HIGH FREQUENCY CAPACITIVE SINGLE CRYTAL SILICON RESONATORS AND COUPLED RESONATOR SYSTEMS

A Dissertation
Presented to
The Academic Faculty

By

Siavash Pourkamali

In Partial Fulfillment
of the Requirements for the Degree
Doctor of Philosophy in the
School of Electrical and Computer Engineering

Georgia Institute of Technology

December 2006

HIGH FREQUENCY CAPACITIVE SINGLE CRYTAL SILICON RESONATORS AND COUPLED RESONATOR SYSTEMS

Approved by:

Prof. Farrokh Ayazi (Advisor)

School of Electrical and Computer Engineering

Georgia Institute of Technology

Prof. Mark Allen

School of Electrical and Computer Engineering

Georgia Institute of Technology

Prof. Oliver Brand

School of Electrical and Computer Engineering

Georgia Institute of Technology

Prof. John Papapolymerou

School of Electrical and Computer Engineering

Georgia Institute of Technology

Prof. Levent Degertekin

School of Mechanical Engineering

Georgia Institute of Technology

Date Approved: August 7th, 2006

In the loving memory of my mother, Shahin Azimi

ACKNOWLEDGEMENTS

I would like to express my deep appreciation to my thesis advisor and mentor, Professor Farrokh Ayazi for his support, encouragement, and advice. I would also like to thank the committee members, Professor Mark Allen, Professor Oliver Brand, Professor Levent Degertekin and Professor John Papapolymerou for their guidance and support.

I would like to acknowledge my colleagues in the Integrated MEMS group Reza Abdolvand, Gavin Ho, and Krishnakumar Sundaresan who have been directly involved in this project. I have always benefited from useful and insightful discussions with them. Without their help, this work would not have been possible. I would also like to acknowledge all of my other colleagues in the Integrated MEMS group for their assistance and friendship. My special thanks go to Babak Vakili, Reza Abdolvand, and Houri Johari for being much more than just colleagues. I have been blessed to have such caring friends around me in the absence of my family during the past five years. I have always enjoyed their company and friendly advice.

I would like to thank the staff of the MiRC cleanroom at the Georgia Institute of Technology for all of their non-stop efforts and collaborations to keep the equipment up and running all the time.

Last but not least, I wish to thank my family, especially my father and my dear departed mother who have been my unlimited source of inspiration and motivation. They have truly devoted their whole life to my comfort, happiness and success.

TABLE OF CONTENTS

LIST OF TABLES

Page

LIST OF FIGURES

Page

LIST OF TERMS

AC:	Alternating Current
AR:	Aspect Ratio
BAR:	Bulk Acoustic wave Resonator
BAW:	Bulk Acoustic Wave
CMOS:	Complementary Metal-Oxide Semiconductor
DC:	Direct Current
DRIE:	Deep Reactive Ion Etching
FBAR:	Film Bulk Acoustic Resonator
HF:	High Frequency
HTO:	High Temperature Oxide
IBAR:	I-shaped Bulk Acoustic Resonator
IC:	Integrated Circuit
ICP:	Inductively Coupled Plasma
LF:	Low Frequency
LO:	Local Oscillator
LPCVD:	Low Pressure Chemical Vapor Deposition
MEM:	Micro-Electro-Mechanical
MEMS:	Micro-Electro-Mechanical Systems
MF:	Medium Frequency
PECVD:	Plasma Enhanced Chemical Vapor Deposition
RIE:	Reactive Ion Etching
Q:	Quality Factor

SAW:	Surface Acoustic Wave
SCS:	Single Crystal Silicon
SEM:	Scanning Electron Microscopy
SiBAR:	Silicon Bulk Acoustic Wave Resonator
SOI:	Silicon On insulator
PPM:	Part Per Million
TCF:	Temperature Coefficient of Frequency
TCXO:	Temperature Compensated Quartz Oscillator
TED:	Thermo Elastic Damping
VHF:	Very High Frequency
UHF:	Ultra High Frequency

SUMMARY

High frequency mechanical resonators such as quartz crystals, surface acoustic wave (SAW) and film bulk acoustic wave resonators (FBAR) and filters are widely used in electronic systems as highly stable frequency references for oscillators and bandpass filters. Recent developments in silicon micromachining technologies has enabled implementation of high frequency silicon capacitive resonators with close to one order of magnitude higher quality factors (Q) compared to the SAW resonators and FBARs. Such devices are gradually entering the market opening up new opportunities for more advanced highly integrated electronic systems. Due to their lithographically-defined resonant frequencies, in-plane capacitive resonators with operating frequencies in a wide range from tens of kHz up to GHz can be implemented on the same substrate simultaneously, providing higher levels of integration. In addition, due to their much high Q values and tunability compared to piezoelectric resonators, capacitive resonators can provide higher performance e.g. lower phase noise for tunable oscillators or ultra-narrow bandwidth for bandpass filters. High-Q micro and nanomechanical resonators also have tremendous potential for precision chemical and biomedical sensing applications.

The objective of the presented research is to implement high-Q silicon capacitive micromechanical resonators operating in the HF, VHF and UHF frequency bands. Several variations of a fully silicon-based bulk micromachining fabrication process referred to as HARPSS have been developed, characterized and optimized to overcome most of the challenges facing application of such devices as manufacturable electronic components. Several micromechanical structures for implementation of high

performance capacitive silicon resonators covering various frequency ranges have been developed. Design criteria and electromechanical modeling of such devices is presented.

Under this work, HF and VHF resonators with quality factors in the tens of thousands and RF-compatible equivalent electrical impedances have been implemented successfully. Resonance frequencies in the GHz range with quality factors of a few thousands and lowest motional impedances reported for capacitive resonators to date have been achieved. Several resonator coupling techniques for implementation of higher order resonant systems with possibility of extension to highly selective bandpass filters have been investigated and practically demonstrated. Finally, a wafer-level vacuum sealing technique applicable to such resonators has been developed and its reliability and hermeticity is characterized.

CHAPTER I

INTRODUCTION

1.1. Overview

A micromechanical resonator is a micromachined mechanical structure that is free to vibrate. Similar to macro-scale mechanical resonant structures a microresonator can have several resonance modes and operate in any of its different modes [1]. A classic example of a mechanical resonator in macro domain is a guitar string that can resonate with frequencies in the audio frequency range (20Hz-20kHz). Due to much smaller sizes achievable for the micromechanical resonators, they can operate at much higher frequencies suitable for a variety of applications in electronic circuits and systems. Depending on their mechanical structure, dimensions and mode of resonance a microresonator can operate in a wide range of frequencies from hundreds of Hz up to a few GHz. When integrated with electromechanical transducers, the mechanical vibrations of a micromechanical resonator can be transformed into electrical signals. Such devices known as micro-electro-mechanical (MEM) resonators can be used as electrical components in electronic circuits.

Mechanical resonance of a single (uncoupled) structure represents the response of its effective structural mass (M_{eff}), stiffness (K_{eff}) and damping (D) in the specific resonance mode of operation to a periodic actuation force. The response of such system to actuation forces in the frequency domain has a second order bandpass transfer function with a specific center frequency (ω_m) and quality factor (Q):

$$\frac{x(s)}{F(s)} = \frac{1}{K_{eff} \cdot \left(\frac{s^2}{{\omega_m}^2} + \frac{s}{\omega_m Q} + 1 \right)} \tag{1.1}$$

where $\omega_m = \left(\frac{K_{eff}}{M_{eff}} \right)^{\frac{1}{2}}$, and $Q = \frac{\sqrt{K_{eff} . M_{eff}}}{D}$.

The bandpass frequency response of the mechanical structure makes such devices suitable for a variety of frequency selection applications such as oscillator frequency references or bandpass filters in electronics [2]. Using proper choice of structural material and micromechanical design, the MEM resonators can exhibit quality factors as high as a few tens of thousands [1-5], which is not possible to achieve using electrical based techniques and components. Such high quality factors enable implementation of ultra-narrow bandwidth, low loss electrical filters and highly stable low phase-noise oscillators.

Macro-scale mechanical resonators have been used in electronics for a few decades [1]. As one of the first materials traditionally used for implementation of highly stable resonators for frequency referencing and timekeeping is piezoelectric quartz crystal which still maintains its superiority over other materials and technologies in terms of frequency accuracy and stability. Pierre and Jacques Currie discovered the piezoelectric effect in quartz crystals for the first time in the early 1880's. They discovered that when pressure is applied to a quartz crystal it generates a voltage, and when a voltage is applied across the crystal it produces mechanical motion or vibration. The first quartz resonator was used in the first quartz clock in 1927 as a replacement for the pendulum clock. Since then, the performance of quartz frequency standards has gradually improved with new

innovations such as use of temperature-compensated quartz crystals (TCXO) [6] and discovery of highly temperature stable crystal cuts such as SC-cut quartz crystal [7]. These discoveries have led to low-cost, extremely stable and precise quartz crystals with high mechanical quality factors (Q). Modern temperature compensated quartz oscillators can be as small as a few millimeters in size and exhibit a temperature drift as low as a few ppm over a 100°C temperature range while consuming only a few milliwatts of power.

As lower cost alternatives for quartz crystals, ceramic resonators and filters [8], have been available in the market for applications where temperature stability is not as critical. Such devices use piezoelectric ceramics as the structural material instead of quartz. In both quartz and ceramic resonators, a bulk of the piezoelectric material with two metal electrodes connected to it is actuated to resonance.

The more recent type of piezoelectric mechanical resonators is the surface acoustic wave (SAW) resonator [9]. A SAW resonator consists of metal electrodes patterned on a piezoelectric substrate. The resonator operates based on the surface acoustic waves generated on the substrate by the electrodes using piezoelectric actuation forces. Depending on the distances between interdigitated electrode patterns the surface acoustic waves at a specific frequency can be optimally actuated and detected by the electrodes therefore providing a bandpass frequency characteristic. SAW resonators and filters with frequencies ranging from a few MHz to a few GHz are commercially available for a variety of wireless applications [10].

Increasing demand for miniaturized electrical appliances especially wireless communication systems with higher performance and lower cost has fueled interest in

development of more integrated, silicon IC compatible, micro/nanoscale solutions for frequency referencing. Such devices have the attractive features of small size, low cost batch fabrication and potential for chip-level or package-level integration with electronics.

The most recent category of high frequency piezoelectric micromechanical resonators available in the market are film bulk acoustic wave resonators (FBAR) and filters [11] that are widely used in RF front-end duplexers as band-select filters. Similar to quartz and ceramic resonators, FBARs consist of a piezoelectric material sandwiched between two metal electrodes. However, in this case the piezoelectric material is in the form of a deposited thin film with thickness in the order of one micron. Such devices are fabricated using micromachining techniques and have the advantage of smaller size compared to their older alternatives. FBAR technology is only suitable for frequencies in the low GHz range. For lower frequencies the film thickness will be too large making it impractical. In addition, since the thickness of the deposited layers determines the resonance frequency of the FBARs, simultaneous fabrication of multiple frequencies on the same chip is not possible.

From temperature and long-term stability point of view, none of the above mentioned resonators beat the superior characteristics of quartz crystal. Efforts are being conducted to develop micro-scale quartz resonators that can be assembled on top of the silicon IC chip and catch-up with the miniaturization trend in that front [12]. Other types of piezoelectric microresonators fabricated on silicon substrates such as longitudinal mode block resonators [13,14] using different piezoelectric materials such as Zinc Oxide [13], or Aluminum Nitride [14] are also under vast investigation. In general for all

piezoelectric microresonator technologies reliability and repeatability of deposited piezoelectric films in a manufacturing environment remains one of the possible drawbacks.

Recent developments in silicon micromachining technologies, have provided the possibility of implementation and characterization of electrostatically operated silicon resonators [3-5,15-29]. Such resonators are fully made of single crystal silicon (SCS) and/or polysilicon and therefore can take advantage of matured, commercially available low cost silicon processing technologies. Capacitive resonators are actuated and sensed by conductive electrodes that are separated from the resonating body by ultra-narrow capacitive gaps. Unlike piezoelectric actuation and detection that requires the drive and sense electrodes to be in physical contact with the resonating body, causing excessive loss and quality factor degradation for the resonators, for capacitive resonators the electrodes are physically isolated from the moving parts. This eliminates loss of motional energy through the electrodes and their junction with the resonator and provides potentially higher quality factors (Q) for such microresonators. In addition, silicon is a low loss material and therefore, close to one order of magnitude higher Q compared to the SAW resonators and FBARs are demonstrated using the SCS and polysilicon microresonators [3-5,15-29]. Such devices are gradually entering the market opening up new opportunities for more advanced electronic systems. Due to their lithographically defined resonant frequencies, in-plane capacitive resonators with operating frequencies in a wide range from tens of kHz up to GHz can be implemented on the same substrate simultaneously [29]. This can be a great progress towards implementation of integrated multi-band wireless communication systems. In addition, due to their much larger Q

values compared to piezoelectric resonators, capacitive resonators may enable direct channel selection right after the antenna resulting in dramatic simplification of the transceiver architectures.

1.2. Capacitive Micromechanical Resonators

The demonstration of capacitive micro-electro-mechanical (MEM) resonators dates back to 1967 with the invention of the resonant gate transistor (RGT) at Westinghouse Research Laboratories [30]. The dimension of this gold resonant beam was 100μm in length, and 5-10μm in thickness, resonating at 5kHz with a quality factor of 500. Several types of capacitive resonators have been used since then for sensory applications [31,32].

During the past few years a great amount of interest has risen up in development of silicon based capacitive micromechanical resonators that can be used as substitutes for traditional piezoelectric resonators in electronics. Higher quality factor provided by silicon, better compatibility with IC integration, good long term and temperature stability and finally availability of a variety of well-established batch-fabrication processes and micromachining techniques has made silicon an attractive structural material for microresonators. Other great advantages of capacitive silicon resonators from the system design point of view are: 1) the resonance frequency of vertical capacitive resonators operating in their horizontal (in plane) resonance modes is determined by their lithography defined dimensions, and therefore resonators with a wide range of different frequencies can be fabricated simultaneously on the same substrate; 2) the resonance frequency of capacitive resonators can be slightly tuned by changing the DC bias voltage applied to them which is required for their operation, such tunability can be used for post fabrication fine tuning or temperature compensation of the resonators; 3) the modulation effect provided by the polarization voltage for capacitive resonators can be used to turn them into narrow band mixers [33] (by replacing the DC bias with the local oscillator (LO) AC signal) or switches (by turning the bias voltage ON and OFF).

A variety of high quality factor (Q) capacitive microresonators with polysilicon [15-23] or single-crystal silicon (SCS) [24-29] as the resonating element have been reported so far. Recently achieved frequencies in the GHz range with quality factors over 10,000 [20,21], demonstrate the potential of capacitive silicon resonators as frequency selective components in the RF front ends as far as the frequency and quality factor is concerned. However, the major bottleneck for capacitive resonators has always been their extremely high equivalent electrical impedances. While impedances well in the 50Ω range can be easily achieved for the piezoelectric resonators, typical capacitive resonators demonstrated in the VHF and UHF range, have impedances in the order of hundreds of kiloOhms [20,26]. The reason behind much higher impedances of capacitive resonators is that electrostatic forces are generally much smaller than the piezoelectric forces generated by similar transducer sizes. As an example, lets compare two transducers, one a piezoelectric actuator with area of $10\times10\mu m^2$ using a 100nm thick layer of Zinc Oxide as the piezoelectric material, and the other one an electrostatic actuator with the same area, a 100nm capacitive air gap and 20V of DC bias. The force generated by a 1V actuation voltage applied to the two actuators will be 6×10^{-3}N for the piezoelectric actuator and 1.8×10^{-6}N for the electrostatic actuator, showing over one thousand times larger force for the piezoelectric actuator. When such actuators are used in a micromechanical resonator, it results in more than one thousand times larger actuation force and more than one thousand times higher sensitivity therefore over a million times lower impedances for the piezoelectric resonator!

The general schematic diagram of an electrostatically operated two-port clamped-clamped beam resonator is shown in Fig. 1.1. Capacitive resonators such as the one

shown in Fig. 1.1 can be operated in a two-port configuration resulting in much lower input-output feed-through capacitance. To drive the microstructure into resonance, (in this case the in-plane flexural mode of the beam) an AC voltage is applied to the drive electrode, and a DC polarization voltage (V_p) is applied to the resonating body. The applied DC bias and AC signal result in a fluctuating electrostatic actuation force applied to the resonator by the drive electrode. On the sense side, there is a DC biased capacitance between the beam and the sense electrode. The fluctuations in the capacitive gap size as a result of resonator motion results in fluctuations of the stored charge in the capacitance. Change in the stored charge in turn is equivalent to an electrical AC current generation in the sense electrode. When the frequency of the applied drive voltage is equal to the mechanical natural frequency of the resonator, vibration amplitude of the microstructure and consequently the output current of the device reach their maximum. The amplitude of vibration at the resonance frequency is Q times (Q=quality factor) larger than the DC displacement amplitudes caused by the same DC drive voltage values.

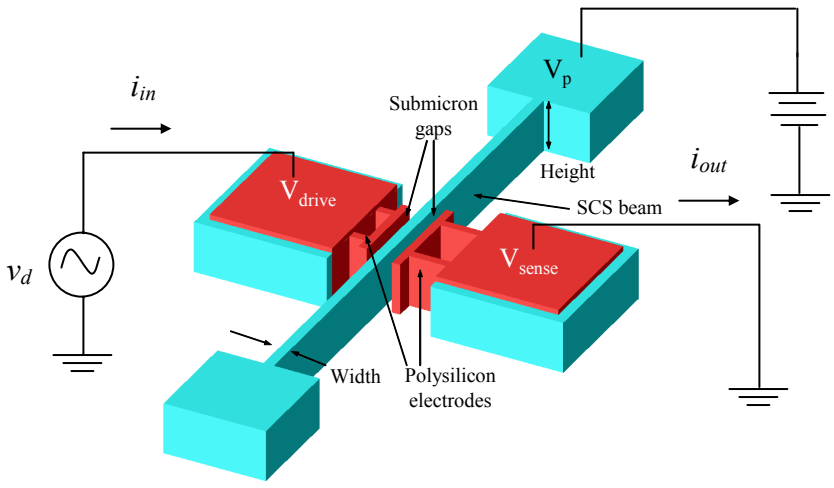

Figure 1.1. Operating configuration of a two-port HARPSS clamped-clamped capacitive beam resonator.

Equation 1.1 gives the electrical equivalent resistance (also known as motional resistance) for a generic two-port vertical (in plane) capacitive microresonator [34]:

$$R_m = \frac{\sqrt{KM}\,g^4}{Q\varepsilon_0{}^2 L_{eff}{}^2 t^2 V_p{}^2} \propto \frac{g^4}{Q.V_p{}^2.L_{eff}.t} \tag{1.1}$$

where g is the sense and drive capacitive gap size, V_p is the applied polarization voltage, L_{eff} is the effective electrode length and t is the thickness (height) of the structure. Gap size (g) has the most significant contribution in the equivalent resistance. However, excessive reduction of the gap size will eventually result in non-linearity and limit the dynamic range of the resonator. In addition, the maximum applicable bias voltage reduces by decreasing the gap size and partially cancels the effect of gap reduction on the electrical impedance. Increasing the thickness and effective length of the resonators on the other hand can help lower the equivalent resistance while increasing the power handling and improve the linearity of the resonator at the same time [26-29]. Finally, having a high quality factor is not only desired to achieve better selectivity and higher performance, but also helps reduce the resonator motional resistance.

In conclusion, for realization of high frequency, high Q capacitive resonators with electrical impedances in the tolerable range for RF applications, which is the main focus of this research, the following are required:

1. A reliable fabrication process that can produce ultra-narrow capacitive gaps (in the order of 100nm and below) in between tall (a few tens of micron) silicon resonator structures and electrodes that are as tall as the resonator itself.

2. Optimized mechanical designs for the resonator structures that have a high frequency resonance mode while maintaining a high quality factor and large transduction area (large resonator height and length).

The following chapters report on the developments and progress achieved in this work towards realization of the above-mentioned requirements as well as the open research topics and future directions in this area.

CHAPTER II

HARPSS BULK MICROMACHINING FOR HIGH FREQUENCY SCS RESONATORS

This chapter presents the accomplished work on development and characterization of a variety of fabrication processes for implementation of high performance single crystal silicon (SCS) capacitive resonators. To meet the specifications described in the previous chapter for high-frequency capacitive silicon resonators with reasonable impedance values, different variations of the HARPSS fabrication process [25-29] have been developed and used in this work.

The HARPSS (High Aspect Ratio combined Poly and Single crystal Silicon) fabrication process, developed by Prof. Farrokh Ayazi at University of Michigan, has been previously used to fabricate thick trench-refilled capacitive polysilicon beam resonators and resonant ring gyroscopes [35,36]. During the course of the presented research, the HARPSS process has been modified and improved gradually in a few steps to become more suitable for implementation of high frequency single crystal silicon resonators with polysilicon electrodes [25-29].

The HARPSS fabrication process has several advantages for fabrication of high frequency capacitive resonators over the alternative available fabrication techniques such as surface micromachining processes [15,16,19-23] or SCREAM [37,38]. HARPSS is a bulk micromachining fabrication process enabling implementation of micromechanical silicon structures as thick as a few tens of microns while having deep submicron capacitive transduction gaps and single crystal silicon as the resonating material. This

allows taking advantage of the bulk of silicon substrate to promote resonator performance and represents a three-dimensional integration approach. HARPSS thick in-plane resonators have the advantage of providing larger capacitive transduction area by extending in the vertical dimension into the silicon substrate while consuming smaller area on the substrate. Single crystal silicon is a very attractive material from the manufacturing point of view because similar to quartz crystal, physical and mechanical properties of single crystalline silicon is defined by the nature of its crystalline structure and is independent of the processing conditions. In addition, the single crystalline nature of the structures can be helpful for reduction of resonator losses and achieving higher quality factors. Larger drive and sense area can alleviate the high equivalent motional resistance issue for the capacitive resonators as well as increase the power handling of the resonators. Moreover, similar to the surface micromachining processes the capacitive gap sizes for the HARPSS resonators are determined in a self-aligned manner by the thickness of a deposited or grown sacrificial oxide layer thus can be reduced down to the sub-100nm range without the need for precision submicron lithography. Having deep submicron capacitive gaps is an inevitable requirement for high frequency capacitive resonators.

The step by step improvement of the HARPSS-based fabrication processes for resonators starting from low frequency beam resonators on regular silicon substrates up to SOI implementation of high frequency low-impedance silicon bulk acoustic wave resonators (BAR) with capacitive gap aspect ratio in excess of 400 is described in the following sections.

2.1. HARPSS Fabrication Process for SCS Resonators on Regular Silicon Substrate

The HARPSS process, as developed at University of Michigan, was capable of producing polysilicon resonant structures with SCS electrodes [35,36]. The first task was to enhance and modify the process to be able to fabricate thick single crystal silicon (SCS) resonator structures with polysilicon electrodes.

The fabrication process flow used to implement low frequency capacitive beam resonators on regular silicon substrates is shown in Fig. 2.1. The process starts by defining the electrically isolated bonding pads for the electrodes. A ~1μm thick thermally grown silicon dioxide covered by a thin layer of LPCVD silicon nitride (3000Å) is used to create the electrode bonding pad isolation from the substrate (Fig. 2.1a). To define the SCS resonating beam, two adjacent high aspect-ratio trenches (3-6μm wide and 20-80μm deep) are etched into the low-resistivity silicon substrate using a deep reactive ion etching (DRIE) system and the Bosch process. The height of the trenches determines the height of the polysilicon electrodes which is approximately equal to the thickness of the resonator itself. A thin conformal LPCVD layer of high-temperature oxide (HTO) is then deposited (at ~850ºC) (Fig. 2.1b) that covers the trench sidewalls as well as the surface of the substrate uniformly. Trenches are subsequently refilled with doped LPCVD polysilicon to form the vertical electrodes. The lateral gap spacing between the SCS beam and polysilicon electrodes is defined by the thickness of the deposited oxide layer, and thus can be scaled down to the tens of nanometer range [4]. Polysilicon is etched back on the surface in plasma to expose the sacrificial oxide layer (Fig. 2.1c). Sacrificial

oxide is patterned to form openings for resonator undercut. Another doped LPCVD layer of polysilicon is then deposited and patterned to form the input and output wirebonding pads. Next, a layer of metal (300Å of Cr and 2000Å of Au) is deposited in an e-beam evaporator and patterned by lift-off (Fig. 2.1d). The resonators are undercut and separated from the silicon substrate using a dry silicon etch in SF_6 plasma, consisting of an anisotropic followed by an isotropic etch to undercut the structures (Fig. 2.1e). During the isotropic etch step the sacrificial oxide layer protects the silicon structure and polysilicon electrodes. Finally, the sacrificial oxide is removed in a HF:H_2O (1:1) solution to release the resonators (Fig. 2.1f). Both clamped-clamped and clamped-free beam resonators with different dimensions covering a wide frequency range can be fabricated using this processing technology.

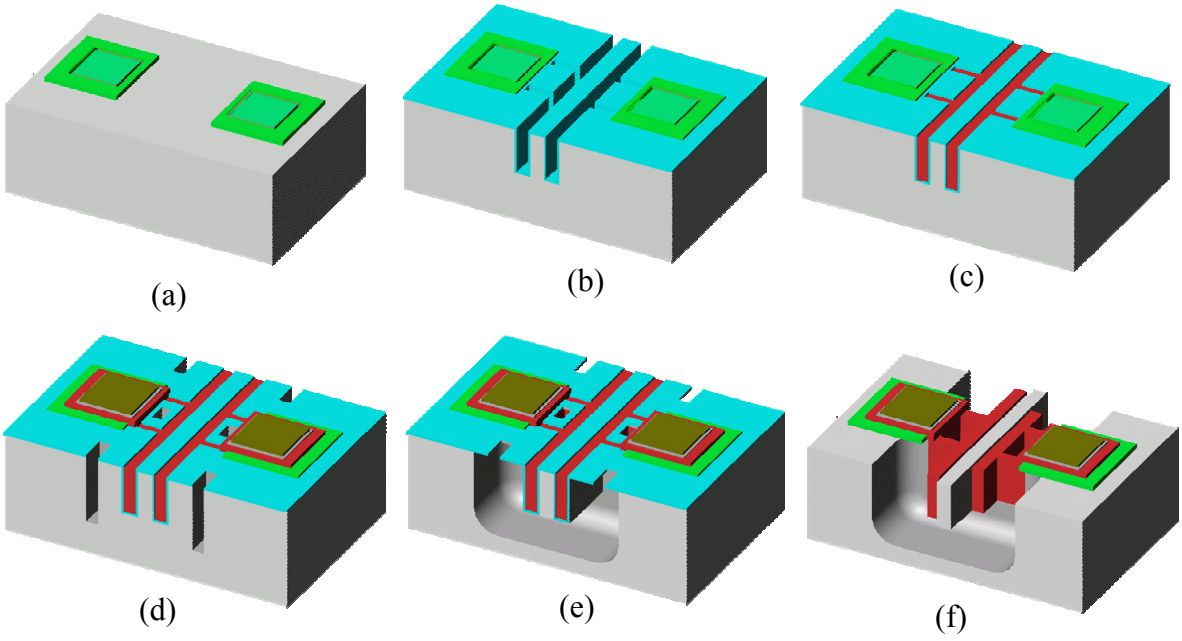

Figure 2.1. HARPSS fabrication process flow for single crystal silicon beam resonators on regular silicon substrates.

Figure 2.2 shows the SEM picture of a fabricated clamped-clamped SCS HARPSS beam resonator. Figure 2.3 is the close-up view of the electrode area, showing the single crystal silicon beam, the polysilicon electrodes and the submicron gaps in between.

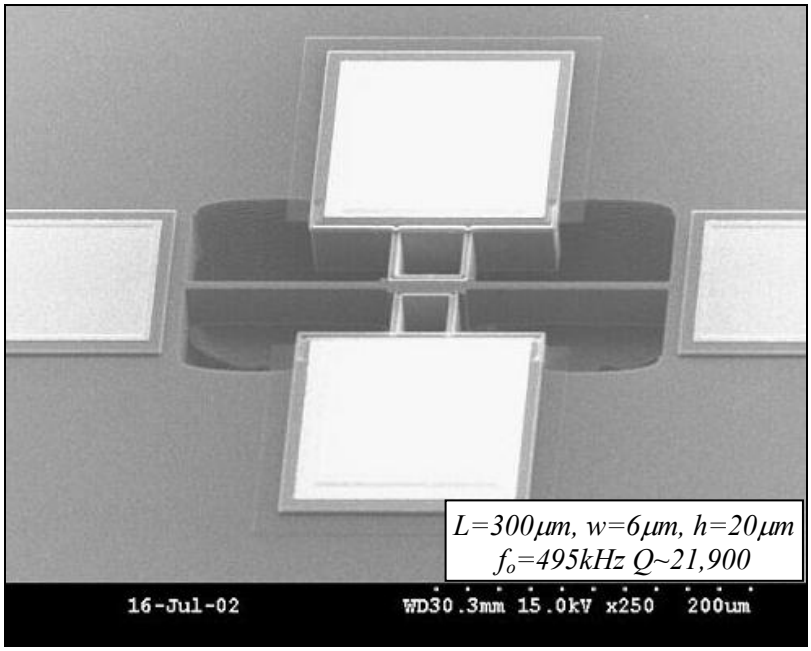

Figure 2.2. SEM view of a clamped-clamped single crystal silicon beam resonators fabricated using the HARPSS process.

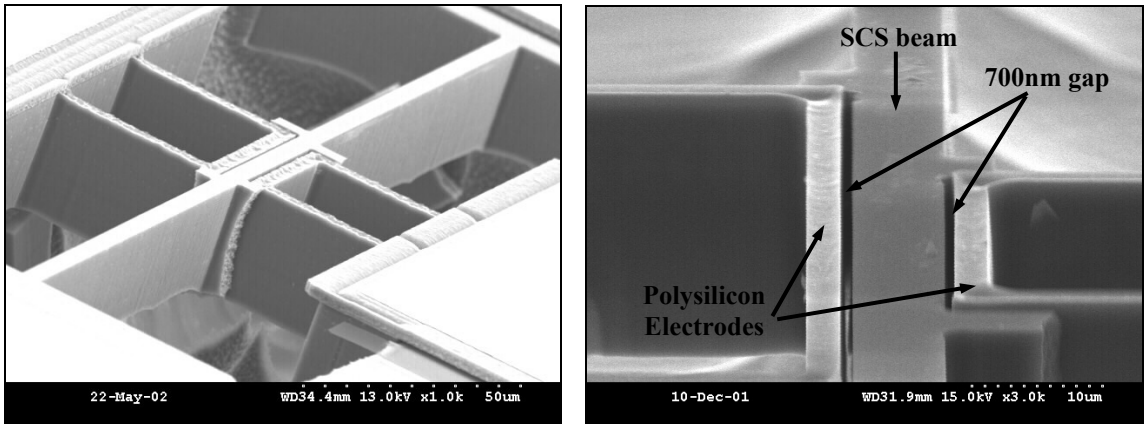

Figure 2.3. Close-up view of the electrode area for a fabricated beam resonator showing the 700 nm gap spacing between the SCS beam and the polysilicon electrodes.

Fabricated SCS beam resonators were tested under vacuum in a custom-made vacuum chamber using an Agilent 4395A network analyzer. Since the resonators have separate electrodes for actuation and sensing, they can be operated in a two-port configuration, where a DC bias voltage (polarization voltage) is applied to the body of the resonator (silicon substrate) and the drive electrodes is connected to the RF output of the network analyzer. Due to very large impedance of the resonators and small power handling, the output signal of the resonators will be too small if directly connected the 50Ω input of the network analyzer. Therefore, very sensitive interface circuits are required. J-FET input wide-band Op-Amps in non-converting configuration were assembled on a printed circuit board (PCB) for this purpose. The MEMS resonator chip was mounted on the board and the input and output signals along with the DC polarization voltage were applied to the resonator through wire-bonds. The PCB was placed inside the vacuum system, which keeps the pressure to below 1mTorr.

Figure 2.4 shows a typical measured frequency response plot taken from the network analyzer, showing a Q of 74,000 at 80 kHz for a 700μm long, 6μm wide and 20μm tall SCS clamped-clamped beam resonator under 1mTorr vacuum. The summary of the Q measurement results for the clamped-clamped beam resonators with various fundamental resonance frequencies ranging from 41.5kHz to 3.2 MHz is given in Table 2.1. The Q decreases as the frequency of the beam increases, mainly due to the thermoelastic damping at lower frequencies [4] and support loss at the higher frequency end.

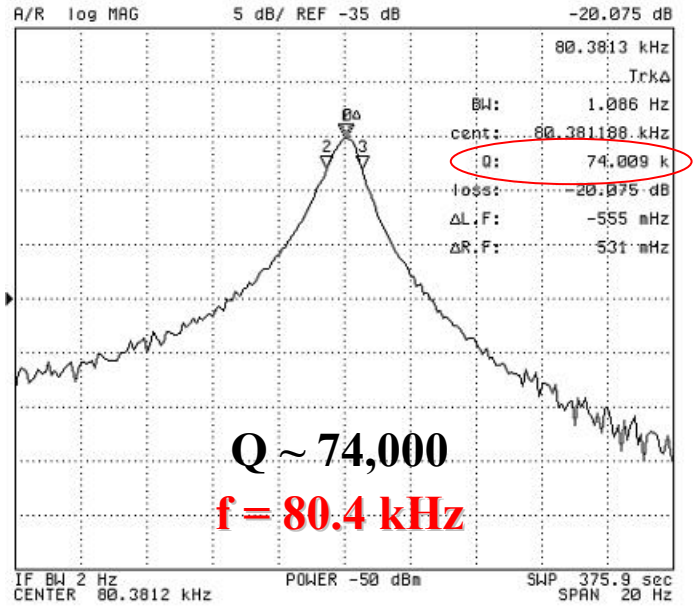

Figure 2.4. Frequency response of a 700μm long, 6μm wide, 20μm thick clamped-clamped beam resonator.

Table 2.1. Measured resonance frequency and quality factor for the fabricated HARPSS SCS clamped-clamped beam resonators with different dimensions.

Dimension		f_0-1st (kHz)	Q
W (μm)	L (μm)		
6	700	80.3	74,000
7.5	700	125.5	39,400
5	500	117.0	67,000
5.5	500	164.5	60,400
6.5	500	198.0	35,000
7.5	500	217.0	27,000
4	300	288.4	43,000
5.5	300	489.3	21,500
6	300	495.5	21,900
6.5	300	528.0	17,000
5	200	911.0	10,000
10	200	3200	4,500

2.2. HARPSS-On-SOI Fabrication Process

For implementation of higher frequency (VHF and UHF) bulk-mode resonators using the HARPSS process, slight modifications were made to the previous version of the process to make it compatible with SOI substrates [25,26]. Due to the uncertainty caused by the isotropic silicon etch to undercut and release the structures on the bottom, perfect dimensional definition of such devices on regular silicon substrates is not possible. Therefore, using SOI substrates for nano-precision fabrication of ultra-stiff bulk-mode SCS resonators with height-to-width-ratio<1 (e.g., disks and blocks) is inevitable. Resonators fabricated on SOI substrates can be undercut by etching the SOI buried oxide layer leaving behind a smooth and well-defined bottom side for the wide bulk-mode resonators. SOI implementation of the resonators can also provide the ability to achieve "electrical isolation" between the body of individual SCS resonators enabling independent tuning of each individual resonator in an array of resonators (e.g. for filter implementation). For the beam resonators discussed in the previous section the body of all the resonators on the same substrate are electrically connected through the substrate. Furthermore, trench isolation on the SOI substrates can help reduce the parasitic capacitances and the related cross-talk between input and output of individual resonators as well as different adjacent resonators. Another important opportunity provided by the SOI approach, is that in the earlier implementation of HARPSS SCS resonators on regular silicon substrates, the sacrificial oxide was used as a protective layer for the silicon structures during the isotropic etch step [4]. Due to finite selectivity of the SF6 silicon plasma etch to silicon dioxide, the minimum achievable gap size was limited by

this mechanism. The use of SOI eliminates the need for a long isotropic silicon etching and hence the capacitive gaps can be reduced to their true physical limits.

The process steps for fabrication of SCS HARPSS resonators on SOI substrates is shown in Fig. 2.5.

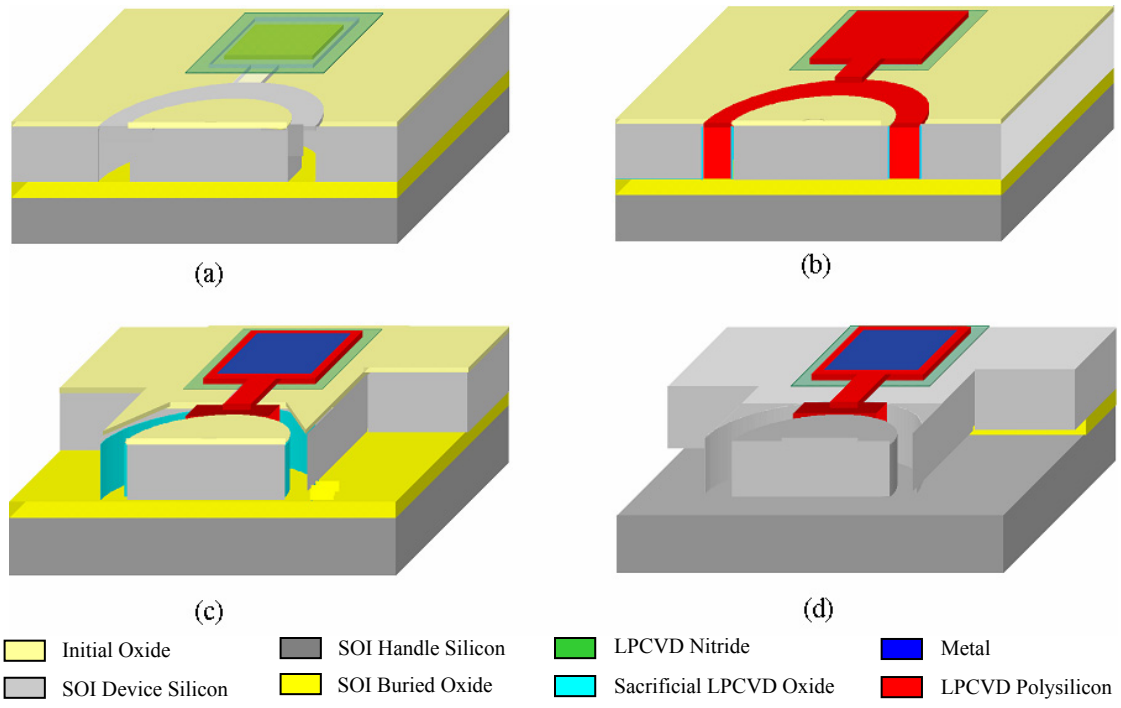

Figure 2.5. Fabrication process flow of single crystal silicon resonators with deep submicron gaps on SOI: a) Grow and pattern initial oxide, deposit and pattern LPCVD nitride, etch trenches (Bosch process); b) Grow and remove thin oxide (surface treatment), deposit and blanket etch sacrificial oxide, deposit and pattern doped LPCVD polysilicon; c) Pattern initial oxide, metallization, etch release openings and pattern polysilicon for electrodes; d) HF release and undercut.

The fabrication process consists of six lithography steps and a number of thin film deposition and etching steps. The process flow for this first version of the HARPSS-On-

SOI process is very similar to the regular silicon substrate process flow described in the previous section. The major modifications are: 1) The initial thermal oxide which is also used for input and output pad isolation, serves as the mask for etching trenches into the SOI device layer which define the resonator boundaries. This oxide layer remains on top of the body of the resonators all the way to the end of the process and protects them against several silicon etching steps during the course of the process. In the previous process flow, the sacrificial oxide was used to protect the resonators, therefore imposing a limit on the minimum tolerable sacrificial oxide thickness, 2) The resonators are undercut by removing the underlying buried oxide layer in a hydro-fluoric acid solution instead of isotropic etching of silicon.

In this approach, vertical trenches are etched all the way through the silicon device layer to the buried oxide layer and therefore the thickness of the SOI device layer determines the thickness of the resonators that can be as thick as a few tens of microns.

A number of side-supported SCS disk resonators with various designs and dimensions were fabricated using the described fabrication sequence on SOI substrates.

Figure 2.6 shows a fabricated 3μm thick, 29.4μm in diameter SCS disk resonator with 120nm capacitive gaps. The disk is supported at one of its resonance nodes by a tiny support beam.

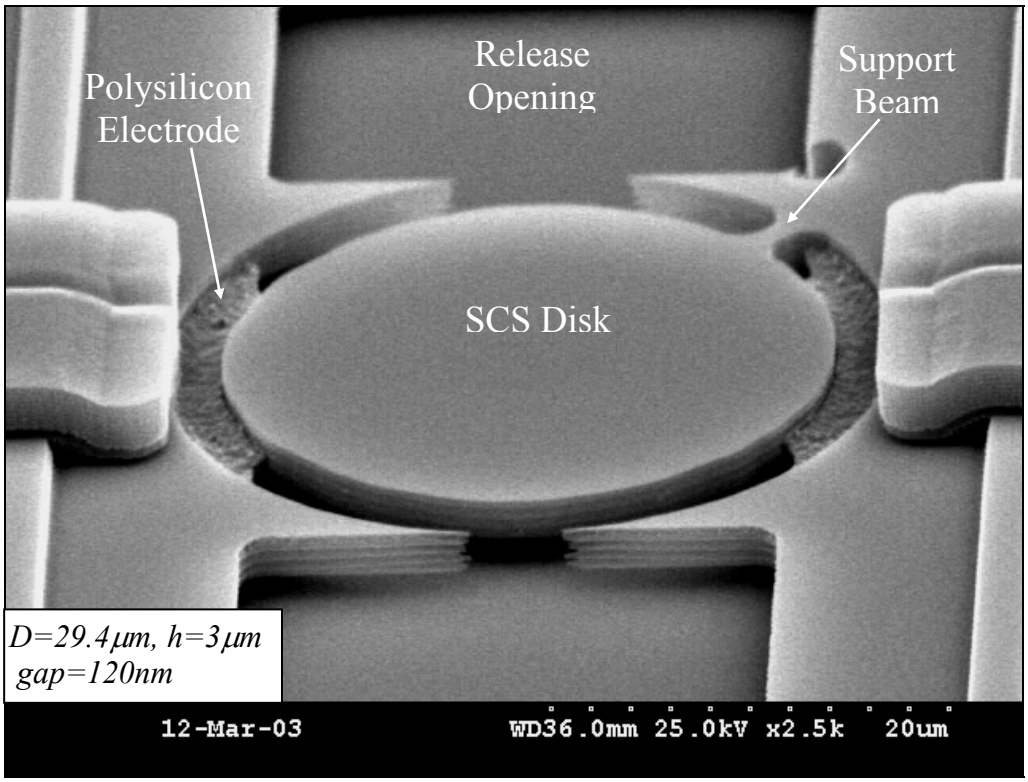

Figure 2.6. SEM of a 29.4μm in diameter, 3μm thick, side-supported SCS disk resonator supported with only one support beam and a capacitive gap spacing of 120nm.

2.2.1. Residual Silicon Nitride Issues for HARPSS-On-SOI Resonators

One of the major issues noticed during the development and characterization of the first version of the HARPSS-On-SOI process described above, was existence of unexpected silicon nitride residues on the resonator edges. The SEM pictures of such devices are shown in Fig. 2.7. To ensure that the residual layer was silicon nitride the devices were dipped in silicon nitride wet etchant (hot phosphoric acid 160-170°C) for long enough time to remove the nitride. The residues were removed after phosphoric acid treatment; however the polysilicon electrodes were attacked by the hot phosphoric acid as shown in Fig. 2.8 and therefore the devices were not operational.

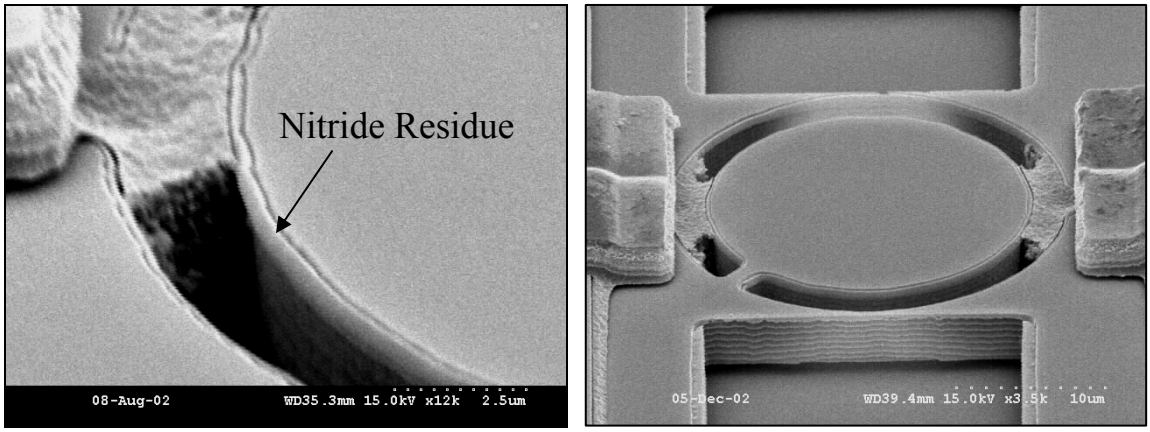

Figure 2.7. SEM picture of the devices fabricated through the HARPSS-On-SOI process showing strips of nitride residues on the device edges trapped inside the gap.

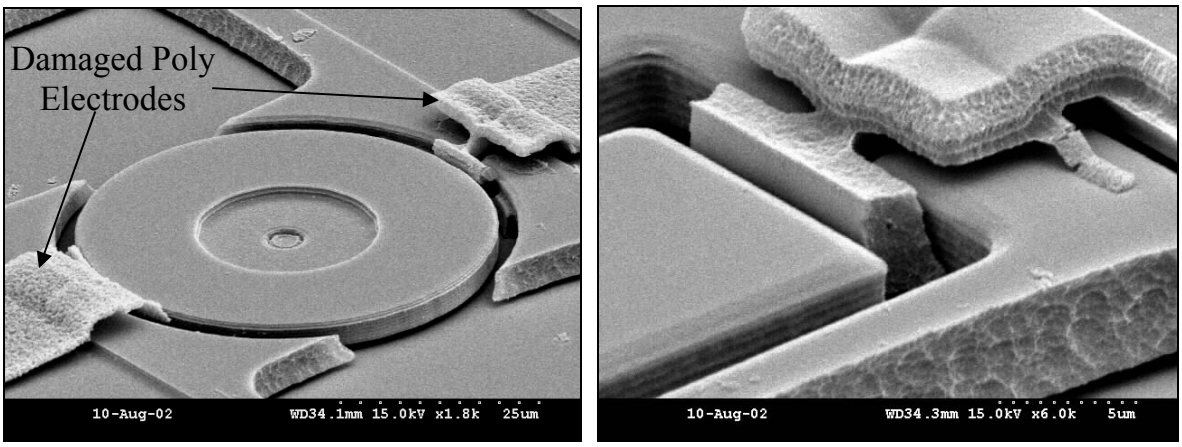

Figure 2.8. SEM view of the resonators after wet nitride etch showing nitride residues removed and polysilicon electrodes attacked by phosphoric acid.

After thorough revision of the fabrication steps, it was concluded that the anisotropic plasma etch used for patterning the nitride deposited on top of the non-flat substrate, with oxide patterns, is responsible for formation of such residues. The schematic diagram of the process of formation of residual nitride strips on resonator edges is depicted in Fig. 2.9.

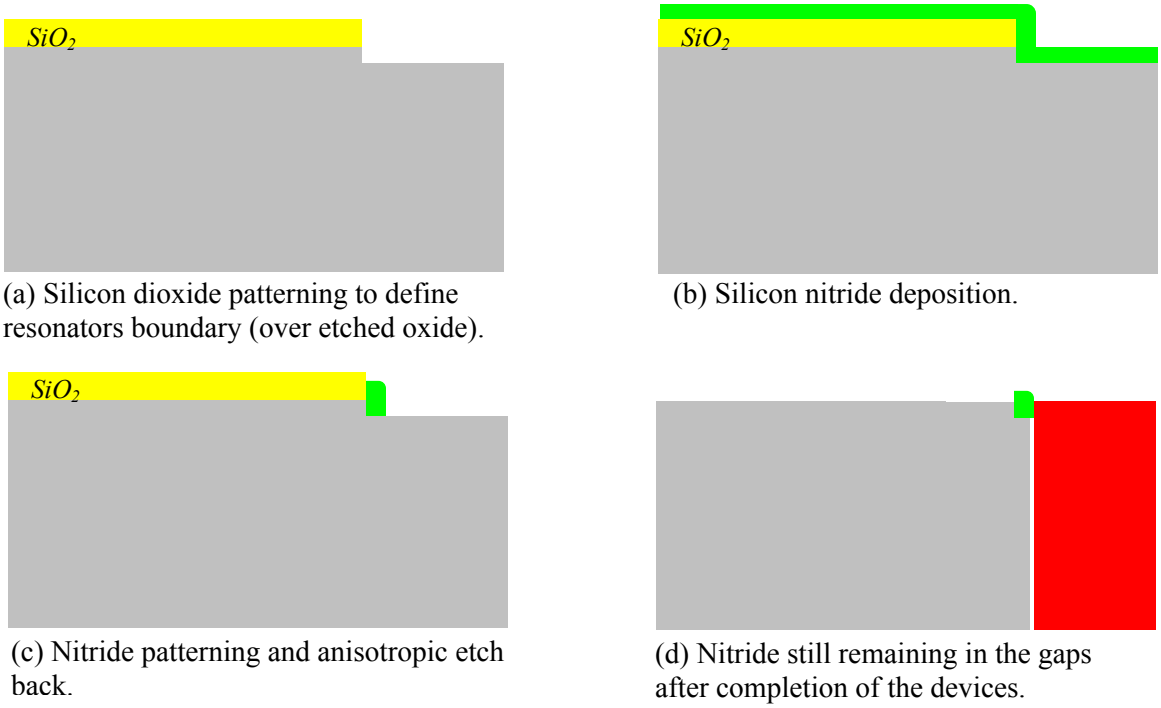

(a) Silicon dioxide patterning to define resonators boundary (over etched oxide).

(b) Silicon nitride deposition.

(c) Nitride patterning and anisotropic etch back.

(d) Nitride still remaining in the gaps after completion of the devices.

Figure 2.9. Process of formation of residual nitride strips on the resonator edges.

To verify the source of the problem, similar initial oxide and nitride deposition and patterning steps were performed on a silicon test wafer. Silicon patterns were etched on the substrate followed by an oxide wet etch in hydrofluoric acid (HF). As shown in Fig. 2.10, nitride strips with the shape of the silicon pattern edges are observed on the devices.

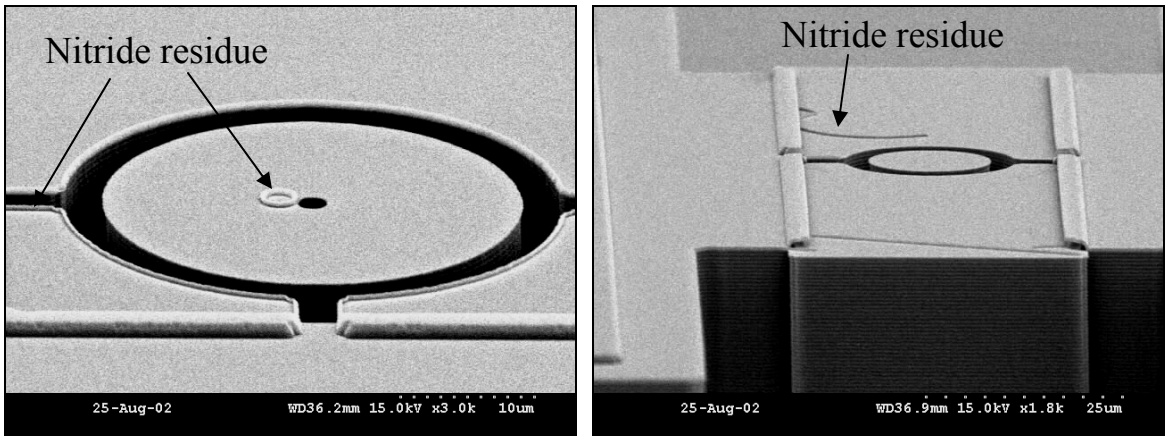

Figure 2.10. Residual nitride strips on test wafer after silicon DRIE and HF oxide etch. The released residues maintain the shape of the silicon boundaries.

Three different solutions were considered to overcome this problem which are as follows: 1. Precise timing of the oxide etch step to stop exactly at the silicon surface, so that the nitride will be supported only by the oxide on top of the resonator and will be detached from the devices when the oxide is removed in HF, 2. Depositing and patterning a thick low stress nitride layer for pad isolation prior to oxide growth and patterning, and 3. Isotropic wet etching of nitride in phosphoric acid instead of plasma etching to pattern the nitride and using an additional LPCVD oxide layer as the etch mask. Eventually both techniques 2 and 3 were deployed for successful demonstration of operational high frequency resonators on SOI substrates (see Chapter IV).

2.3. Simplified 3-Mask HARPSS-On-SOI Fabrication Process

In the described version of HARPSS-On-SOI process in the previous section, the isolation for the input and output pads from the substrate is provided by the oxide and nitride layers and the body of all the resonators are electrically connected to each other through the device layer.

As a more efficient approach, one can pattern the SOI device layer into physically separated islands of silicon providing a strong and reliable isolation between input, output and the body of the resonators. Moreover, by deploying this technique several mask layers used to pattern the isolation nitride and oxide layers will be eliminated. Based on this approach, a simplified and improved version of the HARPSS-On-SOI fabrication process [27,28] was developed that can be done in as few as 3 lithography steps. It is worth mentioning that since adhesion and the electrical connection between the aluminum wire-bonds and bare polysilicon and silicon pads proved to be good enough, the metallization step was also eliminated from the process flow.

The schematic view of the new HARPSS-On-SOI process flow is shown in Fig. 2.11 and is as follows: A 1μm thick initial oxide layer is first thermally grown on the low resistivity SOI substrate. The oxide is patterned and kept only on top of the body of the resonators as well as the polarization voltage wirebonding pads that are physically connected to the resonators (Fig. 2.11a). Similar to the previous version of the process, this oxide layer acts as a mask to protect the structures against the silicon etching plasma during the following silicon and polysilicon etch steps; however it does not need to be kept on top of the electrode pad area for isolation purposes. Vertical trenches are then

etched around the resonators using the Bosch process all the way down to the SOI buried oxide to define the shape of the resonators in the silicon device layer. A thin layer of sacrificial oxide is then deposited (LPCVD) or thermally grown that uniformly covers all the surfaces including the trench sidewalls. The sacrificial oxide is etched back on the surface (Fig. 2.11b) so that the polysilicon pads for the electrodes will be directly connected to silicon and stay firmly anchored during the HF release at the end of the process. Trenches are subsequently refilled with highly p-type doped polysilicon to form the electrodes. The silicon device layer is patterned to provide electrical isolation between different devices as well as the input, output and body of individual resonators. At the same time the polysilicon inside the trenches is patterned and kept only in the desired electrode locations (Fig. 2.11c). Structures are finally released and undercut in hydrofluoric acid by removing the sacrificial oxide layer and the underlying SOI buried oxide (Fig. 2.11d).

Thick SCS disk and block resonators with different dimensions and capacitive gap sizes and operating frequencies in the VHF range (30MHz to 300MHz) were fabricated using the described processing technique. Figure 2.12 shows the close-up view of a fabricated 18μm thick, 29.2 in diameter single side-supported disk resonator and its electrodes. The capacitive gap size for this resonator is 160nm (gap AR ~ 110).

A new design was used for some of the disk resonators at this stage that incorporates four electrodes all around the periphery of the disk for maximum signal transduction. Figure 2.13 is the overall SEM view of the disk resonator of Fig. 2.12, showing all the electrode interconnections. According to the mode shape for the elliptical mode of the disk resonators (see Fig. 4.1 in Chapter IV), the displacement of the resonator towards

each pair of confronting electrodes is in phase. Therefore, by electrically connecting pairs of confronting electrodes the corresponding signals will add up and improve the signal to noise ratio of the device. The polysilicon beam bridging over the resonator (Fig. 2.12) provides electrical connection between two of the electrodes, while the other pair of electrodes are connected by a silicon trace extending around the device (Fig. 2.13).

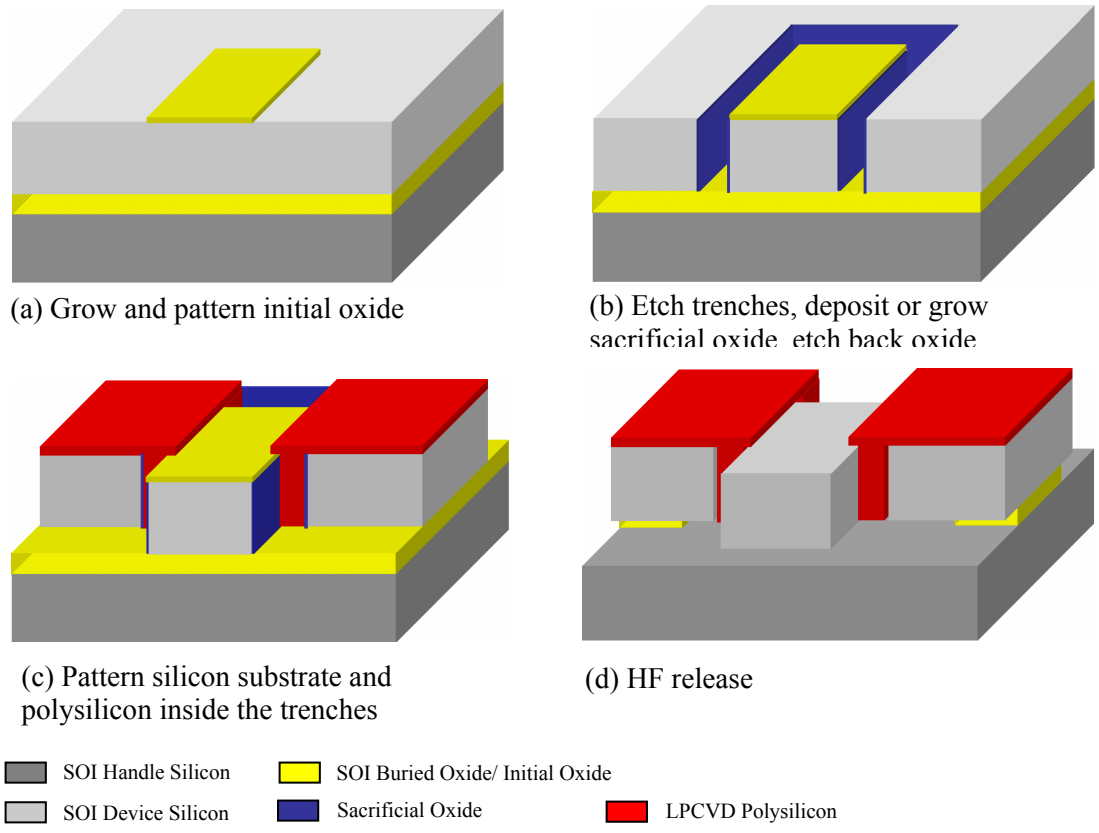

Figure 2.11. Process flow of the three-mask HARPSS on SOI process for fabrication of thick SCS bulk mode resonators.

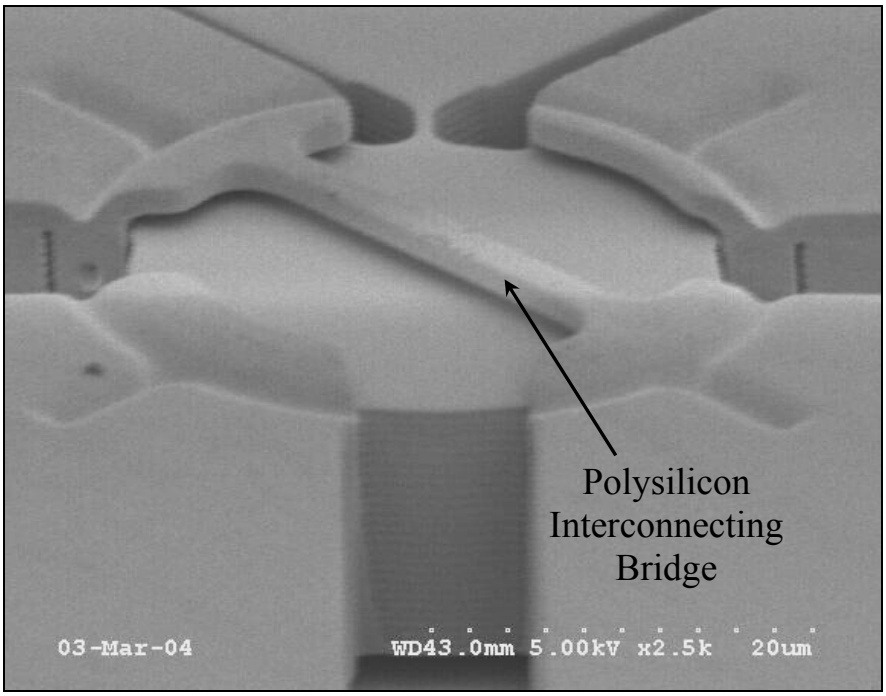

Figure 2.12. SEM of a 29.2μm diameter, 18μm thick, SCS disk resonator fabricated using the 3-mask HARPSS-On-SOI process. The disk is supported by a tiny support beam at one resonance node. Gap Size = 160nm.

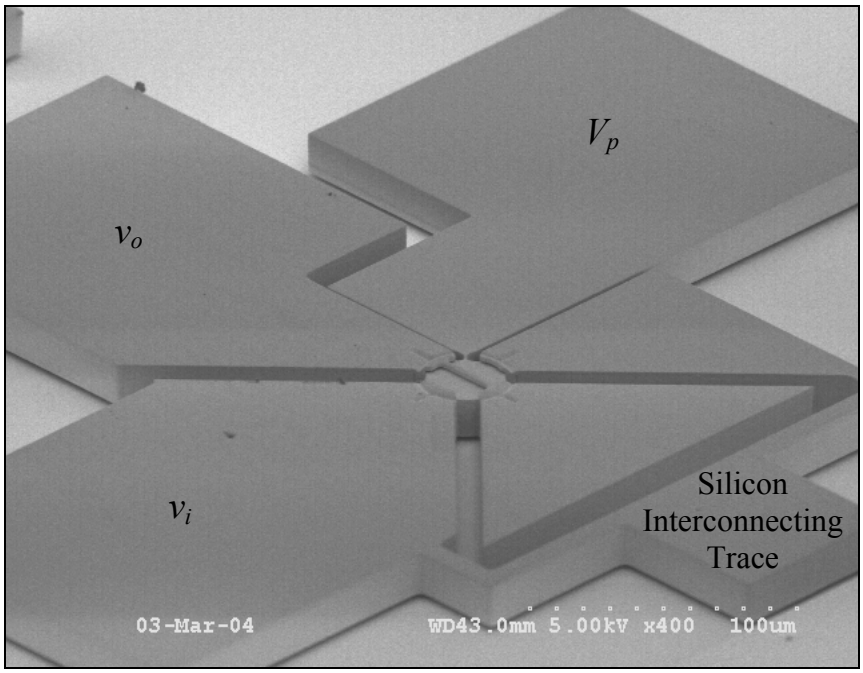

Figure 2.13. Overall SEM view of the SCS disk resonator of Fig. 2.12, showing all the electrode interconnections.

2.3.1. Limitations and fabrication issues associated with the Three-Mask HARPSS-on-SOI Process

The main issue encountered during the characterization and development phase of the 3-mask HARPSS-On-SOI process was associated with patterning the initial oxide. Due to the nature of photolithography and positive photoresist, which was initially used for patterning the oxide, the edge of the patterned oxide features ended up having a slope with oxide thickness going gradually to zero at the device edge. Figure 2.14 shows how this can result in serious problems for the targeted capacitive resonators in this work. Plasma etch back of sacrificial oxide is usually followed by some over-etching to assure complete removal of the oxide on all the surfaces. As shown in Figs. 2.14c and 2.14d, an immediate threat is complete removal of oxide on the resonator edges due to sacrificial oxide over-etch. In this case, the polysilicon deposited to form the electrodes will be electrically shorted to the SCS structure of the resonator (Fig. 2.14d). Figure 2.15 is the close-up view of a polysilicon electrode overlapping the SCS disk resonator showing how the polysilicon touches the resonator at the very edge causing an electrical short.

Furthermore, Figs. 2.14c' and 2.14d' demonstrate schematically that even if the oxide etching is timed precisely to avoid complete removal of the oxide on the resonator edges, there is still a possibility of complete oxide removal during the polysilicon etch back at the end of the process. Due to limited selectivity of the silicon etching plasma to oxide, as the polysilicon inside the deep trench is being etched back, the thin oxide covering the edge of the resonator may be completely etched away resulting in undesired etching of the resonator edges. This imposes a limit on the minimum achievable gap size for the resonators fabricated in this process. It was mentioned in the previous chapter that ultra-thin capacitive gaps and thick resonator structures are the most attractive and useful

features of the HARPSS-based micromachining processes that high frequency resonators can benefit from. Figure 2.16 shows the SEM view of 10μm thick SCS resonators with 75nm capacitive gaps fabricated using this process flow. The edges of the resonator are slightly etched at locations were the polysilicon has been etched back. Apparently this issue limits the maximum achievable gap aspect ratio for the resonators.

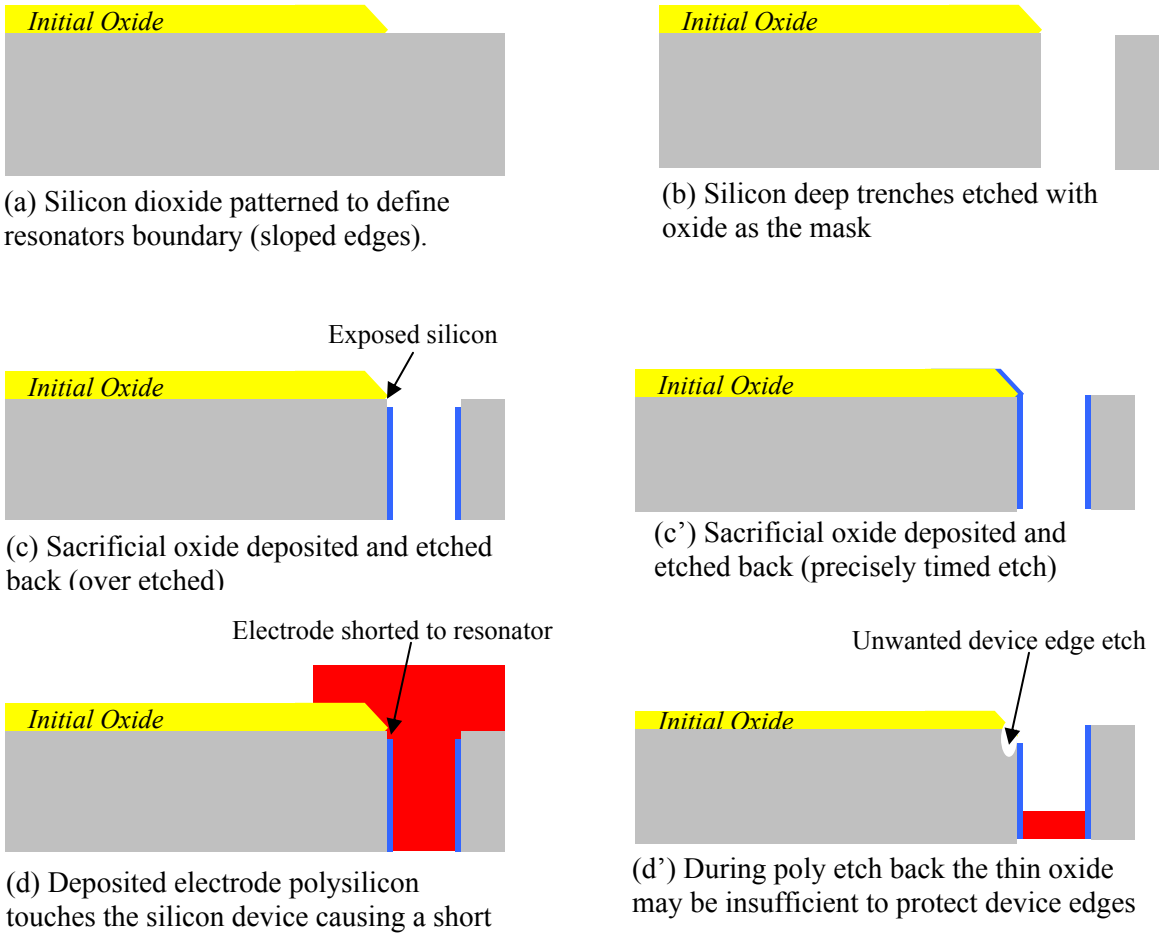

Figure 2.14. Schematic diagram showing the possible electrode shorting or resonator edge unwanted etch problem due to insufficient sacrificial oxide thickness.

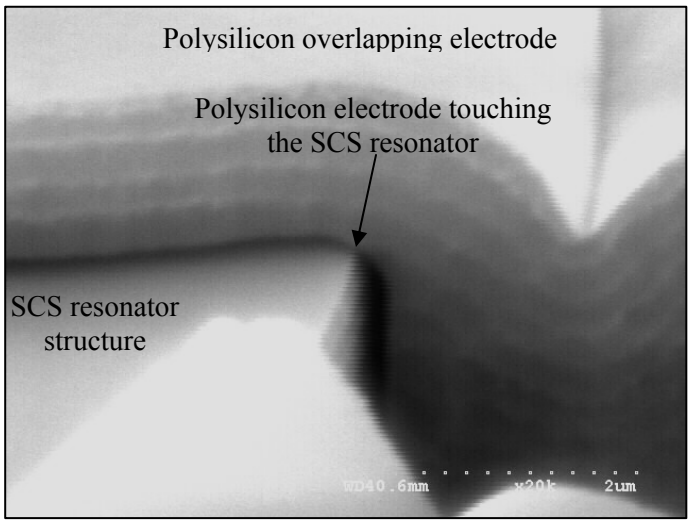

Figure 2.15. SEM view showing close-up of the electrode overlapping point for a fabricated resonators using the 3-mask HARPSS-On-SOI process. The overlapping polysilicon electrode is touching the resonator at the very edge of the structure.

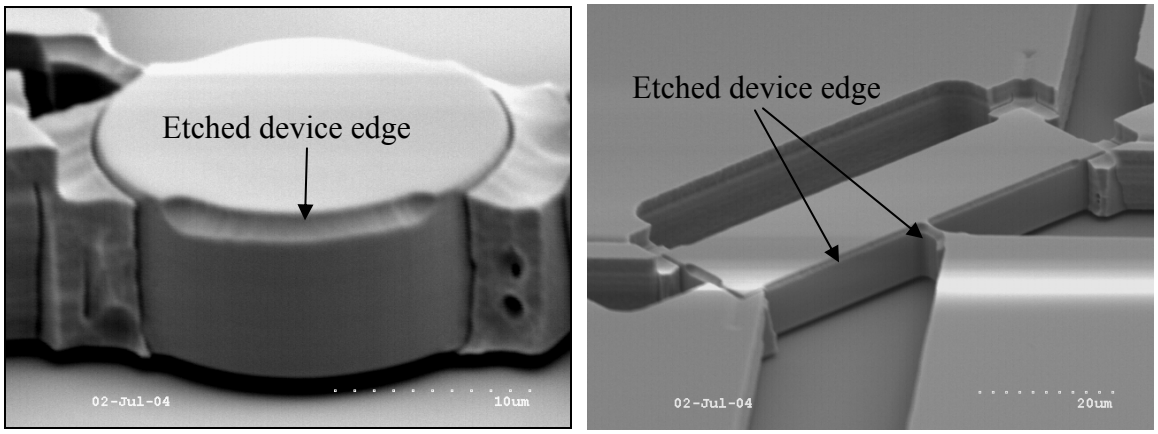

Figure 2.16. SEM view of fabricated resonators using the 3-mask HARPSS-On-SOI process showing unwanted etching of device edge due to insufficient sacrificial oxide thickness.

To alleviate the problems associated with oxide etching the following changes were made to the process: 1. Negative photoresist with precisely timed exposure was used instead of positive photoresist to achieve vertical oxide edges and avoid the oxide slope on the edge as much as possible, and 2. An extra mask layer and lithography step was

added to the process to protect the sacrificial oxide covering resonator edges during sacrificial oxide etch back (Fig. 2.17).

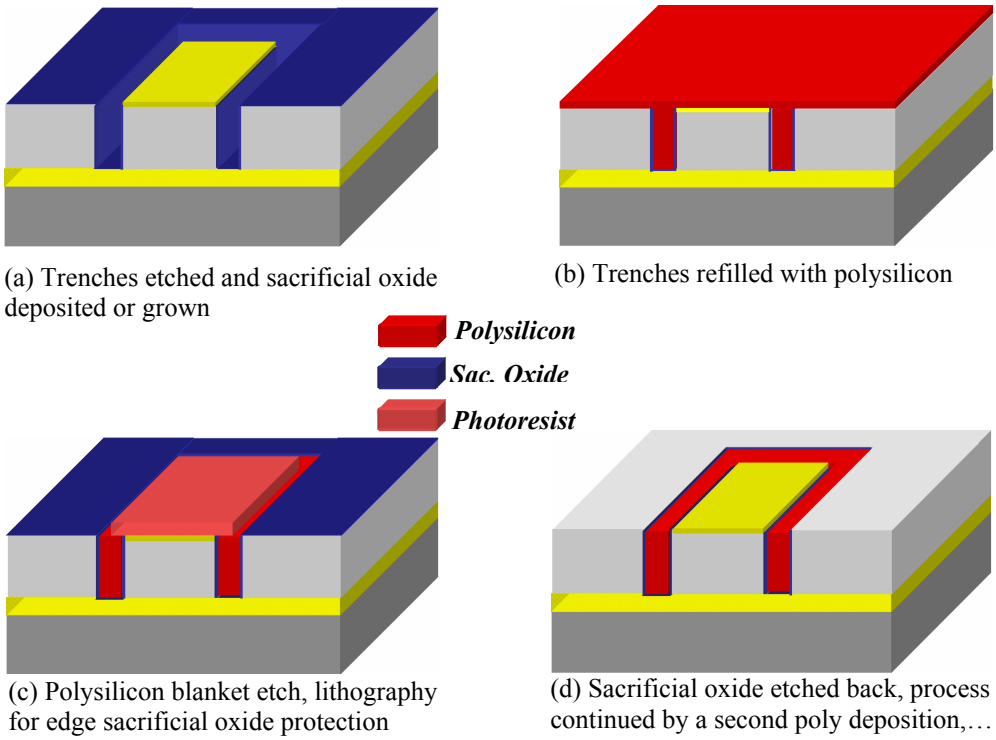

Figure 2.17. Process flow showing the added lithography step for protection of the resonator edges during sacrificial oxide etch back.

The other processing issue associated with all versions of the HARPSS process for fabrication of SCS resonating structures is polysilicon etch back inside the deep trenches. Plasma etching of polysilicon trapped within sacrificial and SOI buried oxide layers inside the deep high aspect ratio trenches is a problematic step that usually leaves behind extremely harmful pieces of residual polysilicon on the resonator sidewalls. Figure 2.18 shows examples of residual polysilicon on the resonator sidewalls after poly etching and HF release. Such residues can cause short or early pull-in of the electrode to the

resonator, or change the resonance frequency of the resonator and reduce its quality factor drastically.

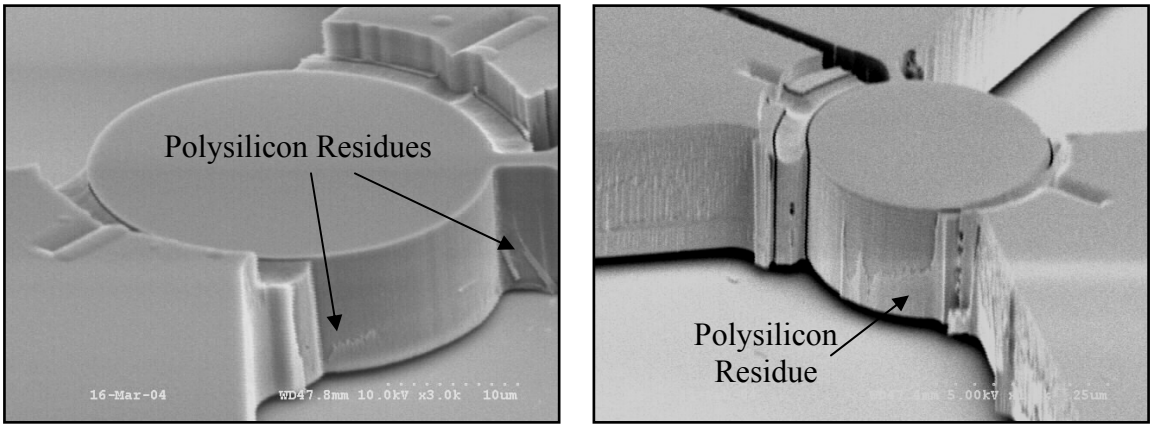

Figure 2.18. SEM view of fabricated HARPSS resonators showing undesired polysilicon residues on the resonator sidewalls.

A short isotropic plasma etching of silicon can reduce the polysilicon residues significantly. A variety of isotropic silicon plasma etching recipes with different reactive gas concentrations were examined for this purpose. Figure 2.19 shows the resulting resonators after pre-HF-release isotropic etching of silicon in a combined gas recipe in the STS ICP system. The recipe includes both SF_6 and C_4F_8 gases in plasma with different concentrations of C_4F_8. No significant polysilicon residual pieces can be observed on the resonator sidewalls, however, silicon plasma isotropic etching is not easily controllable for such small device dimensions, i.e. the exposed silicon around device pads is etched much faster than the residues inside the trenches which can be problematic in some cases. In addition, such uncontrollable isotropic plasma etch induces severe uncertainty in the electrode dimensions.

A more reliable solution to the residual poly problem would be isotropic etching of poly in a non-plasma reactor, e.g. a Xenon Di-Fluoride (XeF_2) silicon etch system, to avoid charging effects and provide more uniformity and controllability over the etch recipe. Due to unavailability of such system in the Georgia Tech microelectronics research center (MiRC) cleanroom, long thermal wet oxidation prior to HF release was used for conformal removal of the polysilicon residues and generation of fully operational devices.

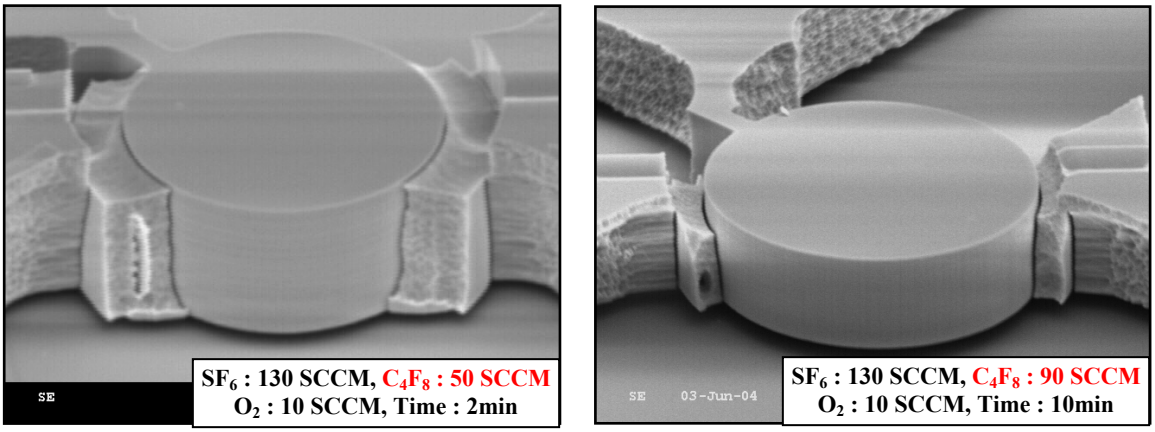

(a) (b)

Figure 2.19. SEM view of resonators fabricated using the 3-mask HARPSS-On-SOI with a short isotropic silicon etch added to remove polysilicon residues.

The above mentioned existing problems in the 3-mask HARPSS-On-SOI process, i.e. polysilicon residues as well as limits on the maximum achievable gap aspect ratio, motivated development of a more advanced HARPSS-based fabrication process which will be explained in the following section.

2.4. Improved HARPSS-On-SOI Process

It was shown in Chapter I that the major challenge for implementation of RF compatible high frequency capacitive resonators is the small electromechanical coupling coefficient of the electrostatic transducers and consequently, high impedance and low power handling of such devices. One of the aspects of the solution to this problem is design optimization of the resonator mechanical structures to maximize electrode transduction area while maintaining high operating frequencies and quality factors. On the device fabrication front, it is well known that reduction of the transduction capacitive gap sizes can significantly reduce the impedance of the resonators. In addition, increasing the resonator thickness which is a unique feature of the HARPSS fabrication process can help further increase the electrode area and consequently reduce the impedance and increase the power handling of the resonators.

Several versions of the HARPSS-based fabrication processes for implementation of SCS resonators with polysilicon electrodes were described in the previous sections. Despite all the progress and demonstrated operational high-Q resonators, there are still processing issues and limitations for achieving the potentially infinite gap aspect ratio promised by the HARPSS process. As an ultimate solution to the existing problems, an advanced version of the HARPSS-On-SOI process was developed. The main goal in development of this version of the process was to completely eliminate the polysilicon etching step to avoid the problems associated with it (undesired polysilicon residues). The process flow is designed so that after formation of the sacrificial oxide and refilling the trenches with polysilicon, the resonator-electrode gaps remain completely untouched

all the way to the end of the process when the sacrificial oxide is etched in HF. This way the resonator gap defined by the sacrificial oxide will be extremely clean and intact until during the process and there will be no limit on the resonator capacitive gap aspect ratio. To achieve this goal a few lithography steps as well as an initial thin nitride layer were added to the process flow. Nitride is used as a mask for oxidation of silicon. The added lithography steps and nitride layer, provide much higher flexibility and new capabilities for the process to implement a variety of new devices and structures that were not possible using the previous versions. Operating resonators with gap aspect ratio as high as 460 have been demonstrated using this fabrication technique which is much higher than the highest demonstrated gap aspect ratios for the previous versions of the process (~160) or the maximum achievable aspect ratios using the state of the art DRIE systems (~60 as reported in [39]).

The process flow for the improved HARPSS-On-SOI process is shown in Fig. 2.20. The process starts with deposition of a thin LPCVD nitride layer (~1000-2000Å) which will be used as an oxidation mask for silicon during the upcoming oxidation steps in the process. A comparatively thick layer of LPCVD silicon dioxide is then deposited on top of the nitride layer. This oxide layer plays a similar role as the initial oxide on the previous version of the process and is used as an etch mask for the silicon device layer. Depending on the thickness of the SOI device layer, the thickness of this oxide layer can be between 0.5 to 2.5μm. The LPCVD oxide layer is then patterned by plasma etching. In this step trenches defining the boundary of the resonators are etched all around them in the oxide layer (Fig. 2.20a). The oxide etch has to be timed precisely to avoid etching of the underlying nitride layer. The second lithography step covers all the area with

photoresist except the locations where the polysilicon electrodes are to be formed, i.e. the oxide trenches are only exposed at electrode locations.

This is one of the major differences between this process flow and the previous version. In the previous approach silicon trenches were etched all around the resonator and in the end polysilicon was removed at undesired locations to leave the electrodes behind. In this approach poly refilled trenches are only formed at required (electrode) locations and therefore no poly etch-back inside the trench will be required at the end of the process. The next few steps are trench etching (all the way to the SOI buried oxide layer) sacrificial oxide growth (Fig. 2.20b) and polysilicon trench refill which is part of all HARPSS-based fabrication processes. Polysilicon is then etched back to expose the initial oxide and nitride layers for patterning (Fig. 2.20c). Next, the remaining initial oxide is patterned and kept only on top of the resonators and their polarization voltage bond pads (similar to the previous process). In other words oxide is kept on locations were the device layer is to remain and be part of the completed device (Fig. 2.20d). Wet etching in BOE is used in this step for oxide etch back because typical oxide plasma etching recipes have a very low selectivity to nitride and result in complete removal of the nitride layer at locations were oxide is already removed. To have a more reliable mask for thick oxide patterning in BOE, a thin layer of polysilicon (~1μm) is kept on the surface during poly etch-back to be patterned in the following lithography (oxide patterning lithography) and protect its underlying oxide layer flawlessly. The undercut and possible feature distortions caused by this wet etch step will not jeopardize resonator performance since it defines only non-critical features e.g. anchors and bondpads.

The fourth lithography step is for patterning the nitride layer. The nitride needs to be removed at locations were electrical connection between the silicon device layer and pad polysilicon is required (Fig. 2.20d). In addition if the nitride is removed on locations were will not be covered by pad polysilicon later on, an oxide layer will be grown during the final oxidation step. Therefore, such parts of the silicon substrate will survive during the final patterning of the device layer.

The next step is deposition and patterning of the pad polysilicon (Fig. 2.20e). The process is followed by a thick wet oxide growth (0.5-1.5μm depending on the device layer thickness). During this oxidation step any polysilicon or silicon surface which is not covered by nitride will be oxidized (Fig. 2.20f) and therefore protected during the final silicon etching for patterning the substrate and releasing the resonators. The substrate is now ready for final device layer patterning without the need for additional lithography. The resonator bodies are protected by the thick initial oxide and the polysilicon pads and electrodes are protected by the thermally grown oxide during the last oxidation step (Fig. 2.20g). The thin nitride layer covering the area in between the resonators acts as a mask during the oxidation step and protects its underlying silicon device layer from oxidation. The thin nitride will be removed during the final silicon etch and therefore the underlying silicon will be etched away leaving behind isolated islands of silicon for different devices. Finally the structures are released and undercut in a hydrofluoric acid (HF) solution (Fig. 2.20h). The remaining nitride layer on top of the resonator structures will be removed during this long HF release as well.

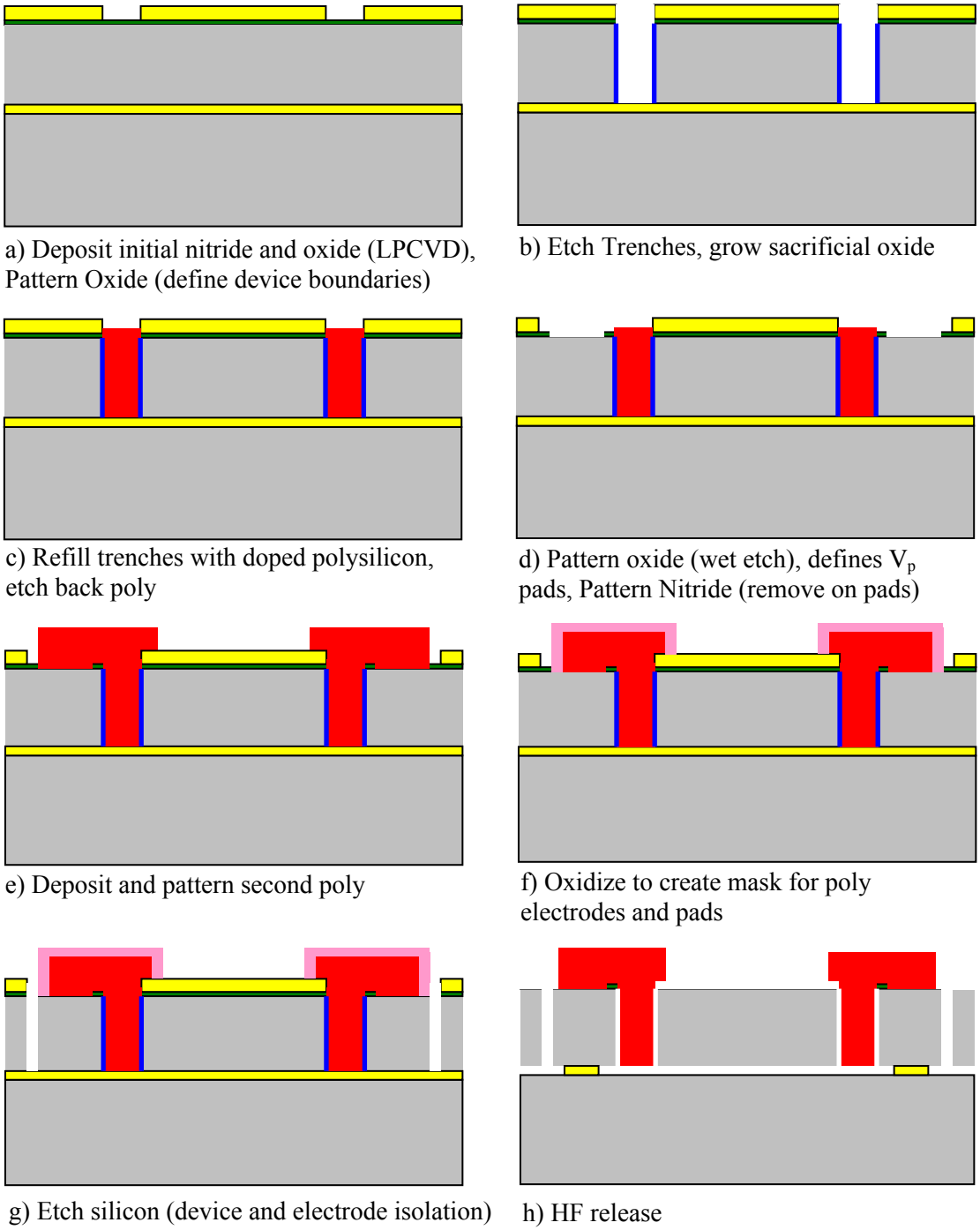

Figure 2.20. Process flow for the advanced HARPSS-On-SOI process. Using silicon nitride for self-aligned definition of the resonator and electrode boundaries.

Figure 2.21 shows the SEM view of fabricated SiBARs using the described fabrication process. As seen in the SEM pictures, the electrodes for these resonators expand all around the resonator and surround the support beams as well. Such expanded electrodes do not deteriorate device performance; however facilitate fabrication of the resonators with perfectly symmetric shapes and possibly higher fabrication yield.

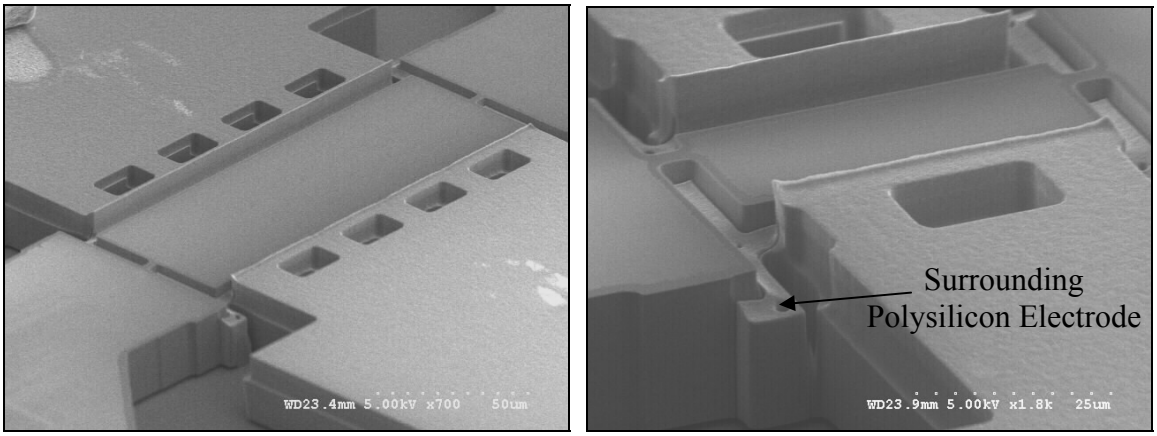

Figure 2.21. SEM view of 20μm thick SiBARs with 125nm capacitive gaps fabricated using the improved HARPSS-On-SOI fabrication process.

Moreover, as mentioned previously, the main advantage of this processing approach is that the whole electrode area will be covered by sacrificial oxide and polysilicon right after getting etched and stays untouched all the way to the end of the process when it is released. This enables implementation of ultra-high-aspect-ratio capacitive transduction gaps between the SCS resonators and their polysilicon electrodes. Figure 2.22 is the SEM photograph of a 30μm thick SiBAR with 65nm capacitive gaps, exhibiting a gap aspect ratio of ~460.

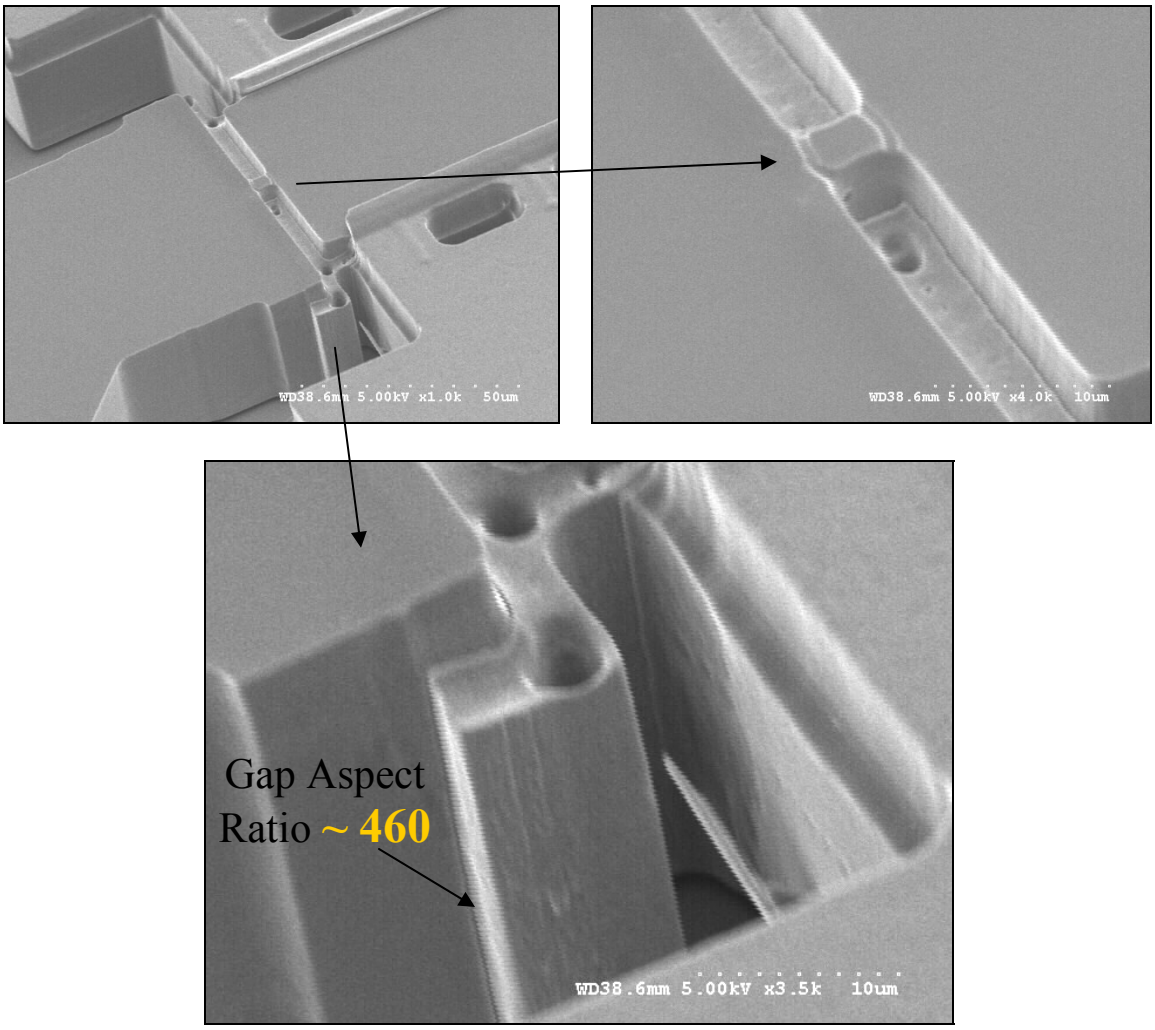

Figure 2.22. SEM view of a 30µm thick resonator with 65nm gaps representing a gap aspect ratio of ~460.

Fabrication of resonators for which the electrodes do not extend all around the resonator, e.g. I-BARs [40,41], using the improved process is more risky. Although such devices still benefit from untouched ultra-high aspect ratio transduction gaps, at the transition point from the area covered by the electrodes to the uncovered area, asymmetry and slight distortion of the resonator shape can occur. Figure 2.23 shows the close-up view of the electrode edge for a 20µm thick I-BAR with 125nm capacitive gaps showing how the resonator sidewall is slightly distorted at the transition point although being

completely clean and operational. Figure 2.24 shows an overall view of some of the fabricated I-BAR resonators.

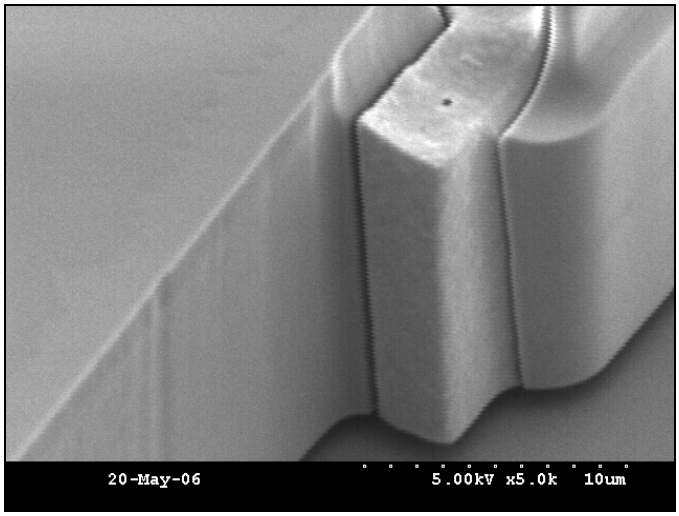

Figure 2.23. Close-up of electrode edge for a 20µm thick SiBARs with 125nm capacitive gaps showing slight distortion of the resonator sidewall at the transition point.

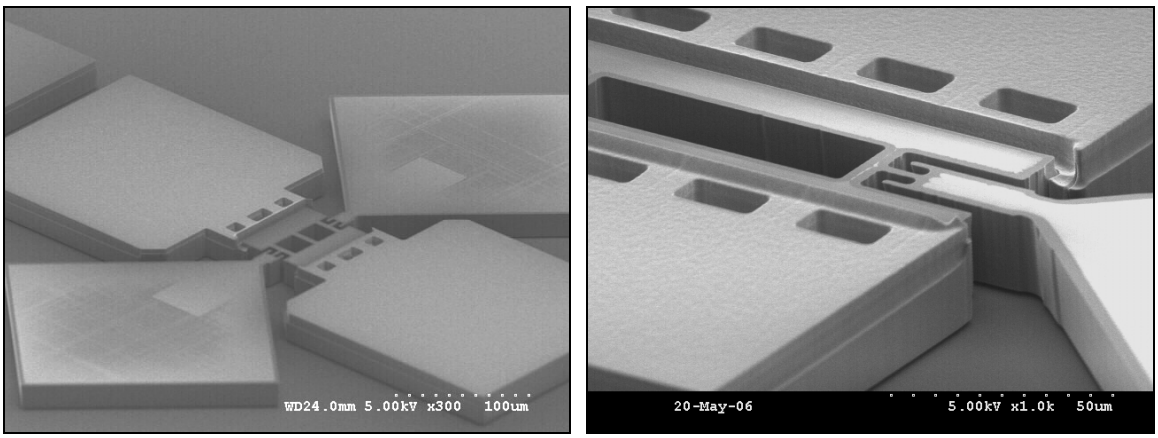

Figure 2.24. SEM view of 20µm thick I-BARs with 125nm capacitive gaps fabricated using the improved HARPSS-On-SOI fabrication process.

The improved HARPSS-On-SOI process has only one additional lithography step compared to its previous version (a total of 5 mask layers), however the added nitride

layer and process steps add tremendous new possibilities and capabilities to the process that were not available before. As an example nitride can be used as an electrical isolation layer which stays intact during HF release. It enables having isolated silicon and polysilicon layers on top of each other without the polysilicon being suspended. This capability can be deployed for implementation of large biasing resistors (e.g. for capacitively coupled resonator filters), using ultra-long tracks of isolated polysilicon on top of a silicon island as shown in Fig. 2.25.

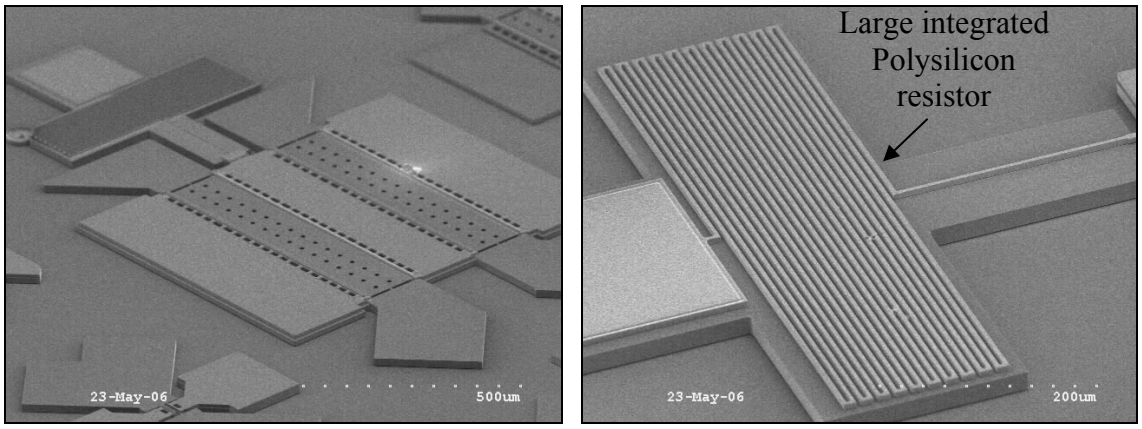

Figure 2.25. Capacitively coupled SiBARs with coupling capacitor bias provided by a large integrated polysilicon resistor. The polysilicon tracks are electrically isolated from the underlying silicon island.

Figure 2.26 shows another example of new possibilities enabled by the improved process. The polarization voltages for the electrostatically coupled resonators of Fig. 2.26 are isolated from their coupling voltages. The polysilicon pad on top of the polarization voltage silicon pads are electrically isolated from them by the initial nitride and oxide layers. The polysilicon carrying the coupling voltage bridges over the body of the resonator without touching it and connects to the polysilicon electrode which is physically connected but electrically isolated from the resonator body.

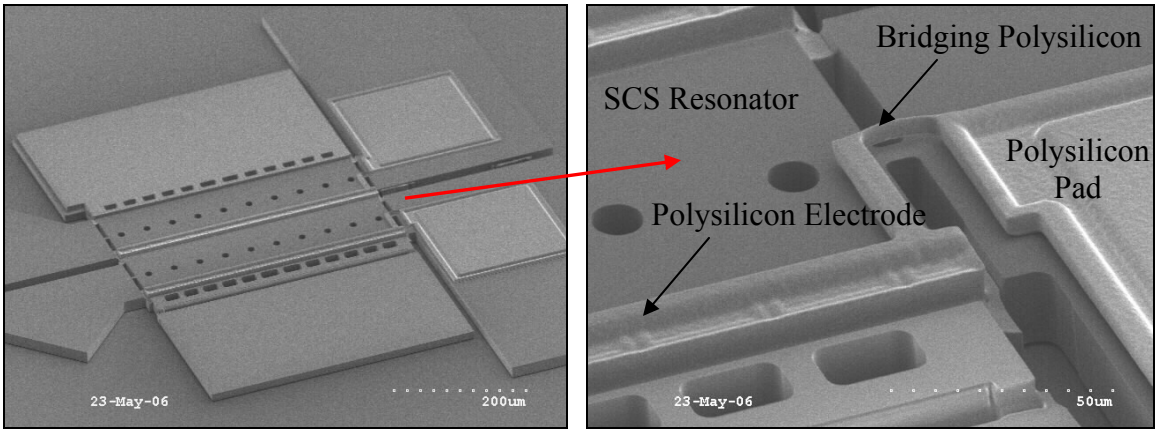

Figure 2.26. SEM view of electrostatically coupled SiBARs with independent coupling voltages. The polysilicon pad and electrode are physically connected to the SCS body but electrically isolated from them by the nitride layer.

In addition to the abovementioned possibilities the thin nitride layer can also be used for simultaneous monolithic fabrication of dielectric-based sensors and actuators, e.g. dielectric gap resonators and filters [42,43].

CHAPTER III

Fully SCS Resonators with Deep Submicron Dry-Etched Capacitive Gaps

This chapter reports on an alternative approach investigated under this project for implementation of high frequency SCS resonators with nanoscale capacitive transduction gaps. In this approach, the capacitive gaps are formed by dry etching of silicon in a deep RIE (DRIE) silicon etcher. The mask features defining the submicron width of the transducer gaps are created in a self-aligned manner using regular optical lithography. This is enabled using a novel processing technique [24] that uses the thickness of a deposited sacrificial polysilicon layer to define the gaps. The submicron gaps are then dry-etched using the Bosch process in an ICP system.

In the HARPSS-based fabrication processes, the submicron transducer gaps are defined and formed between silicon structures by a deposited or grown thin silicon-dioxide sacrificial layer. A similar approach but with the opposite choice of materials is used in this chapter to form silicon dioxide structures with a thin polysilicon sacrificial layer in between them. The oxide structure is then used as a mask for silicon DRIE transferring the submicron features into the silicon substrate. The resulting structure on the silicon substrate will be fully made of single crystal silicon (as opposed to the HARPSS approach which is a mixture of poly and SCS). This can alleviate some of the fabrication and testing problems associated with using polysilicon, e.g., polysilicon etch-back issues, polysilicon quality degradation caused by exposure to HF, and release of polysilicon debris in small capacitive gaps. In addition, dry-etched capacitive

transduction gaps usually demonstrate superior electrical isolation and tolerate higher polarization voltages.

3.1. Deep-submicron Trench Definition and Etching

In order to implement fully-SCS resonators with ~100nm capacitive gaps, the possibility of etching deep-submicron trenches in silicon using the Bosch process was first to be investigated. Figure 3.1 shows the processing steps used to create a silicon dioxide mask with deep-submicron polysilicon features enclosed in it. A layer of oxide (~1μm thick) is first thermally grown or deposited on the silicon substrate. This oxide layer is then patterned to form shallow and narrow (~1μm wide) trenches in the oxide. A thin layer of sacrificial LPCVD polysilicon (~100nm) is then deposited that covers oxide trench sidewalls uniformly. The shallow oxide trenches are subsequently refilled with LPCVD silicon dioxide. The deposited oxide is etched back on the surface in an anisotropic plasma etcher so that the polysilicon on the sidewalls of the initial oxide trenches is exposed.

The sacrificial polysilicon and the underlying silicon substrate are then etched using the Bosch process in an inductively coupled plasma (ICP) system. This step takes advantage of the high selectivity of the Bosch process to silicon dioxide (>100:1) and enables etching a few microns deep into the silicon substrate with the comparatively thin oxide mask on the substrate. After trenches are formed, the remaining oxide mask on top of the substrate can be removed with a quick dip in HF, leaving behind the nano-trenches in silicon.

Figure 3.2 shows the cross section view of ~130nm wide, 2.6μm deep trenches with an aspect ratio (*AR*) of ~20:1 etched in the silicon substrate using the described technique. The trenches start to pinch-off on the bottom for *AR* >20:1.

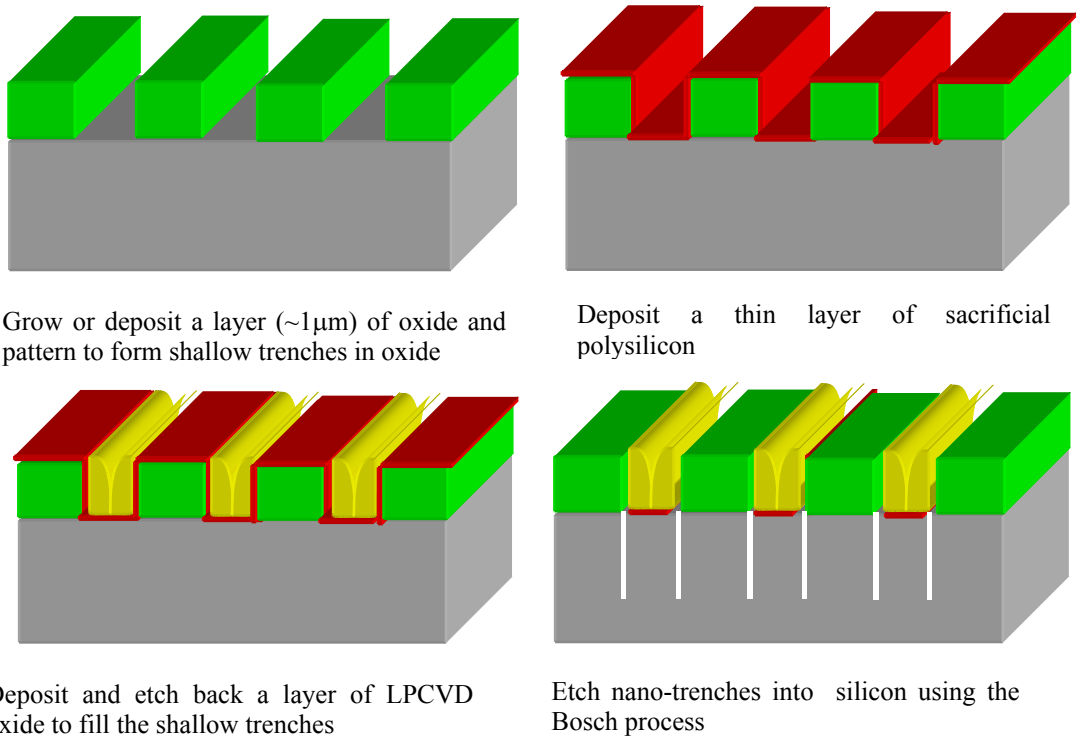

Figure 3.1. Process steps for fabrication of self-aligned nano-trenches.

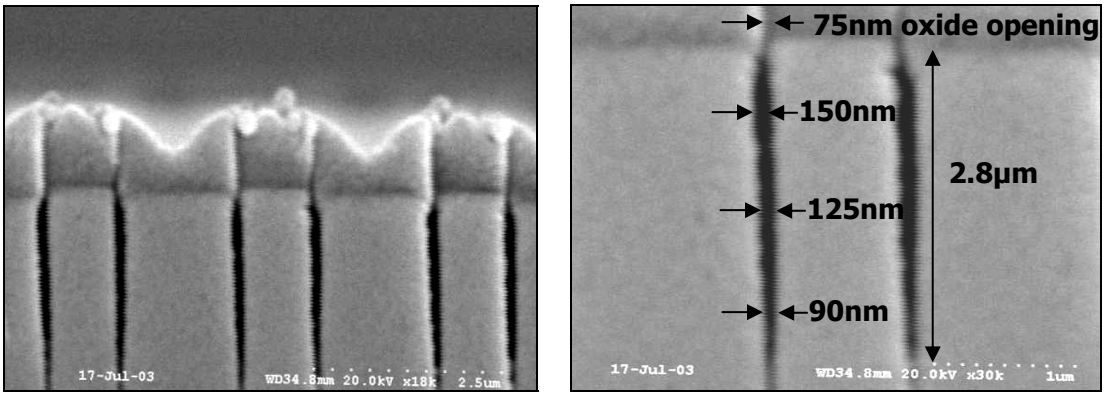

Figure 3.2. 130nm wide trenches dry-etched using the sacrificial polysilicon technique and optimized Bosch process.

As seen in Fig. 3.2, the resulting trench is wider than the initial opening in the oxide mask. This is due to the undercut caused by the Bosch process which can not be completely avoided but can be reduced dramatically by proper characterization and

optimization of process parameters. The trenches shown in Fig. 3.2 are the result of an optimized process after extensive characterization and observation of the effect of different parameters on the etch profile. Figure 3.3 shows the trench profile etched through the same oxide mask using the regular silicon etch recipe used for >2μm wide trenches. The undercut and trench sidewall roughness in Fig. 3.3 is much higher than that of Fig. 3.2 resulting in trench width ~0.5μm.

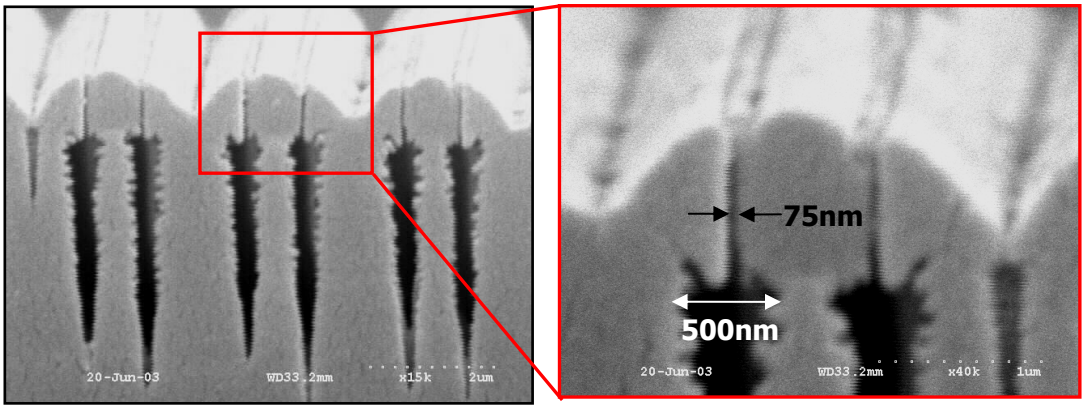

Figure 3.3. Trenches etched into the silicon substrate using the regular silicon DRIE recipe. Etching through 75nm wide oxide openings result in trench width ~500nm due to excessive undercut.

The following modifications were made to the etching recipe in order to improve the trench profile and reduce the undercut and surface roughness, which in turn resulted in the ultra-thin high aspect-ratio trenches of Fig. 3.2: 1) the platen RF power was increased, and the processing pressure was reduced to add to the directionality of the attacking ions in plasma and increase anisotropy; 2) the length of etch and passivation cycles was reduced, so that the amount of silicon etched during each cycle (and consequently the sidewall roughness) is decreased. The processing conditions for both the regular recipe and the optimized recipe are summarized in Table 3.1.

Table 3.1. Process conditions used for nano-trench etching.

	Passivation time (s)	Etching time (s)	Pressure (mTorr)	RF Platten Power (W)	RF Generator Power (W)
Regular Recipe	5	7	20	11	600
Nano-trench Recipe	3	4	8	25	600

Last but not least, for successful etching of narrow trenches, it is necessary that the shallow oxide trenches formed in the first oxide layer have completely vertical or very close to vertical sidewalls. If the trench sidewalls are not vertical, the directional access of the anisotropic etch plasma to the silicon substrate will not be efficient. In order to achieve vertical sidewalls for the oxide shallow trenches, negative photoresist with properly adjusted exposure time was used to pattern the initial oxide. Figure 3.4 shows the cross-section of shallow trenches of oxide with vertical sidewalls etched using negative photoresist (NR7-1500P from Futurrex).

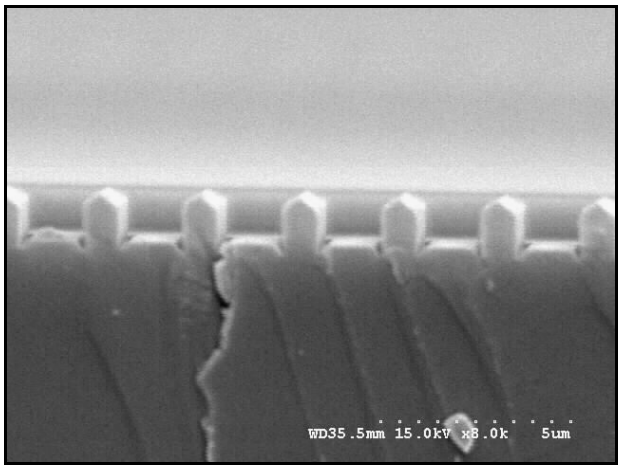

Figure 3.4**.** Cross section of vertical shallow trenches of oxide etched using negative photoresist.

3.2. Resonator Fabrication and Measurement

The described nano-trench etching technique was utilized to fabricate fully SCS resonators with deep-submicron capacitive transducer gaps. The resonators were fabricated on SOI substrates to facilitate isolation and release undercut of the structures.

Figure 3.5 shows the process steps for batch fabrication of fully SCS resonators with the dry-etched ultra-thin trenches for capacitive transduction. The initial oxide is patterned using negative photoresist so that the resonator body and the wirebonding pads are covered by the initial oxide and narrow vertical trenches are etched in oxide at the electrode locations (Fig. 3.5a). Fabrication sequence continues by deposition of the LPCVD sacrificial polysilicon and refilling shallow trenches with silicon dioxide. LPCVD oxide is then etched back anisotropically to expose sacrificial polysilicon. If etched in this step, nano-trenches will be formed all along the sidewalls of the shallow trenches including around the pads leaving behind undesired thin strips of silicon. Therefore, an extra lithography step is required to remove the LPCVD oxide on the sidewalls of the pads except the electrode area (Fig. 3.5b). The third and last lithography step is to physically anchor the drive and sense electrodes to their pads. For this purpose the shallow trenches are partially extended into the pad area and the extensions will be covered by photoresist (Fig. 3.5c) to protect them against the plasma etch. The nano-trench are then etched and at the same time the silicon substrate is patterned to form the body of the resonators and provide electrical isolation between the electrodes. Finally, the resonators are released in HF and the oxide mask on top is removed at the same time (Fig. 3.5d).

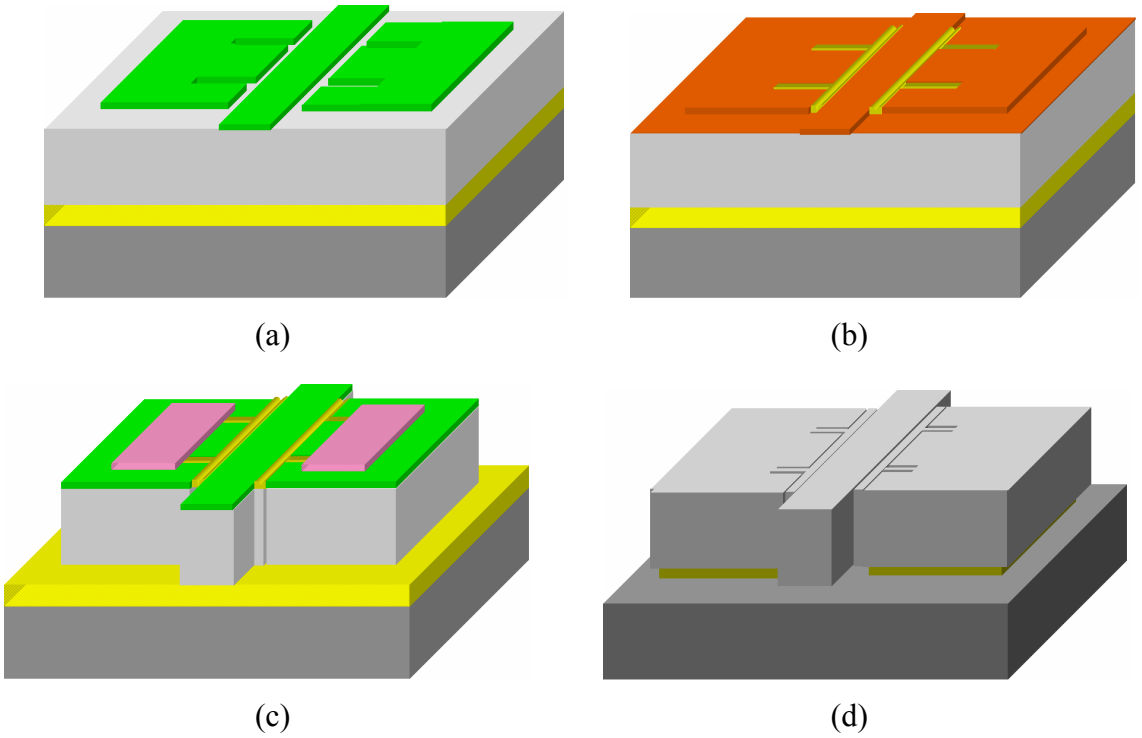

Figure 3.5. Fabrication sequence for fully SCS resonators with dry-etched narrow trenches as transducer gaps: a) Initial oxide growth and patterning (~1μm thick), b) Deposition of sacrificial LPCVD polysilicon, trench refilling with LPCVD oxide, oxide etch back, c) Protection of electrode supports with PR, nano-trench etching and substrate patterning, d) PR removal, resonator undercut in HF

A number of beam resonators with various dimensions and capacitive gap sizes were fabricated on 4-5μm thick low resistivity SOI substrates using the described process sequence. Figure 3.6 shows the SEM view of a fabricated 3.7μm wide, 4μm thick, 54μm long all SCS beam resonator with 200nm capacitive gaps.

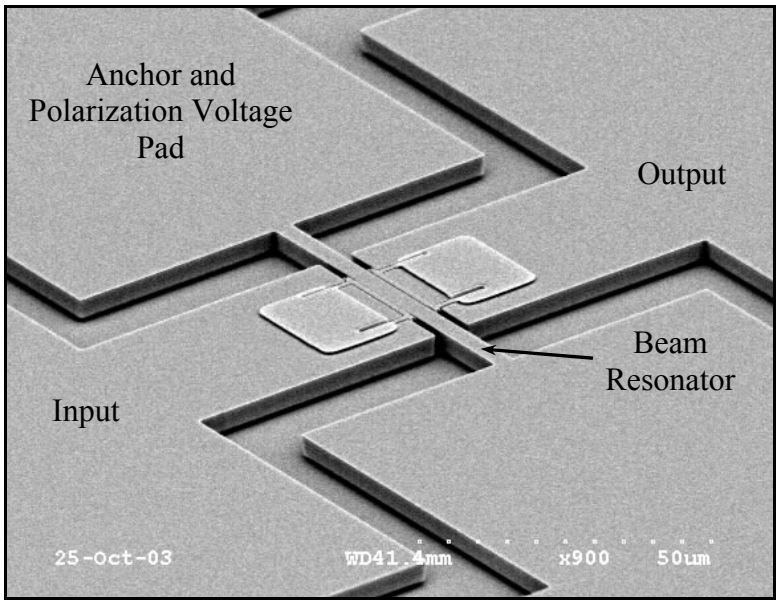

Figure 3.6. SEM view of a 3.7μm wide, 4μm thick, 54μm long all SCS beam resonator with 200nm gaps.

Figure 3.7a shows the close up view of the beam resonator of Fig. 3.6 and Fig. 3.7b is the top view of its electrode area, showing the 200nm capacitive gaps in between the SCS electrodes and the beam resonator. Figure 3.8 shows the cross-section of a 350nm dry-etched vertical capacitive gap between the SCS beam resonator and its SCS electrode.

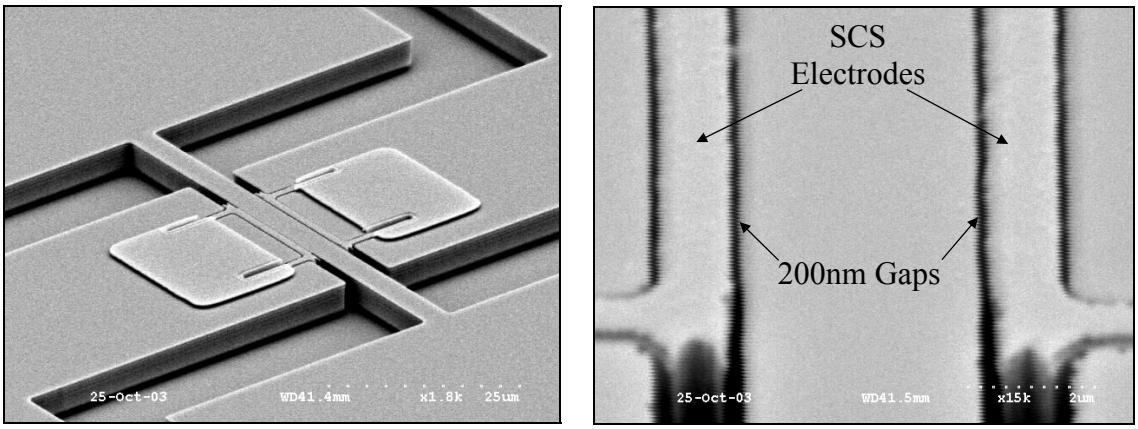

(a) (b)

Figure 3.7. Close-up of the beam resonator of Fig. 3.6 and its electrode area showing the 200nm capacitive gap in between the SCS electrodes and resonator.

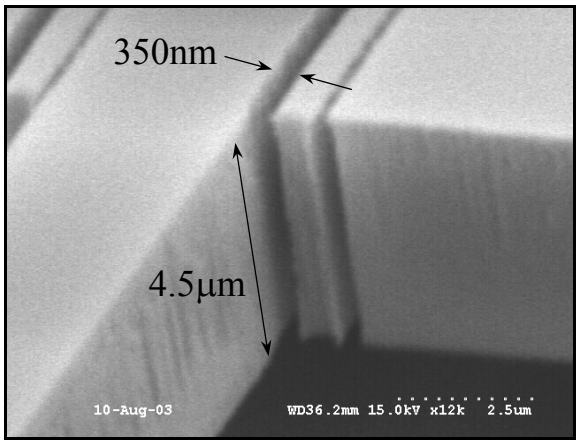

Figure 3.8. Cross-section of a 350nm wide dry etched capacitive gap between the SCS beam resonator and its electrode.

The fabricated beam resonators were tested in a two-port configuration under vacuum using a vacuum probe-station. Figure 3.9 shows the frequency response measured for the fundamental flexural resonant mode of the 3.7µm wide, 54µm long beam resonator of Fig. 3.6. A quality factor of 5,400 was measured for this device at 7.9MHz, which is close to the maximum achievable Q for a beam resonator with such dimensions (limited by support loss).

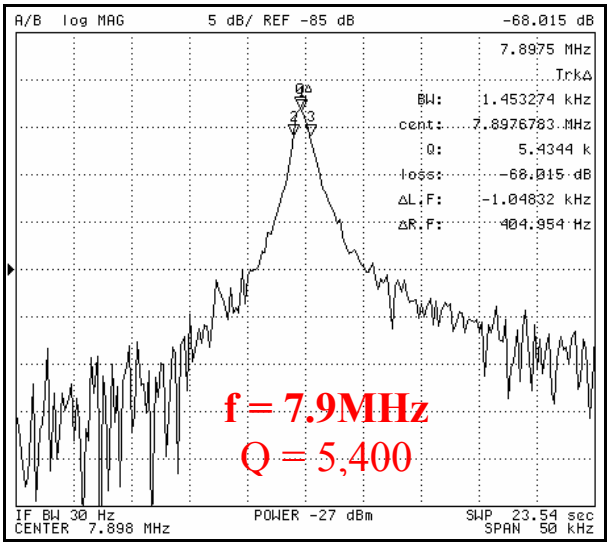

Figure 3.9. Frequency response of the 3.7µm wide, 54µm long beam resonator of Fig. 3.6 in vacuum.

Figure 3.10 shows the frequency response of a 3.7μm wide, 40μm long beam resonator with 350nm capacitive gaps, measured in both vacuum and air. The measured quality factor is 1,800 in vacuum and 300 in air. The lower Q of this beam in vacuum compared to that of Fig. 3.9 is due to its smaller aspect ratio and larger support loss.

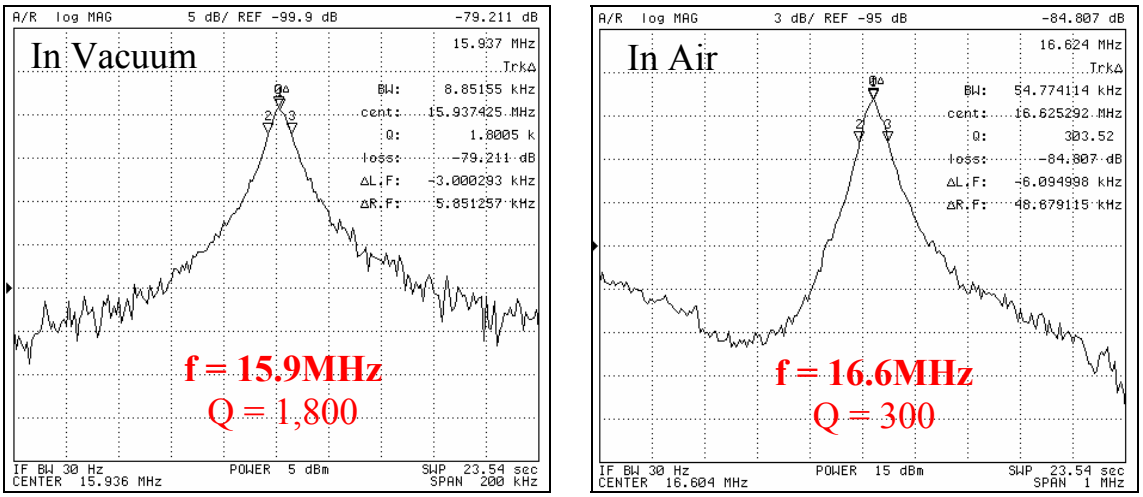

Figure 3.10. Frequency response of a 3.7μm wide, 40μm long fully SCS beam resonator in vacuum and air.

Figure 3.11 illustrates the electrostatic frequency tuning characteristics of the 8MHz beam resonator of Fig. 3.6. A tuning range of 288kHz with tuning slope as high as 950ppm/V has been achieved for this device by changing the polarization voltage from 5V to 70V. According to Eq. 3.1 [26], the measured tuning characteristic confirms a capacitive gap size of ~200nm between the electrodes and the resonator.

$$\frac{\partial f}{\partial V_p} = -\frac{2V_p f \varepsilon A_e}{Kg^3} \tag{3.1}$$

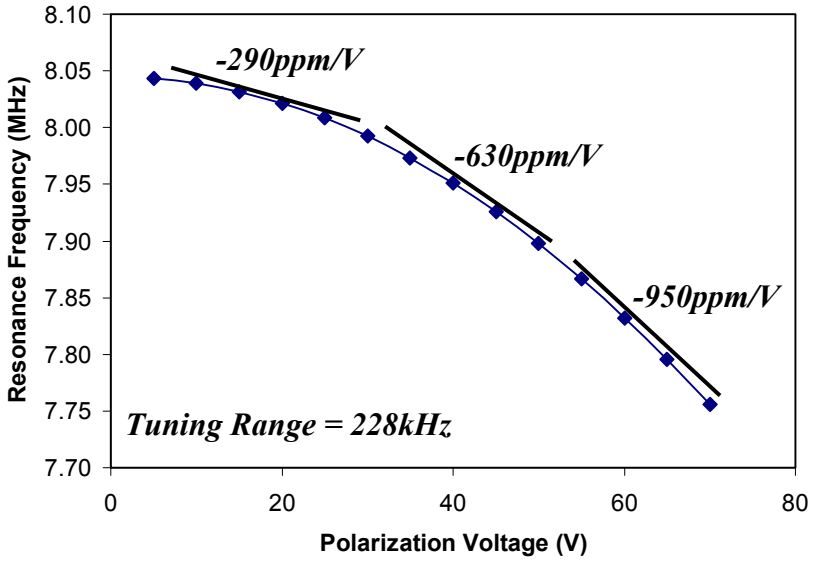

Figure 3.11. Measured electrostatic frequency tuning for the beam resonator of Fig. 3.6 confirming a capacitive gap size of ~200nm.

CHAPTER IV

ELLIPTICAL BULK-MODE DISK RESONATORS

Bulk modes of disk structures have been traditionally used for demonstration of high frequency capacitive MEMS resonators. Polysilicon disks operating in both radial contour mode [16,22] and elliptical mode [19] (also known as wine-glass mode), have been demonstrated. Due to much larger stiffness of the resonator structures operating in their bulk mode, such devices can demonstrate much higher frequencies compared to the flexural modes. Frequencies well in the 100MHz range can be achieved for such modes while having dimensions in the tens of micron range (with silicon as the structural material). Because of popularity and high quality factors illustrated by disk structures, disk resonators were the first to be investigated in this work using the HARPSS process for demonstration of SCS high frequency resonators. For contour mode operation of disk resonators, the resonance node is only at the center of the disk. Therefore, to achieve high quality factors they need to be supported at the center which is not an easy task using the HARPSS process. As a result the work on HARPSS disk resonators was mainly focused on elliptical modes for which there are a number of nodal points around the disk periphery in addition to its center [25-28]. This enables high-Q operation of such devices while being supported from the side at their resonance nodes. The following sections report on modeling, fabrication and testing of elliptical mode HARPSS SCS disk resonators.

4.1. Electromechanical Modeling of Elliptical Bulk-Mode Capacitive Disk Resonators

Figure 4.1 shows ANSYS simulation results for a disk resonator operating in its elliptical bulk mode. In the elliptical (wine-glass) mode, the disk resonator is squeezed along one axis while it expands along the perpendicular axis resulting in an ellipsoid-like deformed shape at resonance. For HARPSS SCS implementation of such resonators the anisotropy of silicon as the structural material has to be taken into account. Typical SOI wafers used for fabrication of resonators in this work have (100) device layers. In the (100) plane, there is a significant direction dependent Young's modulus gradient ranging from 130GPa along <100> direction to 169GPa along <110> direction. Since higher resonance frequencies without excessive dimension shrinkage is desired, <110> direction is considered the better option for fabrication of high frequency SCS resonators. Moreover, much smaller Poisson's ratio of 0.064 in the <110> direction compared to 0.279 in the <100> direction further increases the resonance frequency of bulk modes in <110> direction [44]. Figures 4.1a and 4.1c show finite element analysis of elliptical resonance modes for SCS disks along <110> and <100> directions respectively showing an overall 22% higher resonance frequency along the <110> direction.

Analytical derivations for anisotropic material are far more complicated than isotropic materials. A comparison between resonance modes in anisotropic SCS and isotropic material with similar properties are presented in Fig 4.1. Figure 4.1b and 4.1d show modal analysis results assuming an isotropic structural material with similar mechanical properties (Young's modulus and Poisson's ratio) as of SCS in <110> and <100>

directions respectively. Resulting resonance frequencies turn out to be very close to that of the anisotropic material in both <110> and <100> directions.

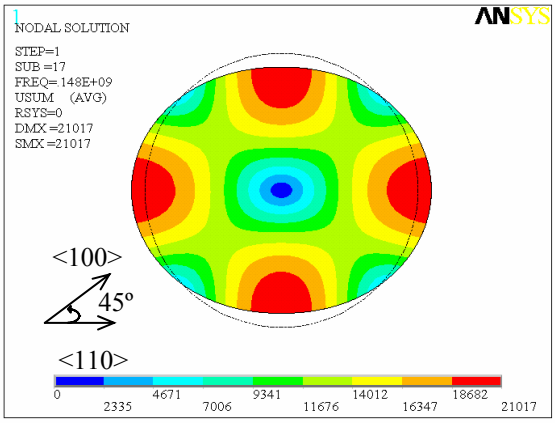

(a) Elliptical bulk-mode along <110> anisotropic material properties of silicon, *f=148MHz.*

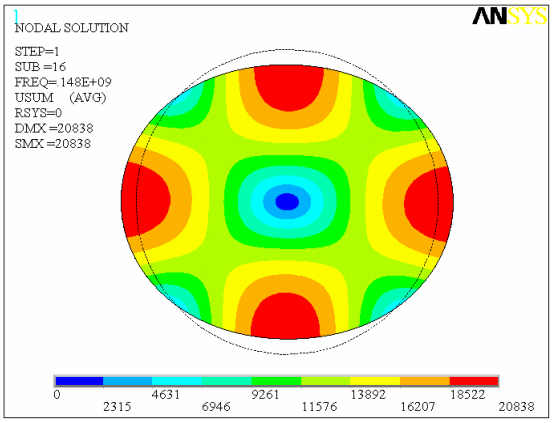

(b) Elliptical bulk mode for isotropic material with properties as of silicon along <110> (*E=169GPa, υ=0.064), f=148MHz*

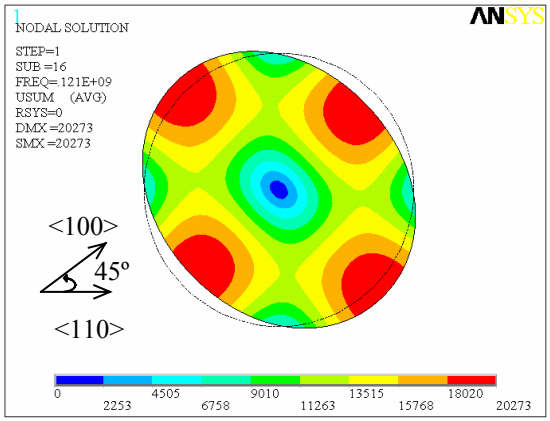

(c) Elliptical bulk-mode along <100>, anisotropic material properties of silicon, *f=121MHz*

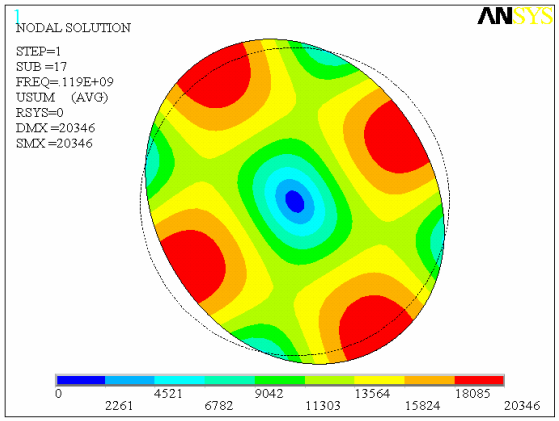

(d) Elliptical bulk mode for isotropic material with properties as of silicon along <100> (*E=130GPa, υ=0.279), f = 119MHz*

Figure 4.1. FEA Analysis results for elliptical bulk-mode of a disk of diameter 29.4μm and thickness 3μm, supported at its center, with the anisotropic and isotropic material properties of single crystal silicon (legend shows the relative displacement distribution across the disk resonator and solid line denotes the undeformed shape).

The resonant frequency for the elliptical bulk mode of a thin disk resonator with isotropic structural material can be calculated using Eq. 4.1 [44]:

$$f_m = \frac{k_m}{2\pi R} \cdot \sqrt{\frac{E}{\rho \cdot (1-\upsilon^2)}} \tag{4.1}$$

where k is the frequency constant and is equal to 1.6002 for SCS in <110> direction, R is the disk radius, and E, ν, and ρ are the Young's modulus, Poisson's ratio, and density of the structural material respectively. According to the simulation results presented in Fig. 4.1, this equation can also be used for anisotropic structural materials such as SCS with good approximation.

Figure 4.2 shows the ANSYS simulation results for a thicker disk resonator (10μm thick, 29.5μm diameter) operating in its elliptical mode. The resonance frequency given by ANSYS for the thicker resonator of Fig. 4.2 is almost equal to the thin ones in Fig. 4.1. As a conclusion equation 4.1 can also be used for prediction of resonance frequency of thick disk resonators with good approximation.

To maximize the resonator quality factors, most of the disk resonators in this work are supported with only one support beam, which is placed at one of the locations with minimum vibration amplitude known as resonance nodes. For operation along <110> direction the resonance node and consequently support beams have to be along <100> direction and vice versa. The electrodes on the other hand need to be placed at locations with maximum vibration amplitude (antinodes) to maximize electromechanical coupling and output current of the resonator.

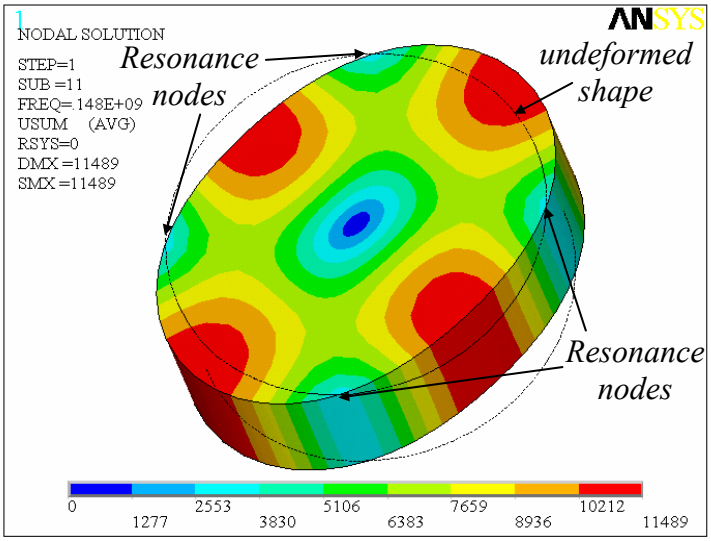

Figure 4.2. ANSYS simulation result for the elliptical resonance mode of a 10μm thick, 29.5μm diameter disk resonator showing its mode shape. The resonance frequency of 148MHz is the same as that of the thin disk presented in Fig. 4.1.

4.1.1. Equivalent Mechanical Model Derivation

A mechanical equivalent model can be used to describe the dynamic behavior of a resonator. To derive a mechanical equivalent model the effective mass, stiffness and actuation forces of the resonator need to be calculated first.

Since the excitation and detection of the capacitive disk resonator is mainly through the gap variation along the radial direction, only the vibration along the radial direction is taken into account here and for simplicity the derivation is done in a polar system (Fig. 4.3). As shown in [44] the radial displacement of the disk resonator in its elliptical mode is simply a sinusoidal function and at the location (r,θ) can be written as [44]:

$$U(r,\theta) = \frac{A}{R} \cdot \cos(2\theta) \cdot U(r) \tag{4.2}$$

where $U(r) = k \cdot J_1(kr') - \frac{2}{r'} \cdot J_2(kr') + \frac{2}{r'} \cdot \xi \cdot J_2(hr')$, is the dimension less normalized vibration amplitude, $r' = r / R$ denotes the dimensionless radial coordinate, normalized to the disk radius R, A is the radial vibration amplitude, k and ζ are constant given in Table 4.1 and $h = k.\sqrt{2/(1-\upsilon)}$. J_1 and J_2 are Bessel functions.

Figure 4.3, shows an infinitesimal element as the reference point which is on the disk edge and along the circumferential direction θ. The effective mass for the infinitesimal element, $d\theta$, is proportional to its physical mass and its vibration amplitude squared [34].

$$m(\theta) = \rho \cdot h \cdot R^2 \cdot \Sigma / U_R^2 \cdot d\theta \tag{4.3}$$

where $U_R = k \cdot J_1(k) - 2 \cdot J_2(k) + 2 \cdot \xi \cdot J_2(h)$ is the dimensionless constant for maximum radial displacement at the disk edge [44] and $\Sigma = \int_0^1 U_r^2 \cdot r' \cdot dr'$ is the integral for the kinetic energy. Both Σ and U_R are listed in Table 4.1 for different silicon-based material properties.

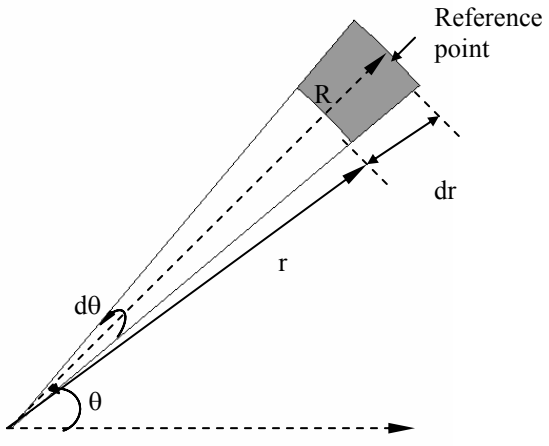

Figure 4.3. An infinitesimal element $d\theta$ on the edge of the disk along the circumferential direction, θ

Table 4.1. Constants related to the disk resonator elliptical bulk mode.

Materials	Single crystal silicon <110>	Single crystal silicon <100>	Polysilicon
Poisson's ratio (υ)	0.064	0.279	0.22
Frequency parameter (k)	1.6002	1.4082	1.4638
Ratio (ξ)	-2.1920	-2.1865	-2.2144
Dimensionless maximum radial displacement at the edge (U_R)	-1.4469	-1.4984	-1.5047
Dimensionless circumferential displacement at resonant nodes (V_R)	0.3719	0.4613	0.4459
Integral for the kinetic energy (Σ)	0.7522	0.8272	0.8294
Effective mass Coefficient (Σ/U_R^2)	0.3593	0.3684	0.3663

The dynamic behavior of this infinitesimal element along the circumferential direction θ can be described by the second-order equation of motion as below:

$$\left\{ m(\theta)\cdot\frac{d^2}{dt^2}\left[\frac{A}{R}\cdot U_R\right] + c_d\cdot\frac{d}{dt}\left[\frac{A}{R}\cdot U_R\right] + K(\theta)\cdot\left[\frac{A}{R}\cdot U_R\right]\right\}\cdot\cos(2\theta) = f_e(\theta) \quad (4.4)$$

where c_d is the damping-related coefficient for this element and $f_e(\theta)$ is the radial electrostatic force per unit radian from the drive and sense electrodes. Multiplying Equation 4.4 by the mode shape of $\cos(2\theta)\cdot U_R$ and integrating both sides of this equation, from 0 to 2π, gives rise to:

$$\begin{aligned} &\pi\cdot\rho\cdot h\cdot R^2\cdot\frac{\Sigma}{U_R^2}\cdot\frac{d^2}{dt^2}\left[\frac{A}{R}\right] + C_d\frac{d}{dt}\left[\frac{A}{R}\right] \\ &+\pi\cdot\rho\cdot h\cdot R^2\cdot\frac{\Sigma}{U_R^2}\cdot\omega^2\cdot\frac{A}{R} = \frac{1}{U_R}\cdot\int_0^{2\pi} f_e(\theta)\cdot\cos(2\theta)\cdot d\theta \end{aligned} \quad (4.5)$$

where A/R and C_d are the radial vibration amplitude and damping coefficient of the disk resonator, respectively. $\omega=2\pi f$ is the angular frequency of the elliptic bulk-mode. Hence, the equivalent mass and equivalent stiffness are, respectively, expressed as:

$$M = \pi \cdot \rho \cdot h \cdot R^2 \cdot \Sigma / U_R^2 \tag{4.6}$$

$$K = M \cdot \omega^2 \tag{4.7}$$

where Σ / U_R^2 denotes the effective mass coefficient, as listed in Table 4.1. Effective mass coefficient is the ratio of the effective mass to the real physical mass of the disk resonator.

The capacitive gap is extremely small compared with the disk radius. Therefore, the capacitances for the drive and sense electrodes can be calculated using a parallel-plate model. Thus, the electrostatic excitation force per unit radian from the drive and sense electrodes, respectively, can be calculated as:

$$f_d(\theta) = \frac{1}{2} \cdot \frac{\varepsilon \cdot h \cdot R}{g_d^2} \cdot \left\{ -2 \cdot V_p \cdot v_d + 2 \cdot \frac{A}{R} \cdot \frac{U_R \cdot \cos(2\theta)}{g_d} \cdot V_p^2 \right\} \tag{4.8}$$

$$f_S(\theta) = \frac{1}{2} \cdot \frac{\varepsilon \cdot h \cdot R}{g_S^2} \cdot \left\{ 2 \cdot \frac{A}{R} \cdot \frac{U_R \cdot \cos(2\theta)}{g_S} \cdot V_p^2 \right\} \tag{4.9}$$

where g_d and g_s are the capacitive gaps for the drive and sense electrodes, respectively, and ε denotes the permittivity of air.

Substituting the above two equations into Equation (4.5) gives rise to the equivalent electrostatic stiffness and the equivalent force for the elliptic bulk-mode, respectively, expressed as:

$$K_e = \varepsilon \cdot h \cdot R \cdot \left(\frac{\theta_e}{2} + \frac{\sin(2\theta_e)}{4} \right) \cdot V_p^{\,2} \cdot \left\{ \frac{1}{g_d^3} + \frac{1}{g_s^3} \right\} \tag{4.10}$$

$$F = \frac{\varepsilon \cdot h \cdot R}{g_d^2 \cdot U_R} \cdot (-V_p \cdot v_d) \cdot \sin(\theta_e) \tag{4.11}$$

Hence, the equivalent mechanical model for describing the dynamic behavior of the disk resonator can be further expressed as:

$$M \cdot \frac{d^2}{dt^2}\left[\frac{A}{R}\right] + C_d \frac{d}{dt}\left[\frac{A}{R}\right] + (K - K_e) \cdot \frac{A}{R} = F \tag{4.12}$$

Taking into account the tuning effect of the polarization voltage through combining Equations (4.10) and (4.12), the resonant frequency of this device can be calculated by:

$$f_{tuned} = f \cdot \sqrt{1 - \varepsilon \cdot h \cdot R \cdot \left(\frac{\theta_e}{2} + \frac{\sin(2\theta_e)}{4} \right) \cdot V_p^{\,2} \cdot \left[1/g_d^3 + 1/g_s^3 \right] / K} \tag{4.13}$$

It can be seen from Equation (4.13) that the frequency-tuning capability of the device strongly depends on the capacitive gaps and the polarization voltage. Since fabrication tolerances are unavoidable, it is necessary to tune the frequencies of the disk resonators when deployed as arrays. As the disk scales down for higher frequencies with the other design parameters fixed, its frequency-tuning capability is decreased. In order to maintain certain frequency-tuning capability, it is required that either the capacitive gaps decrease

or the polarization voltages increase. It is worth noting that these two design parameters are limited by linearity in the device characteristics.

4.1.2. Equivalent Electrical Model Derivation

The resonators investigated in this work are expected to be used as electronic components and interact with other electrical components in an electronic system. Therefore, study of the electrical behavior of such devices by derivation of their equivalent electrical circuit is of great importance.

As shown in Fig. 4.4, the two-port electrical equivalent circuit model for the disk resonator can be developed by derivation of its four *Y*-parameters (admittance parameters), which are defined as the ratio of the current measured at one port to the drive voltage at one of the ports while the other port of the circuit is shorted to ground.

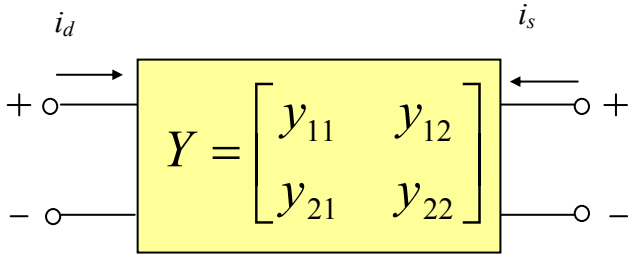

$$Y_{11}(j\omega) = \left.\frac{i_d(j\omega)}{v_d(j\omega)}\right|_{v_s = 0}, \quad Y_{12}(j\omega) = \left.\frac{i_d(j\omega)}{v_s(j\omega)}\right|_{v_d = 0}, \quad Y_{21}(j\omega) = \left.\frac{i_s(j\omega)}{v_d(j\omega)}\right|_{v_s = 0}, \quad Y_{22}(j\omega) = \left.\frac{i_s(j\omega)}{v_s(j\omega)}\right|_{v_d = 0}$$

Figure 4.4. Y-parameter representation of a generic two-port electrical circuit. i_s, v_s, i_d, and v_d are the current and voltage measured at the sense electrode (Port 2) and drive electrode (Port 1), respectively.

For capacitive micromechanical resonators, the admittance parameters can be further expressed in terms of the mechanical force-displacement transfer function for the disk resonator, $Z(j\omega)/F(j\omega)$, and the electromechanical coupling at the input and output ports, η_1, η_2, η_1', and η_2'. Here, the displacement Z denotes the vibration amplitude A/R. The input and output coupling terms are expressed as:

$$\eta_1(j\omega) = \frac{F(j\omega)}{v_d(j\omega)} \tag{4.14}$$

$$\eta_2(j\omega) = \frac{Q_s(j\omega)}{Z(j\omega)} = \frac{1}{j\cdot\omega}\cdot\frac{i_s(j\omega)}{Z(j\omega)} \tag{4.15}$$

$$\eta_1'(j\omega) = \frac{Q_d(j\omega)}{Z(j\omega)} = \frac{1}{j\cdot\omega}\cdot\frac{i_d(j\omega)}{Z(j\omega)} \tag{4.16}$$

$$\eta_2'(j\omega) = \frac{F(j\omega)}{v_s(j\omega)} \tag{4.17}$$

where Q_s and Q_d are the charge going through the sense and drive electrode, respectively. While the electromechanical coupling from the drive electrode to the sense electrode is denoted by η_1 and η_2, the coupling from the sense electrode to the drive electrode is denoted by η_1' and η_2'.

Through combining the above equations, Y_{11} and Y_{21} can be rewritten as [45]:

$$Y_{11}(j\omega) = \frac{Z(j\omega)}{F(j\omega)}\cdot\frac{F(j\omega)}{v_d(j\omega)}\cdot\frac{i_d(j\omega)}{Z(j\omega)} = j\cdot\omega\cdot\frac{Z(j\cdot\omega)}{F(j\cdot\omega)}\cdot\eta_1\cdot\eta_1' \tag{4.18}$$

$$Y_{21}(j\omega) = \frac{Z(j\omega)}{F(j\omega)}\cdot\frac{F(j\omega)}{v_d(j\omega)}\cdot\frac{i_s(j\omega)}{Z(j\omega)} = j\cdot\omega\cdot\frac{Z(j\cdot\omega)}{F(j\cdot\omega)}\cdot\eta_1\cdot\eta_2 \tag{4.19}$$

From Equation (4.12), the force-displacement transfer function of the disk resonator can be expressed as:

$$\frac{Z(j\omega)}{F(j\omega)} = \frac{\dfrac{1}{K \cdot j\omega}}{\dfrac{j\omega}{\omega^2} + \dfrac{1}{\omega \cdot Q} + (1 - K_e / K) \cdot \dfrac{1}{j\omega}} \tag{4.20}$$

where Q is the quality factor of the disk resonator.

Substituting Equation (4.11) into Equations (4.14) and (4.17) gives rise to the following expressions for the voltage-force transfer functions at the sense and drive electrodes:

$$\eta_1(j\omega) = \frac{\varepsilon \cdot h \cdot R}{d_d^2 \cdot U_R} \cdot (-V_p) \cdot \sin(\theta_e) \tag{4.21}$$

$$\eta_2'(j\omega) = \frac{\varepsilon \cdot h \cdot R}{d_s^2 \cdot U_R} \cdot (-V_p) \cdot \sin(\theta_e) \tag{4.22}$$

The displacement-current transfer functions at the sense and drive electrodes can be written as:

$$\eta_1'(j\omega) = \frac{\varepsilon \cdot h \cdot R}{d_d^2} \cdot U_R \cdot \sin(\theta_e) \cdot (-V_p) \tag{4.23}$$

$$\eta_2(j\omega) = \frac{\varepsilon \cdot h \cdot R}{d_s^2} \cdot U_R \cdot \sin(\theta_e) \cdot (-V_p) \tag{4.24}$$

Substituting Equations (4.21) to (4.24) into Equations (4.18) and (4.19) results in the transfer functions in the form of admittance of series RLC tanks with the equivalent inductance, capacitance and resistance expressed, respectively, as below:

$$L_{21} = \frac{K}{\eta_1 \cdot \eta_2 \cdot \omega^2}, \quad L_{11} = \frac{K}{\eta_1 \cdot \eta_1' \cdot \omega^2} \tag{4.25}$$

$$C_{21} = \frac{\eta_1 \cdot \eta_2}{K \cdot (1 - K_e / K)}, \quad C_{11} = \frac{\eta_1 \cdot \eta_1'}{K \cdot (1 - K_e / K)} \tag{4.26}$$

$$R_{21} = \frac{\sqrt{K \cdot M}}{Q \cdot \eta_1 \cdot \eta_2}, \quad R_{11} = \frac{\sqrt{K \cdot M}}{Q \cdot \eta_1 \cdot \eta_1'} \tag{4.27}$$

where R_{21} is commonly referred to as the motional resistance and also denoted by R_m.

Following the same procedure, Y_{12}, and Y_{22} can be derived as:

$$Y_{12} = Y_{21} = Y_{11} \frac{\eta_2}{\eta_1'} = Y_{22} \frac{\eta_1'}{\eta_2} \tag{4.28}$$

Finally, since the two trans-admittance parameters (Y_{12} and Y_{21}) are equal and in the form of the admittance of a series RLC tank, the equivalent circuit model will include a series RLC connecting the two ports. On the other hand, the input and output admittances (Y_{11} and Y_{22}) have the same transfer functions as the trans-admittance parameters scaled by the constant factors, $\frac{\eta_2}{\eta_1'}$ and $\frac{\eta_1'}{\eta_2}$. Adding transformers with the same transformation ratios ($\sqrt{\eta_2} :: \sqrt{\eta_1'}$) to the input and output ports of the RLC tank, will scale the input and output impedances to the required values without changing the trans-admittance parameters.

The equivalent circuit model shown in Fig. 4.5 has all the admittance parameters derived for the resonators and can be used for describing the electrical behavior of the disk resonators. C_{do} and C_{so} are the static capacitances of the drive and sense electrodes, respectively. When interconnect pads are added to the input and output of the resonator, the capacitances related to the pads should be included in C_{do} and C_{so}.

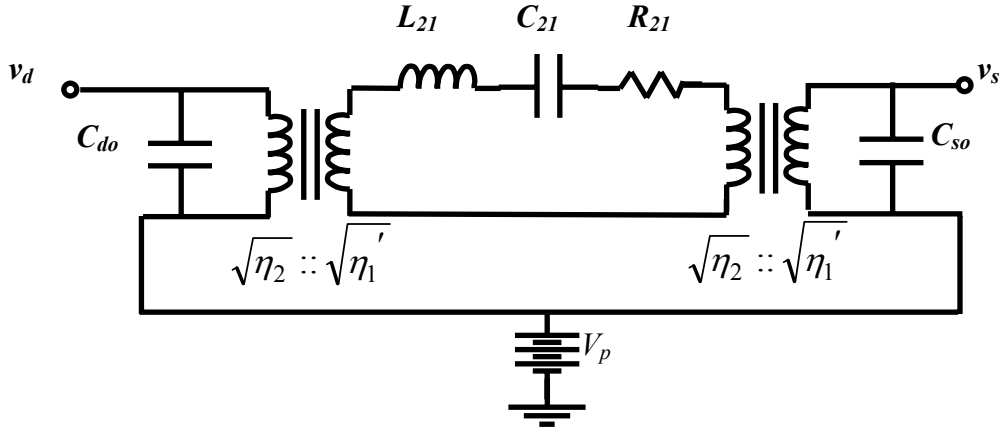

Figure 4.5. The equivalent circuit model for a capacitive disk resonator consisting of a series RLC tank terminated with two transformers at the input and output ports counting for asymmetry between the two electrodes

4.2. Testing and Characterization of High Frequency Disk Resonators

The experimental setup used for measurement of the fabricated disk resonators is illustrated in Fig. 4.6. Unlike low frequency beam resonators for which an amplifier was required to boost the small output signal to detectable levels for the network analyzer, the output signal of the high frequency ultra-stiff resonators can be detected by direct connection to the 50Ω input of the network analyzer. This is mainly due to much larger power handling of such resonators, which is a result of much larger structural stiffness as well as higher operating frequency. Although the resonators still have very large impedance in the MΩ range, resulting in large insertion loss when connected directly to the 50Ω input, larger input signals can be applied to such devices to obtain large enough output signals that can be measured by the network analyzer.

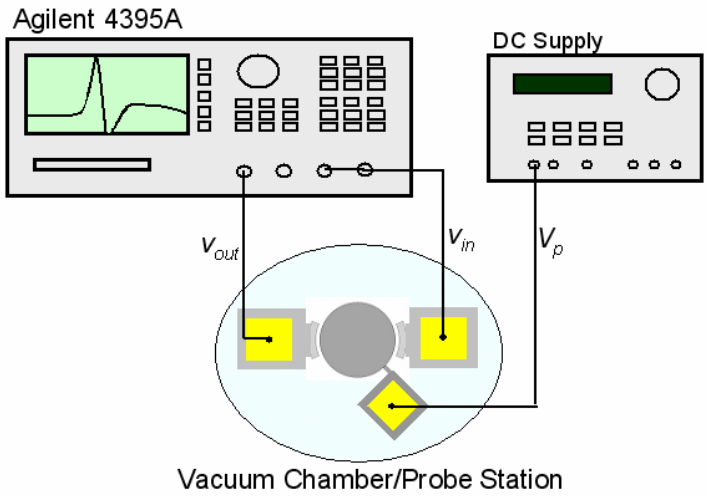

Figure 4.6. Schematic diagram of the test setup for measurement of high frequency resonators.

Figure 4.7 illustrates the frequency response of the 29.4μm diameter, 3μm thick disk resonator that was discussed and shown in Chapter II, Fig. 2.6 under 100mTorr vacuum. The disk is supported by a 1.7μm wide, 2.7μm long support beam at only one resonance node. A quality factor of 39,300 has been measured under vacuum for the elliptical bulk-mode of this resonator at 147.8MHz which is a very high and satisfactory quality factor value for such a high frequency. However, the measured equivalent electrical impedance of 883kΩ for this resonator remains the main drawback for using such devices for real electronic applications. The same disk resonator was also operated in atmospheric pressure and demonstrated a quality factor of 8,200 (Fig. 4.8) with an even higher motional resistance of 2.2MΩ.

For lower frequency flexural mode beam resonators for which the quality factors drops drastically in air to very low values (typically below 100) making the resonance peak very hard or impossible to detect. However, as demonstrated here, higher frequency bulk mode resonators can maintain high quality factors in the tens of thousand under atmospheric pressure. This is primarily due to extremely high mechanical stiffness and larger amount of stored energy in the structure in each resonance cycle for the bulk mode resonators. This is while the amount of energy lost by air damping is pretty much in the same range. Therefore, the percentage of energy lost by air damping compared to the overall stored energy is much smaller for bulk mode resonators resulting much higher quality factors [19-21,25-29].

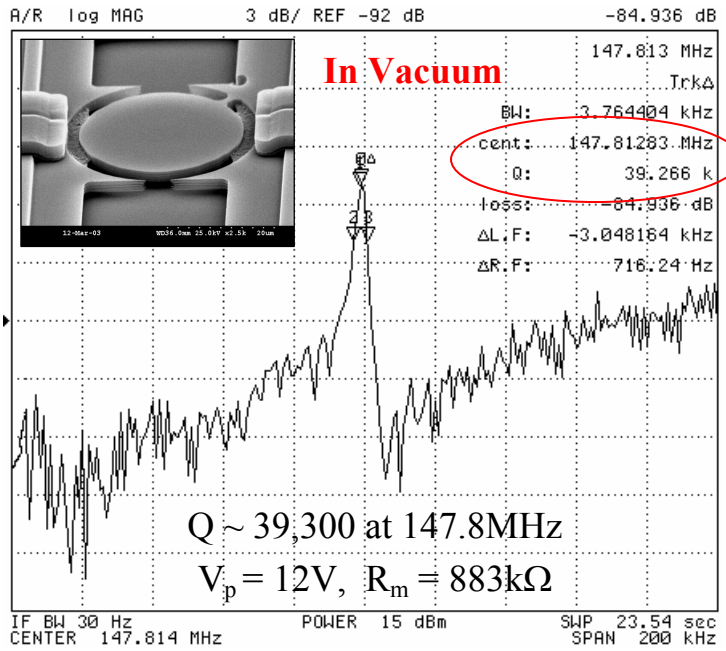

Figure 4.7. Measured frequency response of the 29.4μm diameter, 3μm thick SCS disk resonator of Fig. 2.6 in vacuum.

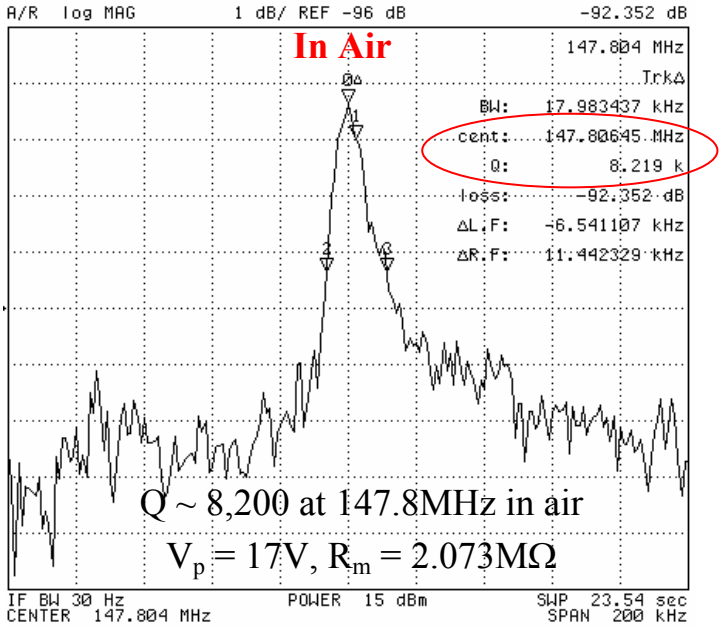

Figure 4.8. Measured frequency response of the 29.4μm diameter disk resonator of Fig. 2.6 in air.

4.2.1. Thick SCS Disk Resonators: Towards Lower Motional Impedance

The luxury of having thick resonant structures with nano-scale gaps provided by the HARPSS-based fabrication processes can be utilized to attack the extremely high motional resistance issue for the high frequency capacitive resonators. As demonstrated in Chapter II, 18μm thick disk resonators were successfully fabricated using the 3-mask HARPSS-On-SOI process (Fig. 2.12). A test setup similar to the one shown in Fig. 4.6 was used to test the fabricated thick disk and block resonators in a two-port configuration.

Figure 4.9 shows the frequency response of the 18μm thick disk resonator of Fig. 2.12, operating in its elliptical bulk mode at 149.3MHz both in vacuum and air. A Quality factor of 25,900 was measured for the 18μm thick resonator in air (Fig. 4.9a), over 3X larger than that of its 3μm thick counterpart (Fig. 4.8). The measured quality factor for the same resonator in vacuum is 45,700 (Fig 4.9b), which is slightly larger than that of the 3μm thick resonator (Fig. 4.7).

Comparing the frequency plots in Figs. 4.7, 4.8 and 4.9, improved signal to noise ratio for the thicker resonator is apparent. Despite having larger capacitive gap size, over 20X lower motional resistances (43.3kΩ in vacuum and 91.2kΩ in air) was measured for the 18μm thick resonator comparing to the 3μm thick resonator. Lower motional resistance is partly due to increased number of electrodes in the design and partly due to much larger device thickness. Two times larger sense and drive electrode effective area means two times larger actuation force and two times larger sensitivity resulting in a total

of four times lower motional resistance. In addition, 6 times larger device thickness results in an additional 6X lower motional resistance for the resonator.

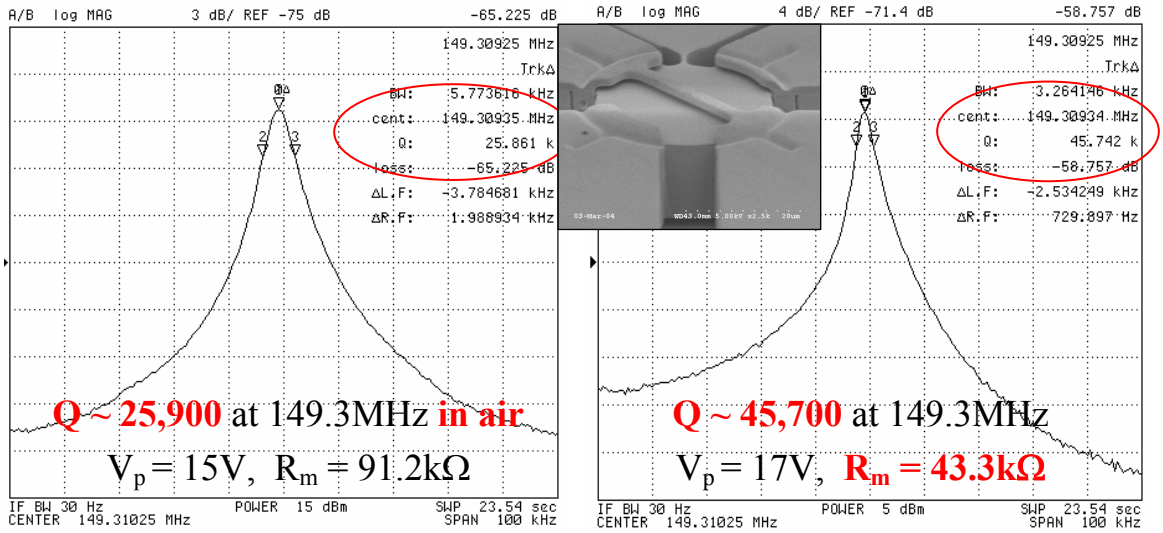

(a) (b)

Figure 4.9. Frequency response of the 18µm thick, 29.2µm diameter disk resonator: (a) in air, (b) in vacuum.

Figure 4.10a shows the frequency response and SEM view of a single support 10µm thick, 19.0µm diameter disk under vacuum showing a quality factor of 35,500 at resonance frequency of 229.5MHz. The capacitive gap size for this resonator is 75nm which is the smallest capacitive gap size demonstrated using the HARPSS process for disk resonators and represents a gap aspect ratio of over 130. Such large aspect ratio can not be achieved using any of the available anisotropic plasma etching tools. Due to very small size of capacitive gaps (75nm) and large resonator thickness, comparatively low motional resistance is measured for this resonator with polarization voltage of only 8 volts. The old electrode layout has been used for this resonator which incorporates only

two electrodes on the two sides of the disk and yet a four times decrease in the motional resistance for the same resonator can be achieved by using the new design with four electrodes. Figure 4.10b is the frequency response of a similar resonator with a diameter of 29.0μm, showing a quality factor of 48,800 at resonance frequency of 150MHz operating with a polarization voltage of only 3V.

Table 4.2 summarizes the measurement results for different disk resonators and compares them to the calculated values using Eq. 4.27 showing excellent agreement between measurement and theory.

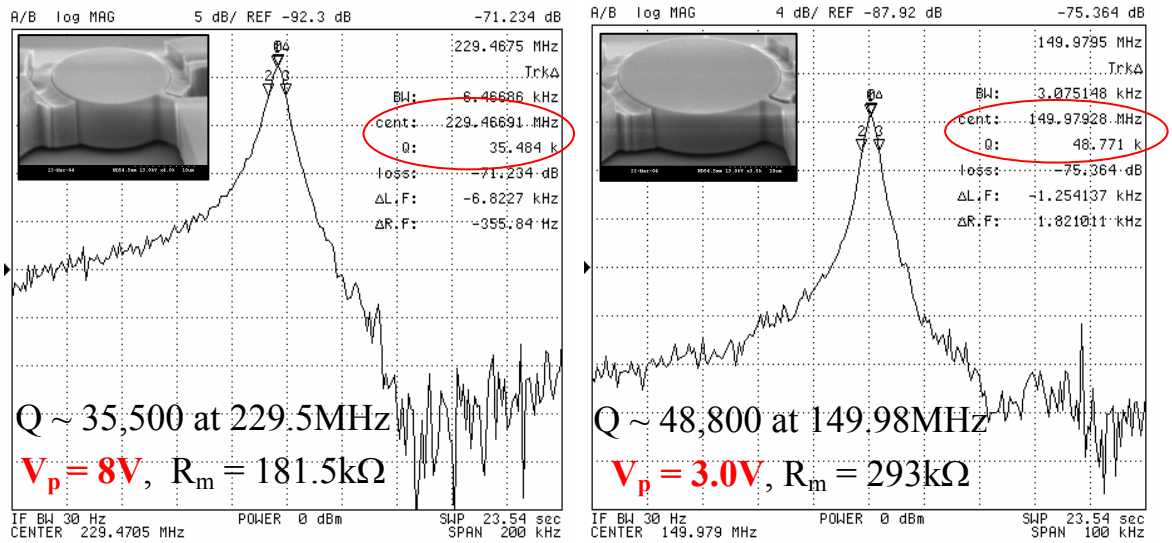

Figure 4.10. Frequency response of 10μm thick, single support disk resonators with 75nm capacitive gaps under vacuum: (a) D = 19.0μm, (b) D = 29.0μm.

Table 4.2. Comparison of the measurement results for different disk resonators with the calculated values.

Resonator Dimensions (μm)	f_{meas} (MHz)	f_{calc} (MHz)	Gap Size (nm)	Q_{vac}	$R_{meas,vac}$ (kΩ)	$R_{calc,vac}$ (kΩ)	f.Q Product ($\times 10^{12}$)
D = 29.4 h = 3	147.8	148.0	120	39,300	883 (V_p=12)	756	5.8
D = 29.2 h = 18	149.3	149.0	160	45,700	43.3 (V_p=17)	42.6	6.8
D = 29.0 h = 10	150.0	150.0	75	48,800	293 (V_p=3.0)	339	7.3
D = 19.0 h = 10	229.5	228.9	75	35,500	182 (V_p=8.0)	179	8.1

CHAPTER V

CAPACITIVE SILICON BULK ACOUSTIC WAVE RESONATORS

High frequency disk resonators operating in their elliptical bulk modes with high quality factors were demonstrated in the previous chapter. Based on the electromechanical equivalent model derived in the previous chapter it can be shown that, although very challenging, impedances in the sub-kiloOhm range are achievable for VHF disk resonators by aggressive pushing of the fabrication limits towards smaller gap sizes and larger device thickness. However, for higher operating frequencies in the UHF range, disk resonators will have diameters smaller than 15μm. Hence, the available area for sensing and actuation will be extremely limited resulting in even higher impedances. On the other hand, excessive reduction of the gap size will eventually result in non-linearity and limit the dynamic range of the device. Moreover, the maximum applicable bias voltage reduces by decreasing the gap size and partially cancels the effect of gap size reduction on the electrical impedance of the resonator.

The abovementioned limitations for the disk structures motivated development and characterization of a new category of resonators based on the longitudinal modes of block structures. Such resonator structures known as Silicon Bulk Acoustic Wave Resonators (SiBAR) can have high frequency bulk resonance modes while maintaining a comparatively large transduction area to alleviate the impedance and power handling issues significantly. SiBARs enable implementation of low impedance VHF and UHF

capacitive resonators without the need for aggressive reduction of the capacitive gap sizes.

5.1. Electromechanical Modeling of Silicon Bulk Acoustic Wave Resonators

High frequency extensional mode of the in-plane block resonators is a much stronger candidate for implementation of high frequency, low impedance capacitive resonators. The block structure can be enhanced along its non-frequency-determining horizontal dimension (referred to as "length") providing a large transduction area while maintaining its high operating frequency by keeping the same frequency-determining dimension (referred to as "width"). Such resonator structures resemble the high frequency film bulk acoustic wave resonators (FBAR), where a plate of the piezoelectric film is actuated in its thickness mode by the metal electrodes on its two sides. Figure 5.1 shows the schematic view of a piezoelectric FBAR (Figure 5.1a) as well as a capacitive silicon BAR (Figure 5.1b). SiBARs can be considered vertically placed versions of FBARs with a bare silicon resonating membrane that is operated electrostatically in its horizontal width extensional mode.

As opposed to the FBARs where the resonant frequency is determined by the thickness of a deposited piezoelectric film, resonant frequency of the SiBARs is determined by their lithography defined horizontal thickness (width). Therefore, resonators with different resonant frequencies covering a wide range can be fabricated on the same substrates simultaneously. This includes frequencies in the VHF range which can not be implemented using FBAR technology due to the extremely large film thickness required. In addition, frequency tuning capability offered by capacitive transduction mechanism can be used for post-fabrication fine-tuning of the resonators.

Furthermore, as opposed to the disk resonators, resonant frequency of the SiBARs can be scaled up by reducing their width (horizontal thickness) without decreasing the available transduction area.

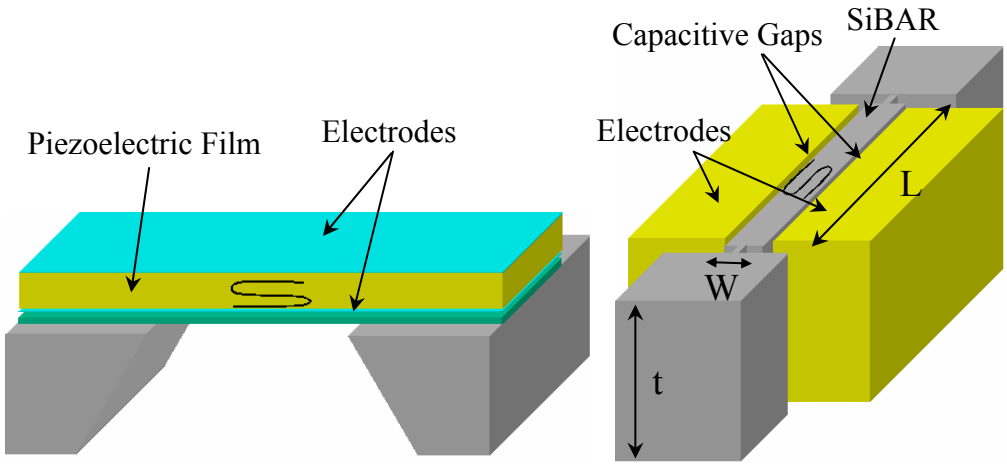

(a) Piezoelectric FBAR (b) Vertical Capacitive SiBAR

Figure 5.1. Schematic diagram of (a) a piezoelectric FBAR and (b) a vertical capacitive SiBAR.

5.1.1. Extensional Mode SCS Block Resonators

The idea of capacitive silicon bulk acoustic resonators (SiBAR) stems from the extensional mode of block resonators. A number of high frequency block resonators designed for operation in their extensional mode were fabricated along with the disk resonators using the 3-mask HARPSS-On-SOI process. Figure 5.2 shows the SEM view of a 30μm long, 20μm wide and 18μm thick block resonator, which is supported by a small support beam on one side. Figure 5.3 shows the ANSYS simulation results

showing the extensional mode shape for this resonator. The support beam is placed in the middle of the block length, which has the minimum vibration amplitude to minimize the support loss and maximize resonator quality factor.

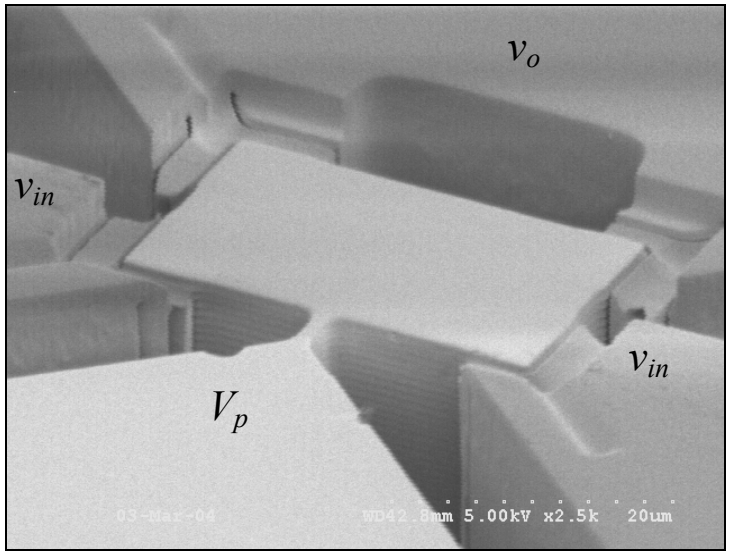

Figure 5.2. SEM view of a 30μm long, 20μm wide, 18μm thick block resonator with 160nm capacitive gaps.

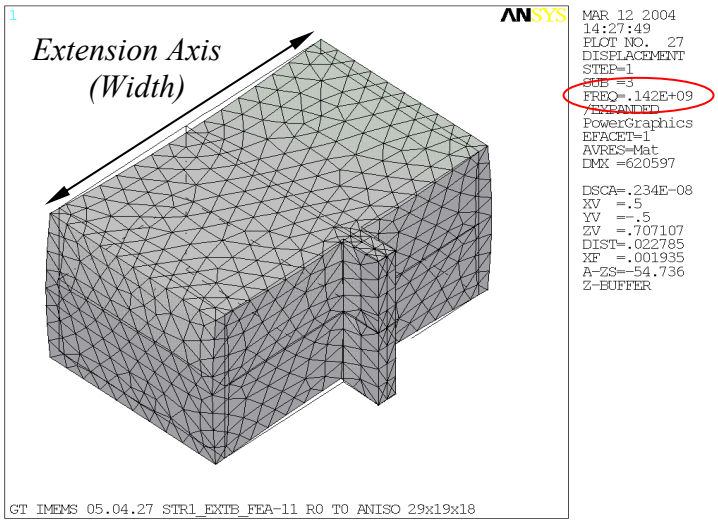

Figure 5.3. ANSYS modal analysis results showing the mode shape for the first extensional mode of a 30μm long, 20μm wide, 18μm thick block resonator.

Figure 5.4 shows the frequency response measured for the block resonator of Fig. 5.2 both in vacuum and air. The measured resonance frequency of 142MHz is in excellent agreement with the simulation results and the measured quality factor values are similar to that of the disk resonators with resonance frequencies in the same range.

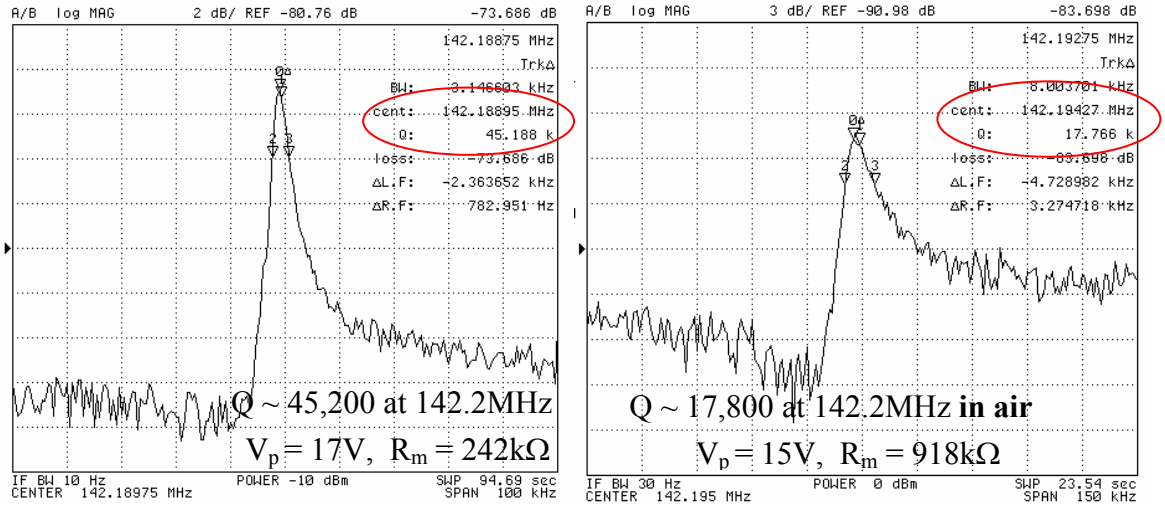

Figure 5.4. Frequency response of the single support block resonator of Fig.5.2 operating in its first extensional mode in vacuum and air.

The resonance frequency for the length extensional mode of a long, narrow and thin block resonator can be calculated using Eq. 5.1:

$$f_n = \frac{n}{2L} \cdot \sqrt{\frac{E}{\rho}} \qquad (5.1)$$

where n is the length extensional mode number, which is an integer (n = 1,2,…), L is the length of the block (for SiBARs the frequency determining dimension is resonator width and L has to be replaced by W), and E, ν, and ρ are the Young's modulus, Poisson's ratio, and density of the structural material respectively.

5.1.2. Equivalent Motional Resistance of SiBARs

Equation 5.2 gives the electrical equivalent resistance for a generic two-port vertical (in plane) capacitive microresonator:

$$R_m = \frac{\gamma\sqrt{KM}\,g^4}{Q\varepsilon_0{}^2 L_e{}^2 t^2 V_p{}^2} \propto \frac{\gamma g^4}{Q.V_p{}^2.L_e{}^2.t} \tag{5.2}$$

where K and M are the effective mechanical mass and stiffness of the resonator, g is the capacitive gap size, Q is the quality factor of the resonator, V_p is the applied polarization voltage, L_e is the physical electrode length, t is the thickness (height) of the structure and γ, which will be referred to as "coupling ratio", is a coefficient indicating how effective the electromechanical coupling between the resonator and the electrodes is. The value of γ varies from 1 for a completely uniform mode shape all along the electrode area, to 0 for a wavy mode shape with complete cancellation.

The effective mass for the extensional mode of a block resonator is half the static mass of the resonator [46], i.e. ($M = \frac{\rho.L.W.t}{2}$), where ρ is the density of the structural material. The effective stiffness can be calculated based on the effective mass and resonance frequency ($K = M\omega^2$).

SiBARs are wide and thick block resonators operating in a similar resonance mode, therefore equation (5.1) can be used to calculate resonance frequency of SiBARs with good approximation. It should be noted that for SiBARs, L in equation 2 has to be replaced by W, which is the frequency determining dimension in this case. To determine

the exact resonance frequency of SiBARs finite element modal analysis needs to be performed for each specific set of dimensions.

The coupling factor γ can be calculated numerically for each mode shape using Equation 5.3:

$$\gamma = \frac{1}{A}\iint_A X(y,z)dydz \tag{5.3}$$

where A is the electrode physical area, y and z indicate the location of each point on the resonator sidewall and $X(y,z)$ is the normalized vibration amplitude at location (y,z) on the resonator sidewall. The vibration amplitude is normalized to the amplitude for a completely undistorted, uniform mode shape (e.g. a thin, narrow block) actuated by the same actuation force density.

Qualitatively, γ is a measure of how flat or distorted the surface of the SiBAR facing the electrodes is at resonance. Since for SiBARs the dimensions (or at least one dimension) of the electrode-facing surfaces, i.e. length and/or thickness, are larger than the acoustic wavelength at the operating frequency, a wavy pattern in the mode shape is usually observed. In other words there is variations in the vibration amplitude along the length and/or thickness of the resonator. Figure 5.5 shows ANSYS modal analysis results showing the width extensional mode shape for SiBARs with the same length and width but different thickness ranging from 0.2×width up to ~1.5×width . As shown by the mode shapes shown in Fig. 5.5, for SiBARs with thickness < ~0.7×width, the width extensional mode is slightly distorted along the length of the resonator but all the points move in phase towards or away from the electrodes at resonance. For SiBARs with thickness > ~0.7×width, the mode shape is significantly distorted and in most cases has

points moving in opposite directions with respect to electrodes. This effect which is observed in FBARs as well [47], results in partial charge cancellation and consequently smaller output signal and larger motional impedance compared to a resonator with a completely flat (or in phase) mode shape. To avoid charge cancellation and maximize the electromechanical coupling, precautions need to be taken in choosing the resonator dimensions.

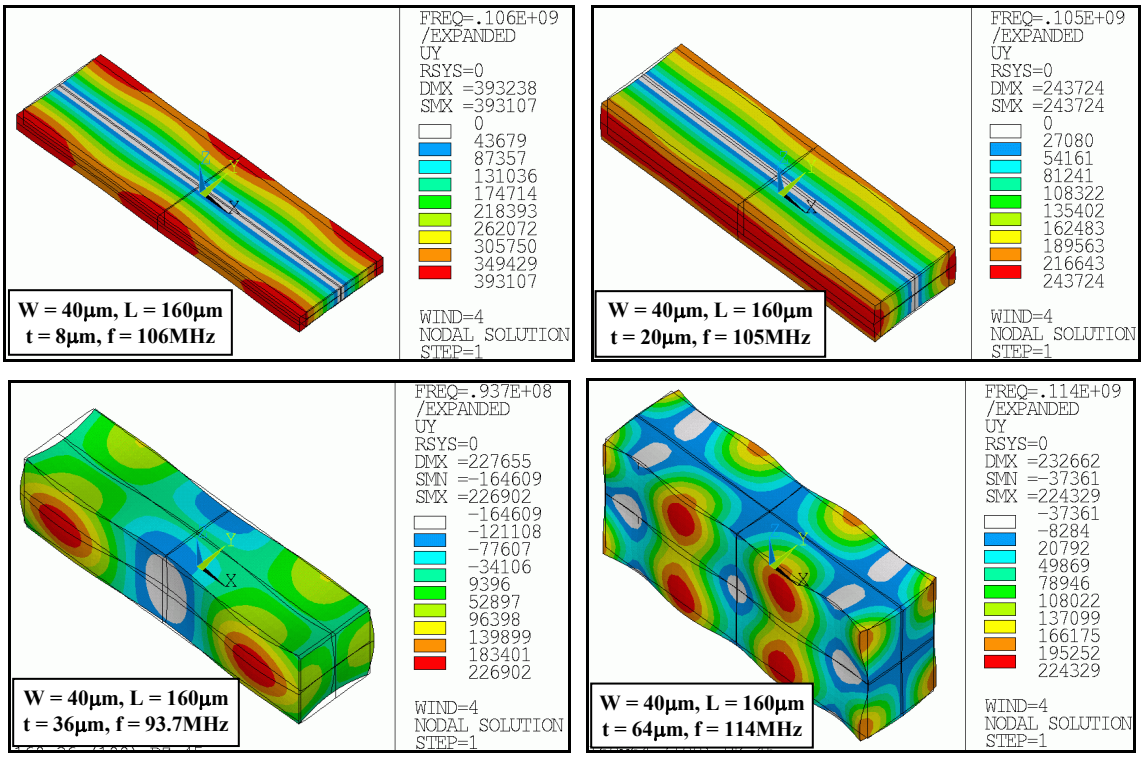

Figure 5.5. ANSYS modal analysis showing the width extensional mode shape for 160µm long, 40µm wide SiBARs with thickness ranging from 8µm to 64µm showing how the mode shape becomes distorted as the resonator thickness increases.

5.2. Fabrication, Measurement and Characterization of Silicon Bulk Acoustic Resonators

The three-mask HARPSS-On-SOI fabrication process [27-29], already demonstrated its viability and versatility by implementation of high Q disk resonators, was used for preliminary demonstration of SiBARs. A wide variety of SiBARs with different dimensions and capacitive gap sizes were fabricated on low resistivity SOI substrates [29]. The detailed measurement and characterization of such resonators is presented in the following sections.

5.2.1 First Generation SiBARs: Matched Support Lengths

Figure 5.6 shows a fabricated 10μm thick, 20μm wide, and 80μm long clamped-clamped SiBAR. The resonator has 225nm capacitive gaps and is supported on its two sides by 3μm wide, 10μm long support beams. Support beams are placed in the midpoint of the resonator width, which has zero vibration amplitude along the width axis. In addition, the length of the supports is chosen to be equal to the quarter wavelength at the operating frequency (half of the BAR width) to match the frequency of the longitudinal mode of the support beam with the width extensional mode of the BAR. Support beam with a matched frequency imposes less resistance against motion of the resonator and can minimize flow of energy to the substrate and maximize the quality factor of the resonator [15,20,21]. Figure 5.7 shows the close-up view of the support area for the same resonator and its capacitive gap.

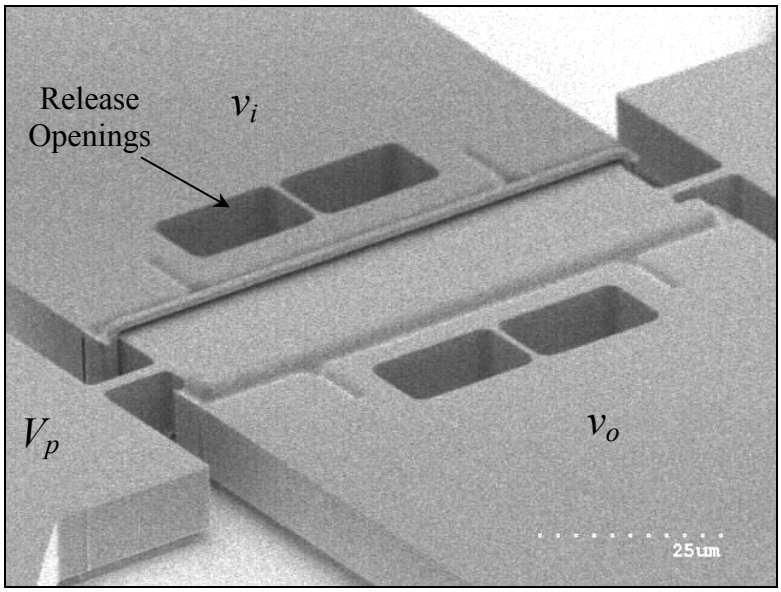

Figure 5.6. SEM view of a 20μm wide, 80μm long, 10μm thick SiBAR with 225nm capacitive gaps.

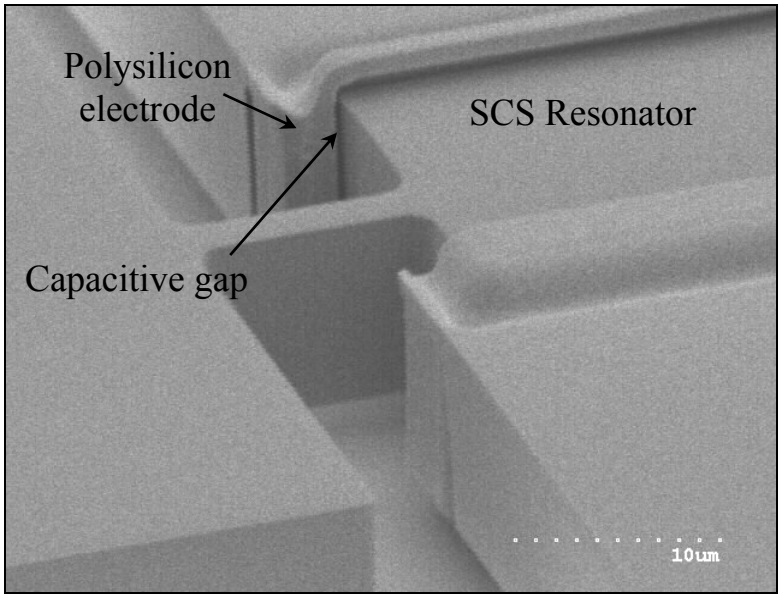

Figure 5.7. Close up of the support area of the SiBAR of Fig. 5.6 showing the 225nm capacitive gap between the polysilicon electrode and SCS resonating body (electrodes cover the edges of the SiBAR).

The rectangular openings in the electrode pads are etched during the last lithography and etching step to facilitate and accelerate resonator undercut in HF.

Fabricated resonators were tested in a two-port configuration using the same test setup as the one used for disk resonators (Fig. 4.6) by direct connection to the network analyzer. Figure 5.8 shows the measured frequency response for the resonator of Fig. 5.6. Quality factors of 28,700 in vacuum and 20,200 in air were measured for the first width extensional mode of this resonator at 213.4MHz. The measured quality factors are in the range of values measured for the side supported SCS disk resonators with similar operating frequency [26-28]. Electrical equivalent resistance as low as 6.3kΩ was measured for this resonator which is close to an order of magnitude lower than the lowest values demonstrated SCS disk resonators [26-28].

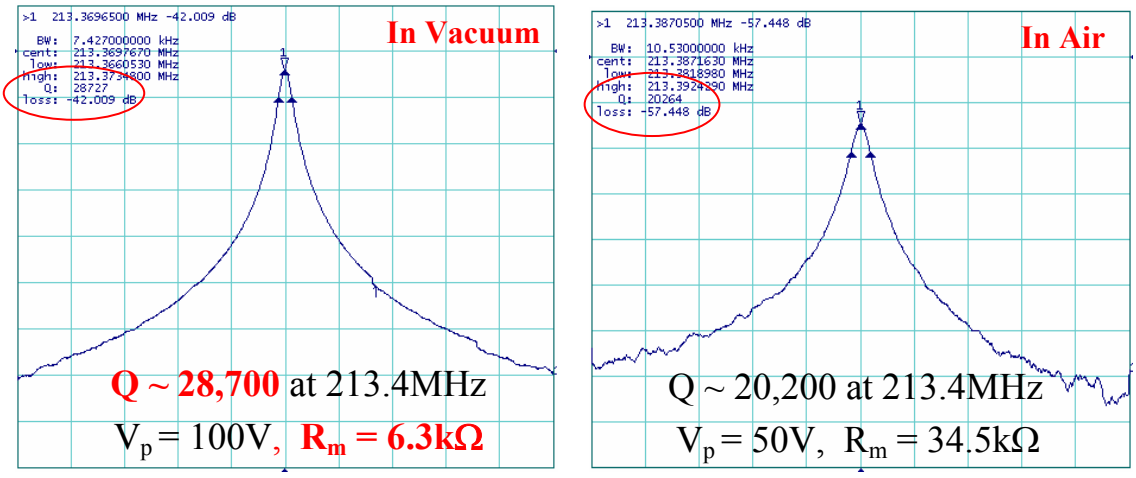

Figure 5.8. Frequency response of the SiBAR of Figure 5.6 in its first width extensional mode in vacuum and air.

Figure 5.9 shows the ANSYS modal analysis for the SiBAR of Fig. 5.6 showing the mode shape for the measured resonance mode of Fig. 5.8. There is a good agreement between the measured resonance frequency and the value given by the simulation.

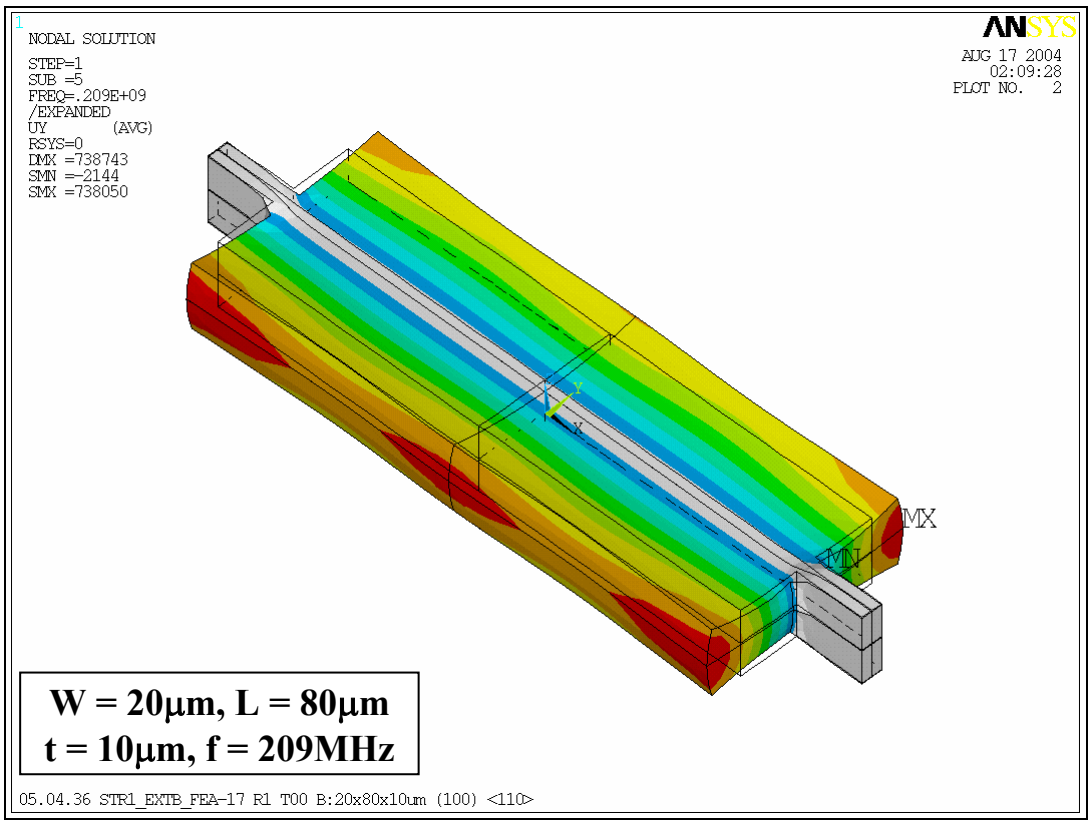

Figure 5.9. ANSYS modal analysis showing the mode shape for width extensional mode of the resonator of Fig. 5.6.

Figure 5.10 shows the measured frequency response and SEM of a 20µm thick, 30µm wide, 300µm long clamped-clamped SiBAR. Quality factor of 39,800 and electrical resistance of 5.5kΩ was measured for the first mode of this resonator at 137.2MHz under vacuum.

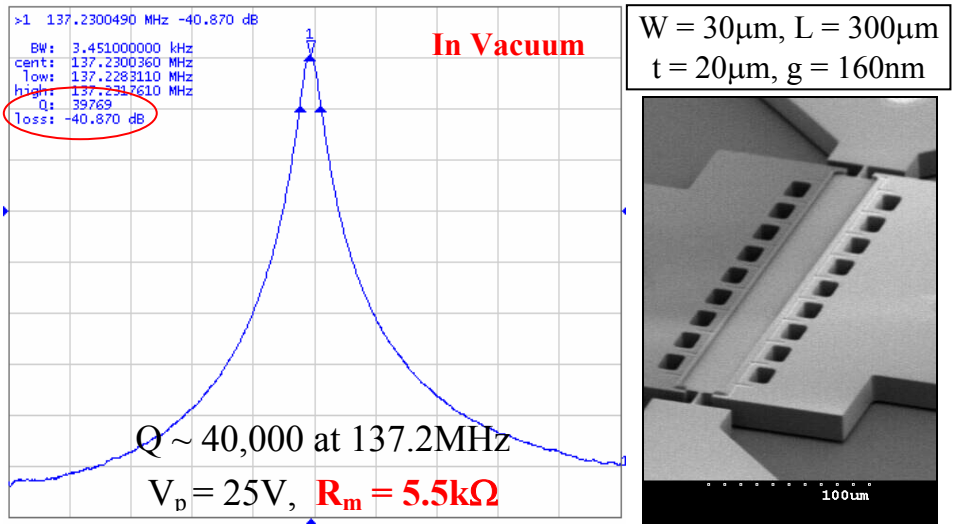

Figure 5.10. Frequency response and SEM view of a 20µm thick, 30µm wide, and 300µm long clamped-clamped SiBARs.

Frequency response as well as the SEM view of a 10µm thick, 15µm wide, and 300µm long SiBAR is shown in Fig. 5.11 showing a quality factor of 24,200 at 281MHz for its first width extensional mode.

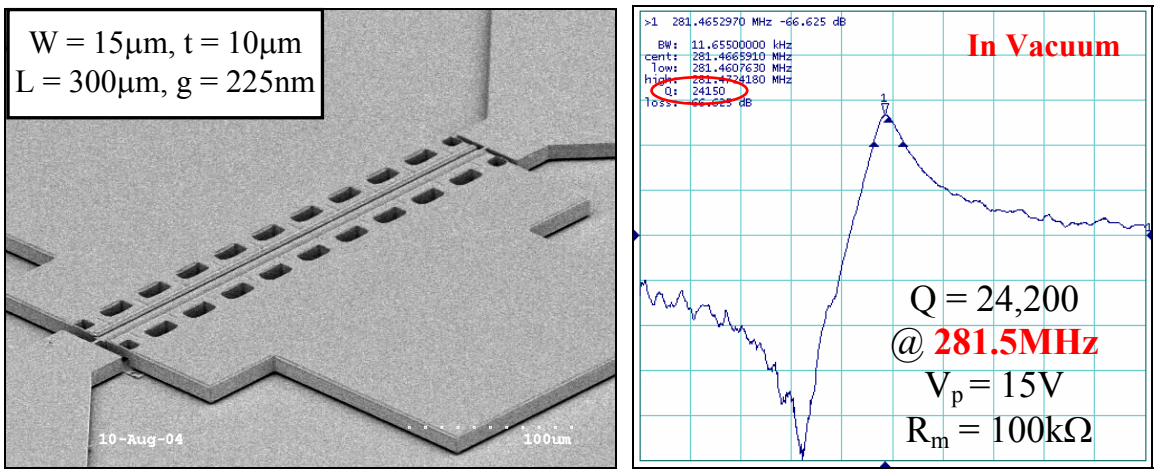

Figure 5.11. SEM view and frequency response of a 10µm thick, 15µm wide, and 300µm long clamped-clamped SiBAR in vacuum.

5.2.2. Second Generation SiBARs: Very Low-Impedance VHF Resonators

SiBARs presented in the previous section [29] demonstrated significant superiority in impedance and power handling over the disk resonators while maintaining high quality factors in the same range. For the previous generation of SiBARs the longitudinal resonance mode of the support beams was matched to the resonance frequency of the BAR by setting the beam length to a quarter wavelength at the operating frequency (half of the BAR width). Although high quality factors were achieved for the SiBARs with quarter wavelength supports, but such comparatively long support beams result in excessive compliance of the resonator structure and reduce their capacity to tolerate large enough polarization voltages. This in turn limits the minimum achievable motional resistances to a few kiloOhms. In the second implementation of SiBARs, very short support beams were used to increase device stiffness without caring about frequency matching and Q-optimization. Surprisingly it turned out that very high quality factors in the tens of thousand can still be achieved for the long SiBAR structures with 3-5μm long support beams [47].

Figure 5.12 is the SEM view of a fabricated 20μm thick, 40μm wide, 150μm long SiBAR as well as the close-up of its 170nm capacitive gap. The resonator is supported on the two sides by 4.5μm long, 2.5μm wide support beams. Similar to the previous devices, support beams are placed in the midpoint of the resonator width.

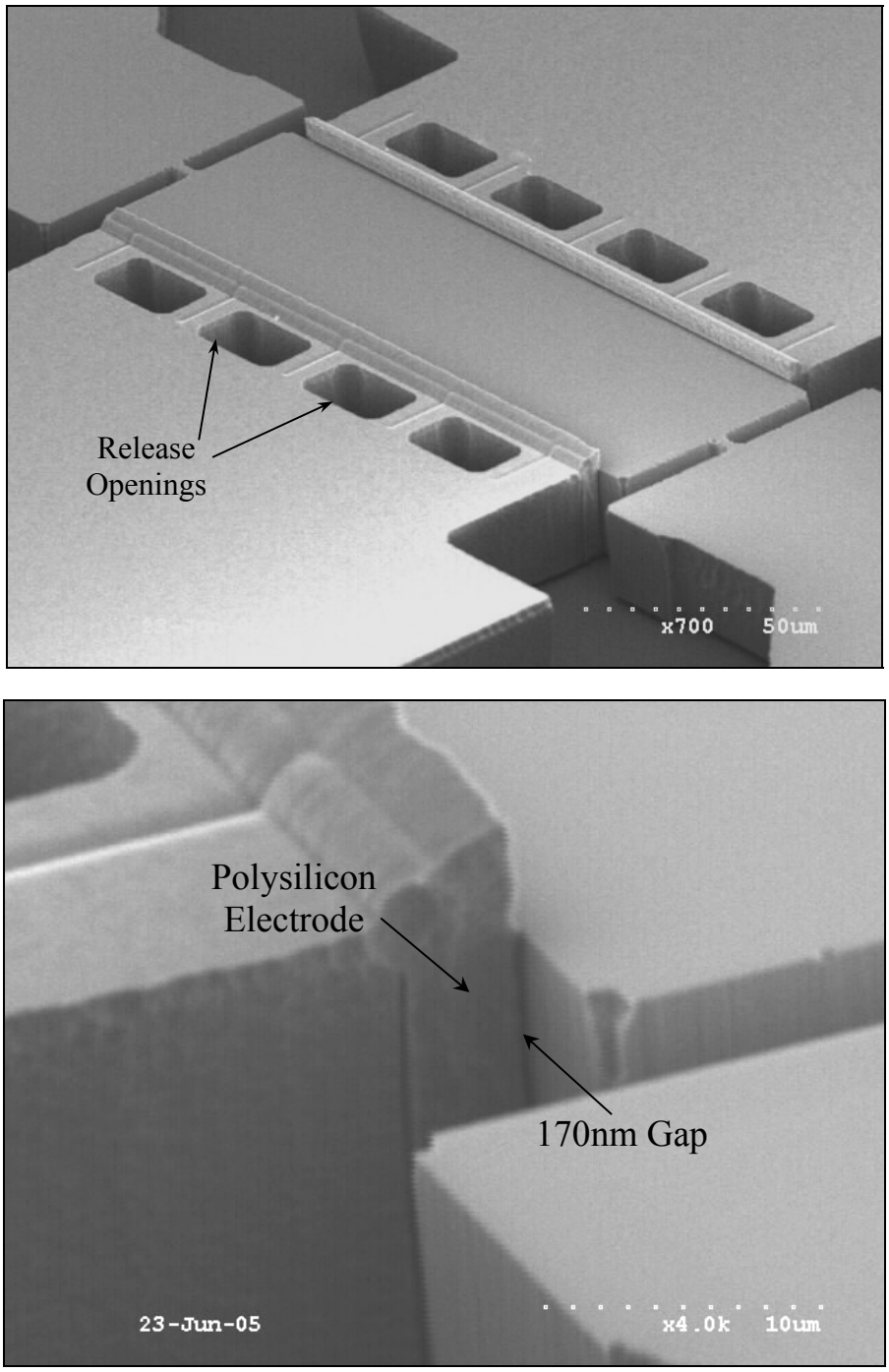

Figure 5.12. SEM view of a 40μm wide, 150μm long, 20μm thick SiBAR and the close up of its electrode showing the 170nm capacitive gap.

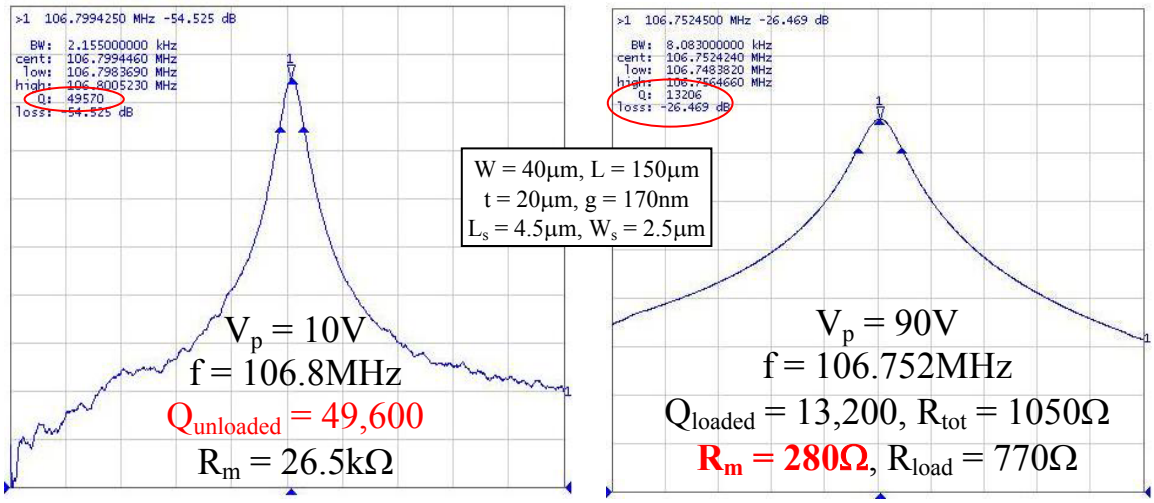

Figure 5.13. Measured frequency response of the 106.8MHz SiBAR of Fig. 5.12 with a) low, and b) high polarization voltage value showing Q loading due to extremely low motional resistance of the resonator.

Figure 5.13 shows the measured frequency response for the 150µm long, 40µm wide, 20µm thick SiBAR of Fig. 5.12. A very clear resonance peak was observed for this resonator by applying polarization voltages as low as 10V (Fig. 5.13a). Quality factor of 49,600 was measured for the first width extensional bulk mode of this resonator (at 106.8MHz) in vacuum. Polarization voltages up to 90V were applied to this resonator resulting in a total measured impedance of 1050Ω. However, the quality factor of the resonator was gradually reduced to 13,200 by increasing the polarization voltage. Reduction of quality factor is a result of existence of parasitic series resistance in the silicon body of the resonator (R_{load}) that loads the intrinsic Q of the resonator. As the impedance of the resonator decreases by increasing the polarization voltage, the effect of the loading resistor on the quality factor, becomes more pronounced (as shown in Eq. 5.4).

$$Q_{loaded} = Q_{unloaded} \frac{R_m}{R_m + R_{load}} \tag{5.4}$$

Using Equation 5.4 and the fact that the total measured impedance at resonance is the sum of the motional resistance of the resonator and the associated parasitic series resistance ($R_{tot} = R_m + R_{load}$), the value of loading resistance and intrinsic motional resistance of the resonator can be extracted. For the resonator of Figure 5.13, the extracted motional resistance is only 280Ω and the related parasitic loading resistance is 770Ω.

Figure 5.14 is another example of a very low impedance 85.9MHz (50μm wide, 300μm long, 20μm thick) SiBAR whose quality factor is being loaded by the series parasitic resistance. Quality factor for this resonator decreases from 77,000 to 22,500 by increasing the polarization voltage from 7V to 60V, which is the result of a 480Ω series loading resistance added to the 200Ω intrinsic motional resistance of the resonator (at V_p = 60V). The same resonator had a Q of 24,400 in air (at low V_p). The extracted motional resistances in the order of 200Ω are the lowest impedance values reported for the high frequency bulk mode capacitive resonators so far and are well within the desired range for RF circuit design applications. The typical values of loading resistances for the fabricated resonators in this work are in the range of 400-1000Ω. The typical values measured for the static physical resistance measured between the two V_p pads on the two ends of the devices is also in the hundreds of Ohm range. Therefore, the resistivity of the silicon substrate in the V_p path is suspected to be responsible for Q loading. To achieve lower overall resistances and avoid Q loading, the resonators should be fabricated on lower resistivity SOI substrates.

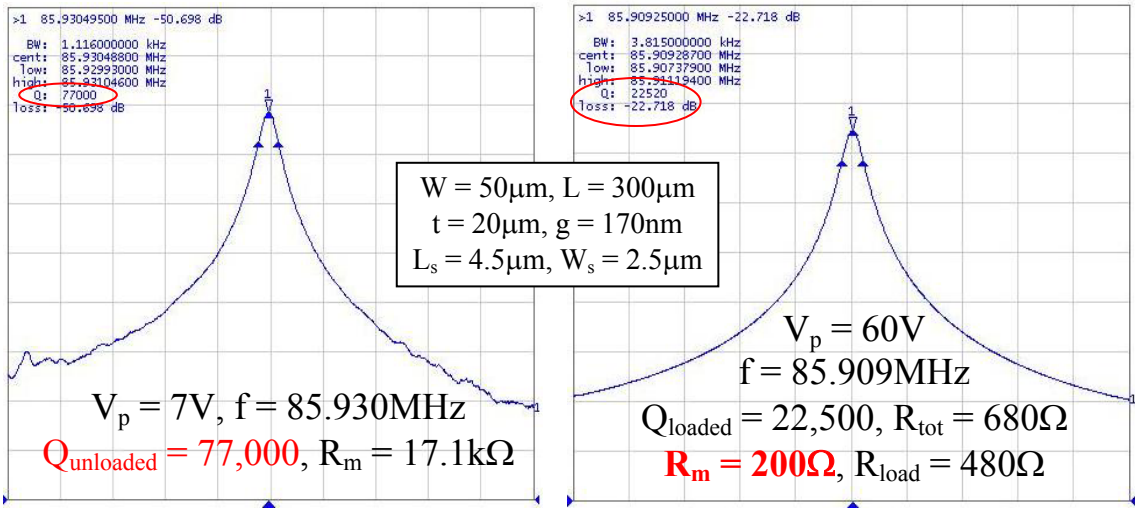

Figure 5.14. Measured frequency response of a low impedance 86MHz SiBAR with different polarization voltages.

The starting SOI substrate for the resonators in Figures 5.13 and 5.14 had a device layer resistivity of 0.015Ω.cm. To further investigate the effect of substrate resistivity on Q loading, another batch of resonators were fabricated on a SOI substrates with lower device layer resistivity (0.002Ω.cm). Figure 5.15 shows the frequency response and extracted resistance values for a 20µm thick, 40µm wide, 300µm long SiBAR with 125nm capacitive gaps (Gap aspect ratio = 160) fabricated on the lower resistivity substrate. The extracted loading resistance for this resonator is only 120Ω which is much lower than the loading resistor for the devices on the previous higher resistivity substrate.

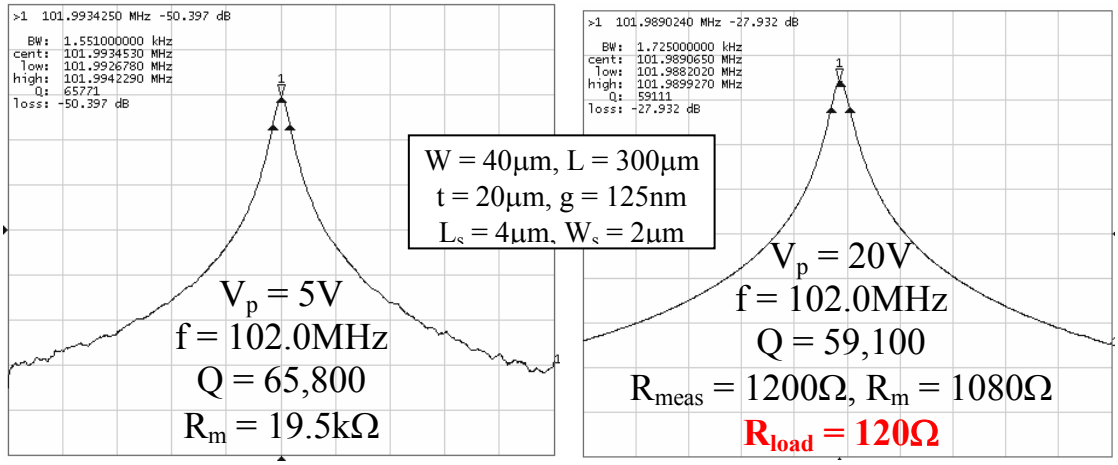

Figure 5.15. Frequency response of a SiBAR, fabricated on an ultra-low resistivity substrate showing a much smaller loading resistance of 120Ω.

With the demonstrated resonator transduction gap sizes in the 100-200nm range, comparatively large polarization voltages are required to achieve impedance values in the sub-kiloOhm range. By reduction of capacitive gaps to 100nm and below, the required polarization voltages can be significantly reduced. As an example, the plots in Fig. 5.16 show some of the resonance peaks measured for a 30um thick resonator with 65nm capacitive gaps. This is a successful demonstration of an ultra-high gap aspect ratio of ~460 fabricated through the advanced HARPSS-On-SOI process as described in Chapter II. The resonator is 50um wide and 540um long and its detailed SEM view is shown in Fig.2.22. As shown in Fig. 5.16 the 65nm capacitive gaps enable low motional resistances in the kilo-Ohm range with polarization voltages less than 10V. Such low polarization voltages can be generated and controlled on a CMOS chip.

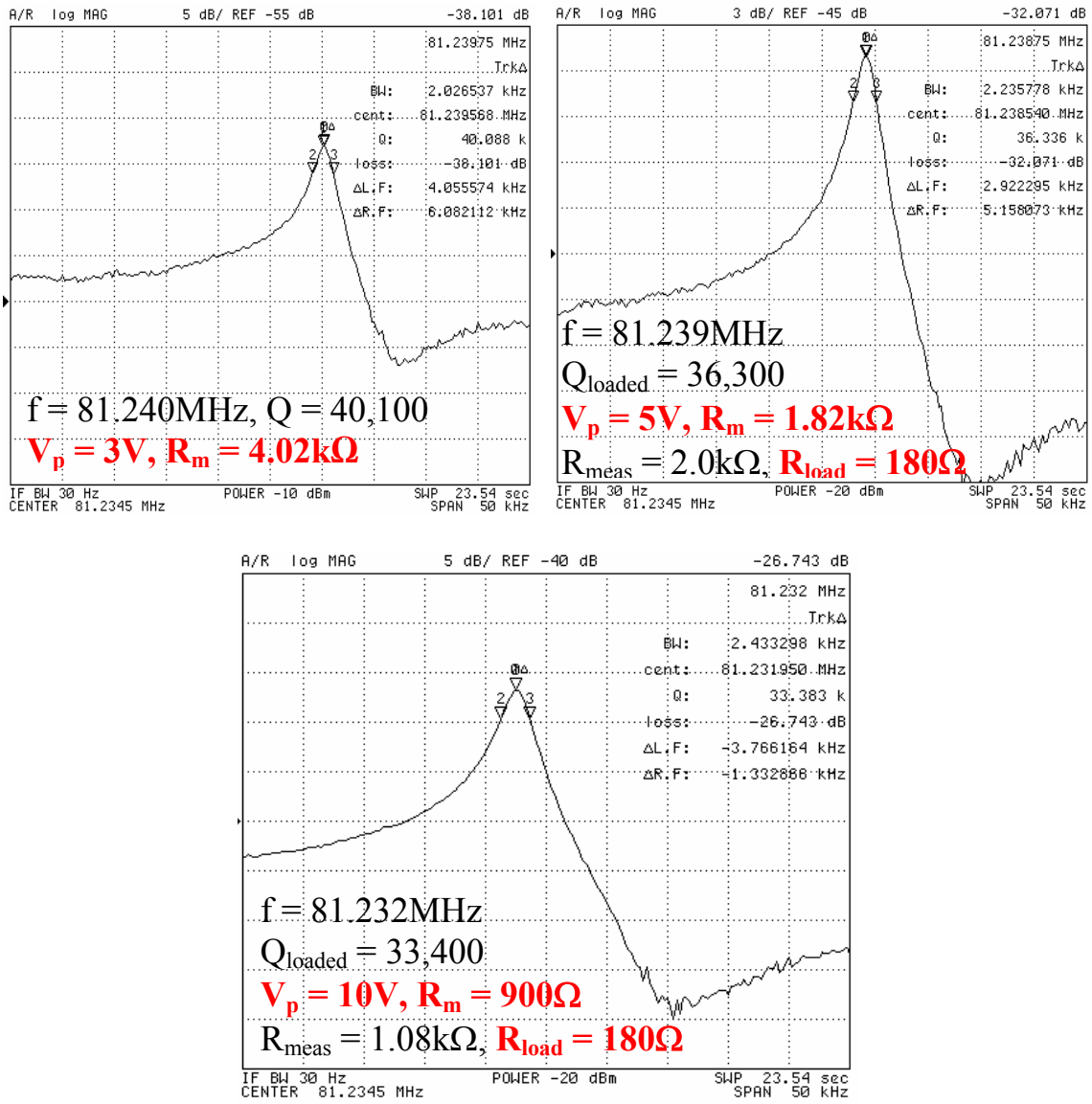

Figure 5.16. Measured frequency response for a 30um thick, 50um wide, 540um long SiBAR with 65nm gaps.

Table 5.1 summarizes the measured quality factors for SiBARs of different dimensions. It can be concluded from the data presented in Table 5.1 that increasing the length and thickness of the resonators with equal frequencies and support sizes, does not degrade their quality factor. This confirms the potential for reduction of the SiBAR equivalent impedances to any required level by further increasing the resonator length without sacrificing the quality factor or resonance frequency.

Measurement results in Table 5.1 clearly shows that resonators with quarter wavelength supports do not have noticeably larger quality factors compared to the SiBARs with short (3-5μm long) supports. On the other hand, much lower impedances can be achieved for the resonators with short supports. Short supports increase the stiffness of the resonator structure significantly making it much more resilient against electrostatic pull-in. Therefore, such resonators can tolerate much higher polarization voltages and provide lower impedances. Having stiffer structures is also beneficial from the manufacturability and reliability point of view for improving shock resistance of the resonators.

Table 5.1. Measured operating frequency, quality factor, and impedances for the fundamental mode of SiBARs with different dimensions.

Thickness (μm)	Width (μm)	Length (μm)	Support Width (μm)	Support Length (μm)	Gap size (nm)	Freq. 1st Mode	Q (Vac) 1st mode	Q (Air) 1st mode	V_p (V)	Q_{loaded}	R_{tot} (kΩ)	R_{load} (kΩ)	$R_{m,ext}$ (kΩ)	$R_{calc,PM}$ (kΩ)	Coupling Ratio (γ)
t = 30	50	540	3.0	6	65	81.2	40,100	-	5	36,300	2.0	0.18	1.82	0.43	0.24
	30	300	3.0	15*	210	138.9	21,700	-	45	21,700	62	-	62	1.9	0.031
t = 20	50	540	2.5	4.5	170	85.9	89,300	30,500	15	74,200	3.0	0.5	2.5	1.50	0.60
	50	300	2.5	4.5	170	85.9	77,300	24,400	60	22,500	0.68	0.48	0.20	0.39	0.98
	40	300	3.0	6	125	102.0	65,800	-	20	59,100	1.20	0.12	1.08	0.61	0.56
	40	300	2.5	4.5	170	106.7	60,800	-	40	26,400	1.53	0.87	0.66	0.56	0.85
	40	300	2.5	20*	170	106.6	75,100	-	15	64,900	7.5	1.0	6.5	3.2	0.49
	40	150	2.5	4.5	170	106.8	49,600	-	90	13,200	1.06	0.78	0.28	0.28	0.99
	40	150	2.5	20*	170	106.7	75,600	-	15	66,000	7.5	1.0	6.5	6.41	0.99
	30	300	2.5	4.5	170	139.7	31,500	-	35	26,600	2.9	0.5	2.4	1.42	0.60
	30	300	3	15*	160	137.2	41,500	-	25	39,800	5.5	0.2	5.3	1.7	0.32
	20	150	2.5	4.5	170	209.9	18,000	-	60	18,000	77.4	-	77.4	1.69	0.022
t = 10	50	300	2.5	4.5	135	86.2	34,000	-	20	31,200	6.2	0.6	5.6	3.2	0.57
	30	150	3	15*	225	142.9	47,000	24,600	62	43,300	6.2	0.5	5.7	3.7	0.65
	20	150	3	10*	225	214.2	35,700	21,800	60	34,000	10.2	0.5	9.7	5.2	0.53
	20	80	3	10*	225	213.4	30,200	20,200	100	28,700	6.3	0.3	6.0	4.2	0.7
	20	40	3	10*	225	214.8	31,400	17,000	90	30,000	17.7	1.1	17	9.9	0.58
	15	300	3	7.5*	225	281.5	24,300	-	15	24,300	107	-	107	61.2	0.57
	15	150	3	7.5*	225	280.7	7,200	-	70	7,200	33.8	-	33.8	19	0.56
	10	80	3	5*	225	431	6,000	-	100	6,000	440	-	440	21	0.05
t = 5	30	150	2.5	4.5	135	144.1	38,700	15,300	50	32,500	4.3	0.7	3.6	1.8	0.5
	20	100	2.5	4.5	135	217.5	28,600	15,100	50	26,300	9.9	0.8	9.1	3.6	0.4
	10	50	2.5	4.5	135	429.6	5,500	-	50	5,500	97	-	97	38	0.39
	7.5	80	2.5	4.5	135	591.5	4,600	-	25	4,600	416	-	416	113	0.27

* Quarter acoustic wavelength support lengths

$R_{m,ext} = R_{tot} - R_{load}$ = Extracted motional resistance value

$R_{calc,PM}$ = Calculated motional resistance using, assuming a non-distorted mode shape

5.2.3. Ultra-Long SiBAR Structures

It was shown that SiBARs can be stretched along their length without degradation of their resonance frequency or quality factor. Therefore, potentially any desired impedance value can be achieved for a SiBAR by choosing the right length for it. In practice however, increasing the resonator length will be associated with issues such as excessive compliance of the structure, which in turn results in stiction issues for the resonator during HF release or early pull-in at low polarization voltages. The other concern that still needs to be addressed is that increasing the resonator length after some point might result in intolerable mismatch between different parts of the resonator that can jeopardize its operation.

The simplest solution to the compliance problem is adding perpendicular support beams at several locations along the resonator length [47] as shown in Fig. 5.17. The support length should be equal to quarter wavelength at the operating frequency (half of the resonator width) in order to minimize the support loss. As reported in [20] adding notches to the resonators at support locations (Fig. 5.17b) can further reduce the support loss. However effect of adding extra supports to the ultra-long SiBAR structures on their quality factor needs to be investigated.

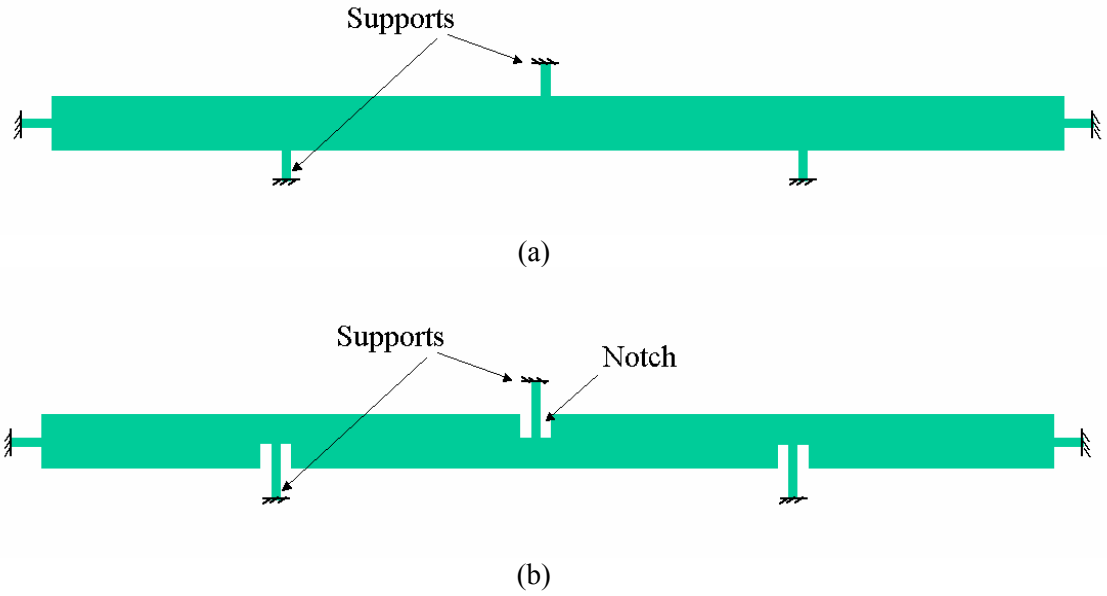

Figure 5.17. Schematic top view of ultra-long SiBARs with perpendicular supports along their length: (a) with un-notched supports, (b) notched supports.

For oscillator applications the resonator Q is desired to be as high as possible to minimize the close to carrier phase noise. However in most of the filter applications, a comparatively small (<1000) filter Q is targeted and very high resonator Q can help slightly reduce filter insertion loss, but is not a necessity; instead very low resonator motional resistances are required to avoid the need for large terminating resistors and resulting problems caused by parasitic input and output resonator capacitances. In other words, for filter applications, although having high resonator quality factors is a plus, it is preerred that low resonator impedances be resulting from strong electromechanical coupling (small gaps, large V_p, and large effective length) not its high quality factor.

Figure 5.18 shows the SEM view of a fabricated 1800μm long SiBAR with perpendicular support beams at several locations along its length.

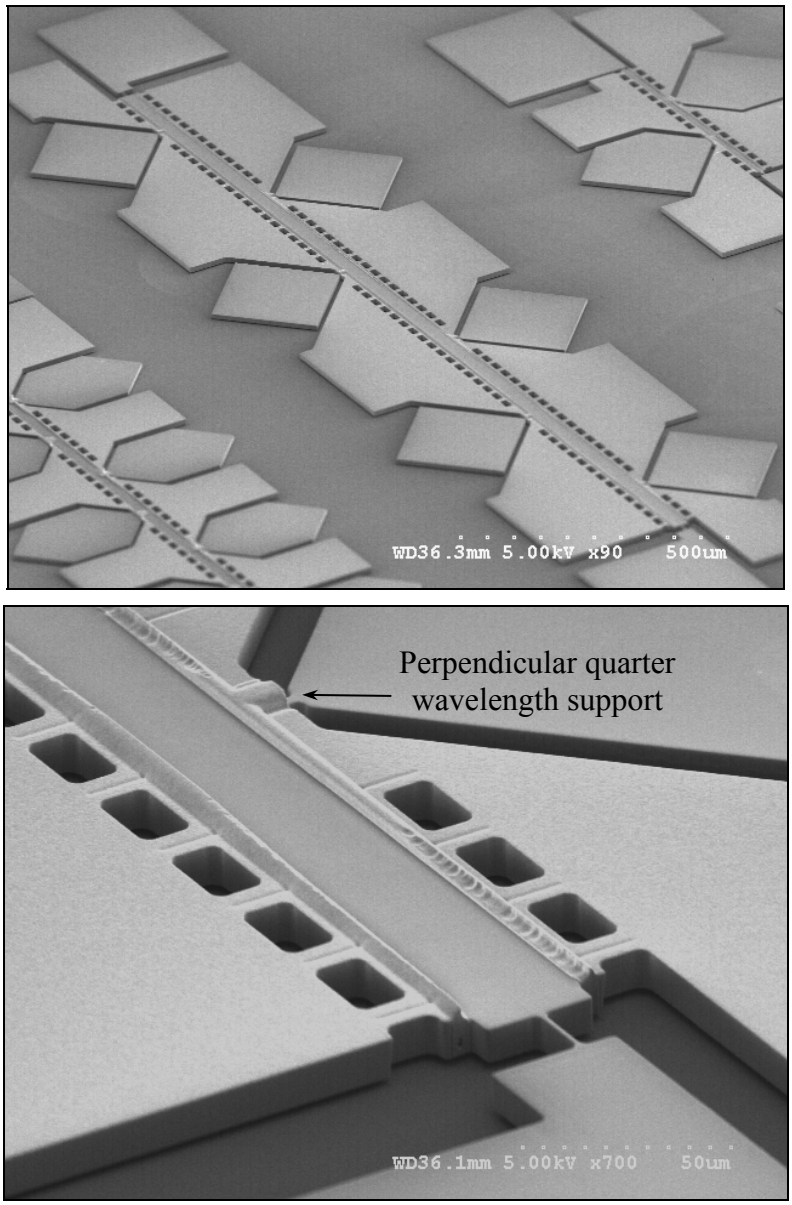

Figure 5.18. SEM view of an ultra-long (30μm wide, 1800μm long) SiBAR with perpendicular supports along its length.

As expected, the added supports reduce the resonator quality factor significantly (Figure 5.19a). Adding notches to the resonating body at the support interconnects helps increase its quality factor to some extent [20] (Figure 5.19b). However the Q is still much lower than the regular clamped-clamped SiBARs with similar resonance frequencies. Such large structures are very susceptible to having unwanted spurious

modes close to their main mode (Figure 5.19). Therefore, precautions need to be taken in their design to avoid and suppress the undesired modes as much as possible.

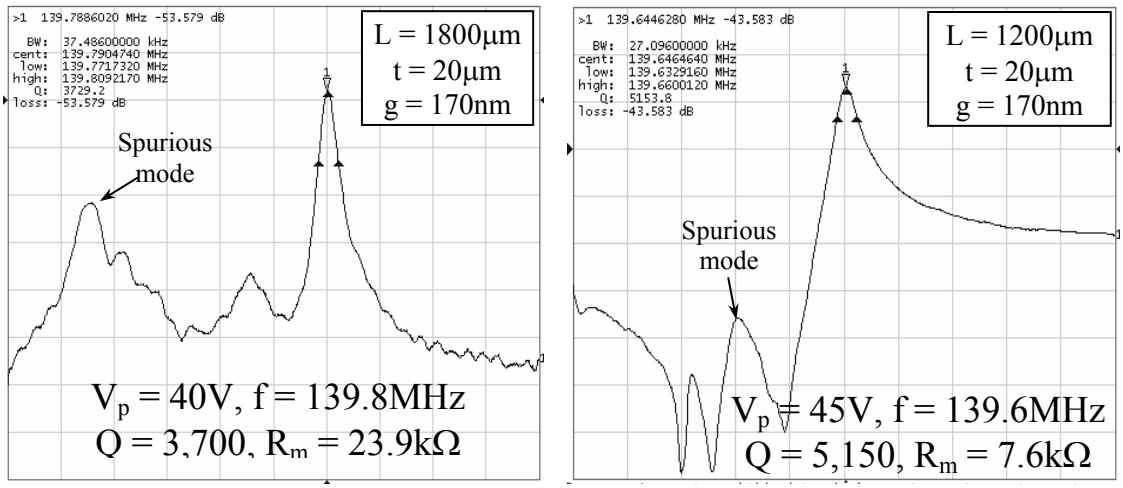

Figure 5.19. Measured frequency response of ultra-long 20μm thick 30μm wide SiBARs with perpendicular support beams along their length, (a) solid (un-notched) BAR, (b) notched BAR.

Corner supported square resonator is an alternative approach explored in this work to achieve larger effective length for the SiBARs while maintaining their structural rigidity. Figure 5.20 shows the SEM view and frequency response of a single square SiBAR supported at its four corners. Polysilicon interconnects bridging over the resonator provide electrical connection between different sections of the electrodes for the square SiBARs. Similar to the ultra-long SiBARs with perpendicular supports, proper design of the square SiBARs is not as straight forward as the regular clamped-clamped SiBAR. As an example it was noticed that when the square length is a multiple of its width, instead of having a single resonance peak for the resonator, the frequency response will have several resonance peaks with frequencies close to the expected frequency (Fig. 5.21). In addition the individual resonance peaks in the measured frequency response have higher

quality factors compared to the single peaks observed for other square SiBARs. This behavior can be explained by weaker coupling between the four sides of the square when its length is a multiple of its width. This results in more independent resonance of each side and separate resonance peaks for each of them. Less interaction between different sides of the square also results in less motion at the corner support locations and consequently higher Q.

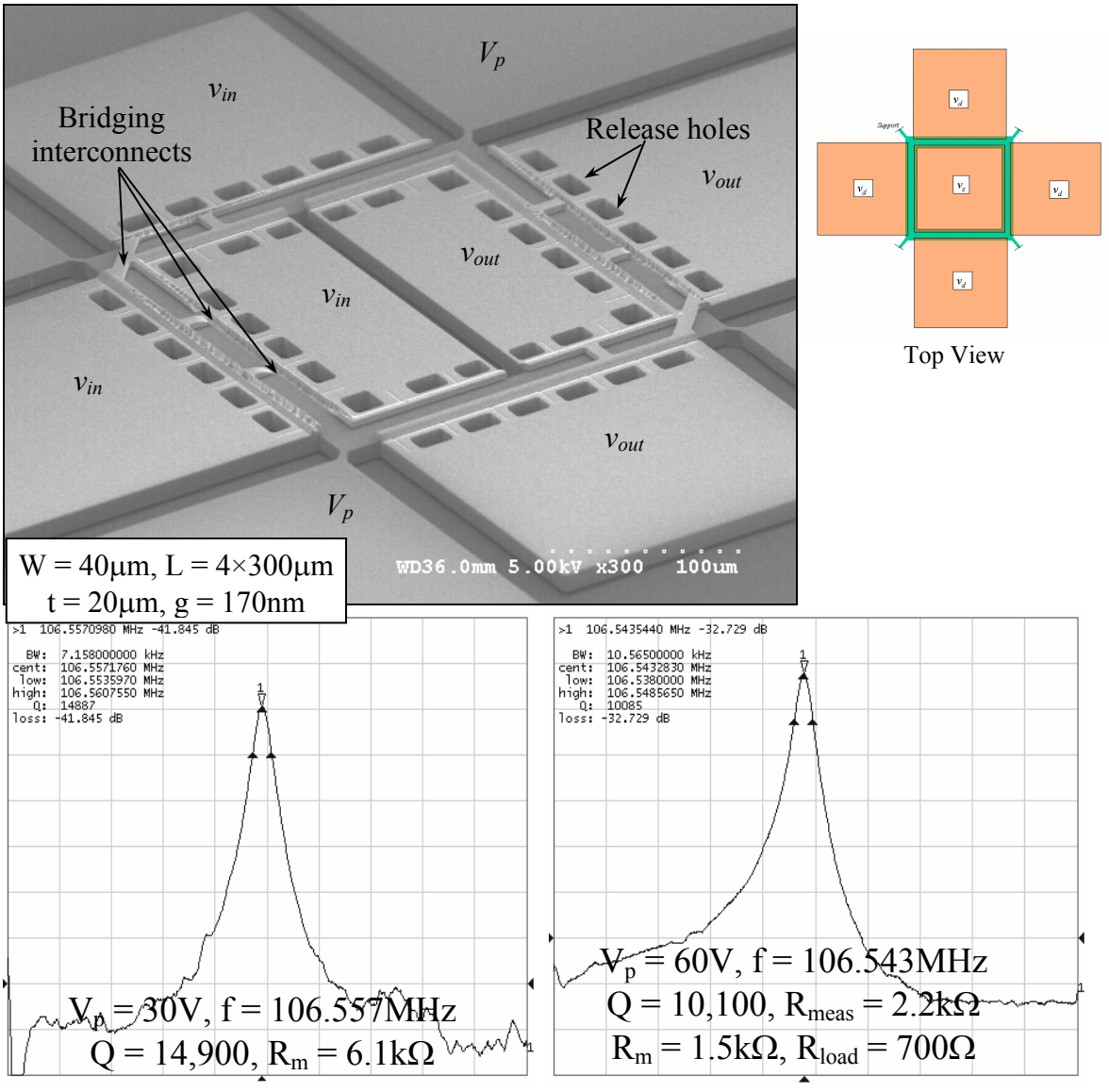

Figure 5.20. SEM view of a 20µm thick 40µm wide corner-supported square silicon BAR and its measured frequency response under low and high polarization voltages.

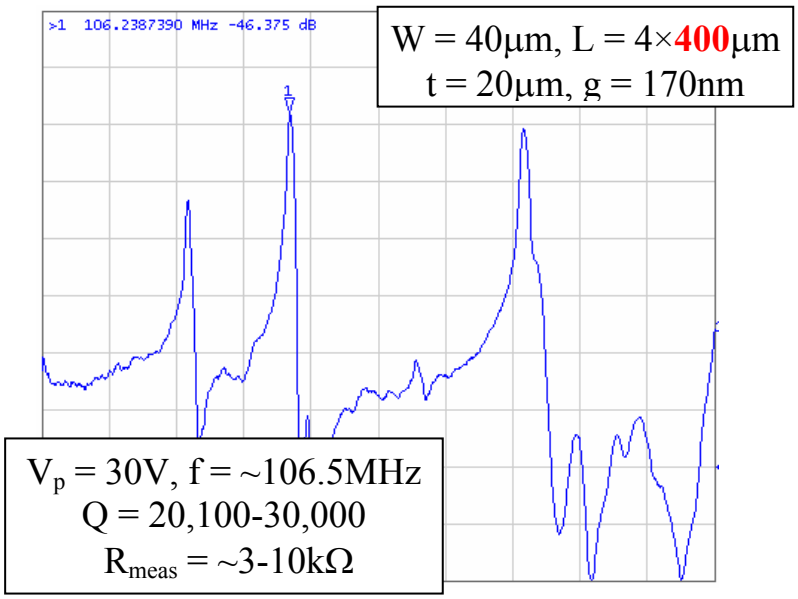

Figure 5.21. Measured frequency response of a square SiBAR showing several resonance peaks at close vicinity of the expected resonance frequency resulting from the square length being a multiple of its width..

In the square resonator of Fig. 5.22 the length maximization is taken another step further. This resonator consists of a network of four squares sharing common sides with each other. Square SiBARs have larger quality factors compared to the linear ultra-long SiBARs. However their quality factor is much lower than that of the regular clamped-clamped SiBARs.

The preliminary results for ultra-long SiBAR structures presented here, serve as a brief demonstration of different possibilities for extending the performance of regular SiBARs. Thorough understanding of resonant behavior of such complicated structures and development of design rules for their optimized design requires extensive finite element analysis and measurement, which is out of the scope of this thesis.

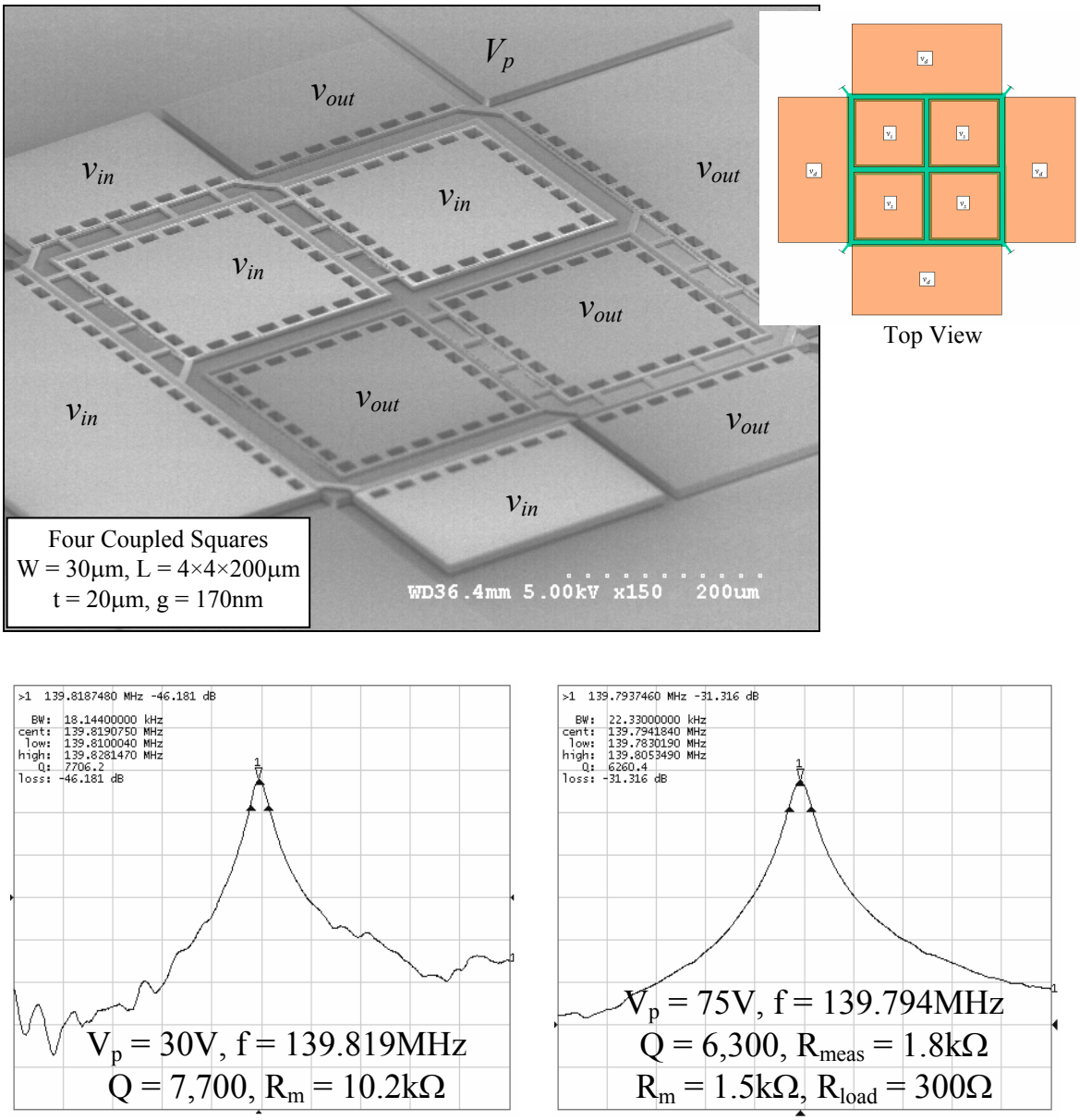

Figure 5.22. SEM view of a 4-square network silicon BAR and its measured frequency response with different polarization voltages.

5.3. Higher Mode Operation of SiBARs: Towards Low Impedance GHz Resonators

Although impressive performance has been achieved for VHF SiBARs, operation of such resonators in the UHF range as RF components is still facing challenges related to the large motional impedances.

For frequencies in the UHF range (300MHz-3GHz) the resonator width which is equal to half of the acoustic wavelength will be 13-1.3μm. As shown in Fig. 5.5, as the SiBAR thickness increases and reaches its width, the mode shape becomes distorted and the electrostatic coupling decreases drastically. An example is shown in Fig. 5.23 in which the frequency response of a 30μm wide, 30μm thick and 300μm long SiBAR exhibits over 20X larger impedance that the expected impedance for a non-distorted mode shape. This is blamed on severely distorted mode shape due to improper choice of dimensions for the resonator. Another example is shown in Fig. 5.24 that compares two different SiBARs with similar resonance frequencies (equal width) but different thickness. Surprisingly, the thicker resonator has about four times larger motional resistance compared to the thinner resonator. The effect of other parameters such as length, V_p, Q and gap size for the two resonators is almost equal and the higher impedance of the thicker resonator can only be a result of distorted mode shape and much smaller coupling ratio (γ). In conclusion, reducing the resonator impedances in the UHF range is not as straight forward as increasing their thickness and larger thickness may have an opposite effect if proper device dimensions are not selected. Identification of the

optimized BAR dimensions requires extensive finite element analysis which is out of the scope of this thesis.

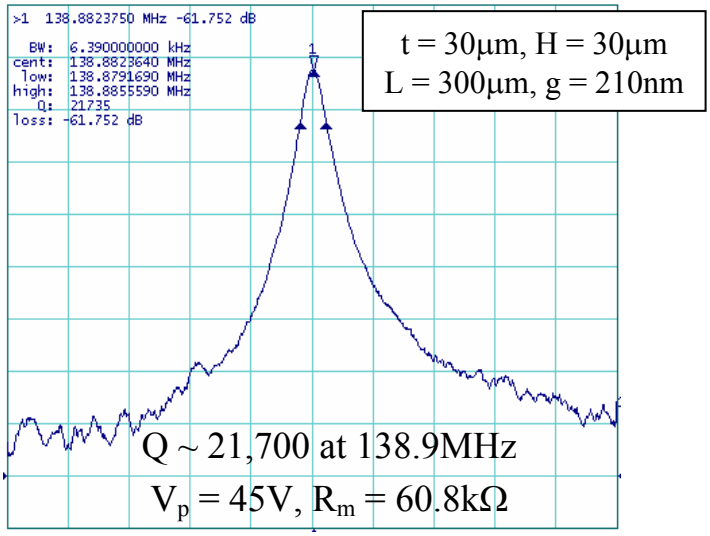

Figure 5.23 Measured frequency response of a 30µm wide, 30µm thick, 300µm long clamped-clamped SiBAR showing about 20 times larger impedance than the expected value assuming an undistorted mode shape.

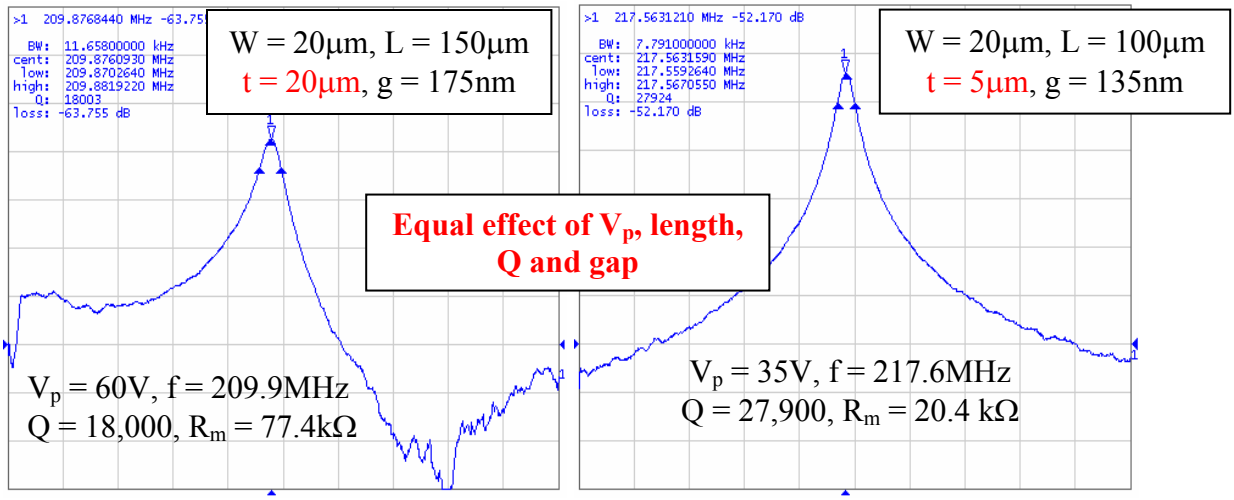

Figure. 5.24. Comparison between 5um thick and 20um thick, 20um wide SiBARs showing a much lower impedance for the thin resonator. The impedance of the thicker resonator is about 15 times higher impedance than expected for the same device with undistorted mode shape.

The more straight forward solution which is not as effective is to keep the resonator thickness 10μm or less (depending on how high the target frequency is) to ensure that the mode shape is not severely distorted. Fabrication of such thin resonators using the HARPSS technology is not desirable since several surface micromachining fabrication approaches are available for implementation of thin resonators [19-22]. In addition, thin structures are much more susceptible to stiction due to the compliance of their structure in the vertical direction and therefore reliable fabrication of thin HARPSS resonators is more challenging compared to their thicker counterparts.

5.3.1. Higher Resonance Modes of Thin SiBARs

The support beams for the SiBARs in this work are placed in the middle of the resonator width. Therefore, in the even width extensional modes the supports will be subject to large vibration amplitude imposed by the resonator and introduce excessive loss resulting in low quality factors. However for higher order odd width extensional modes, similar to the first mode, the midpoint of the device width is still the resonance node (i.e. has close to zero vibration amplitude) and high quality factors can be obtained.

Theoretically, the motional resistance for the n^{th} width extensional mode of a SiBAR assuming an undistorted mode shape is n times larger than that of a the same device operating in its first mode. This can be explained using Equation 5.2, where the electrode dimensions are the same, but the effective stiffness is n^2 times larger for the higher resonance mode resulting in n times larger impedance.

Figure 5.25 shows the measured frequency response of a 30µm wide, 150µm long, 5µm thick SiBAR operating in its first and higher odd width extensional modes up to the 5th mode. Quality factor of 17,300 at resonance frequency of 765MHz has been measured for the 5th mode of this resonator. Impedance as low as 23.7kΩ was measured for this resonance mode, which is close to one order of magnitude lower than the typical reported motional resistance values for capacitive resonators at such high resonance frequencies.

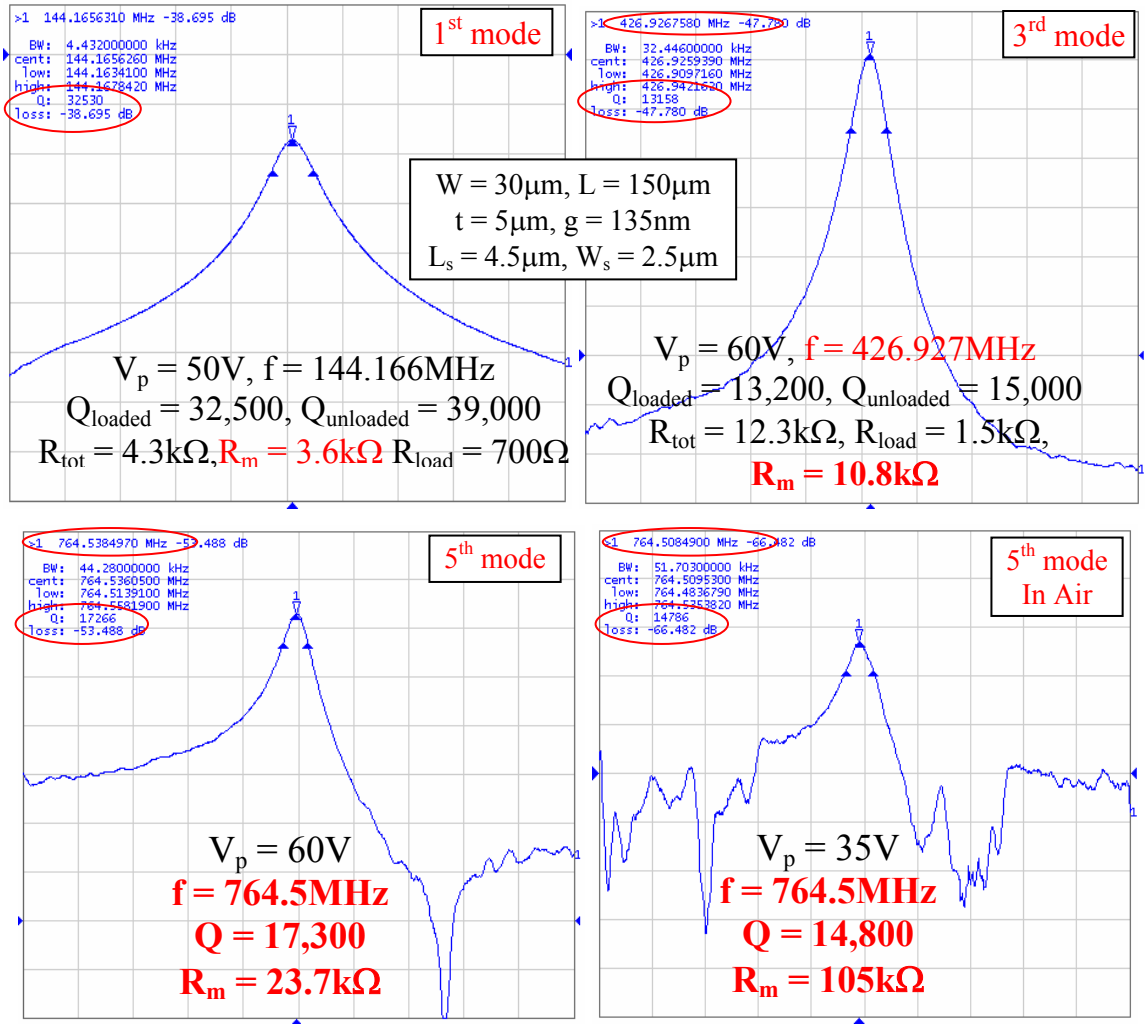

Figure 5.25. Measured frequency response of a 30µm wide, 150µm long, 5µm thick SiBAR operating in its first and higher resonance modes up to the fifth mode.

Figure 5.26 shows the SEM view as well as ANSYS modal analysis results for the same SiBAR structure showing the mode shape for the first, third and fifth width extensional modes.

Similar argument about the effect of resonator thickness on its mode shape applies to the higher modes of SiBARs. Clean and uniform mode shapes with large coupling ratio can be obtained for resonator thickness smaller than its effective width. For higher modes, the effective width is *n* times smaller than the physical width of the resonator, where *n* is the mode number.

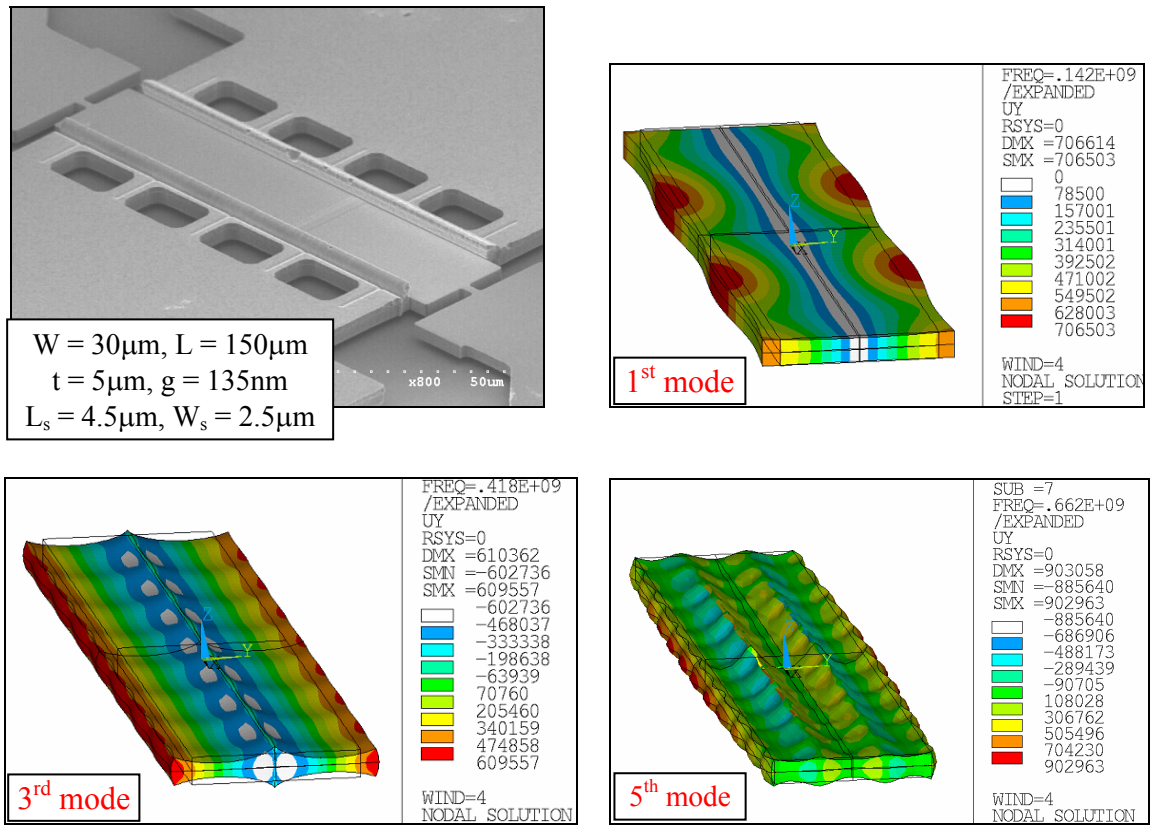

Figure 5.26. ANSYS modal analysis showing the mode shape for the first, third and fifth width extensional modes of the SiBAR of Figure 5.25.

Figure 5.27 shows the measured frequency response for a 50μm wide, 10μm thick resonator and it higher resonance modes. For the third resonance mode of this device, the effective width is 50/3 ~ 17 and therefore the mode shape will be clean and a resonance peak with a frequency of three times the first mode can be detected (3×86 ~ 251). The next high-Q and low impedance resonance mode for this resonator was observed at 359MHz with an impressive Q of 40,200 demonstrated f.Q product of 1.44×10^{13} (10^{13} is considered to be the physical limit for quartz crystals). The frequency of this mode is not close enough to five times the first mode, and therefore can not be considered the fifth mode. However, the effective length at the measured frequency is ~12μm which is very close to the resonator thickness and therefore, it is not surprising that the frequency does not match the expected value for a clean mode shape. Further discussion on higher resonance modes with resonator thickness higher than the effective length will be provided in the next section.

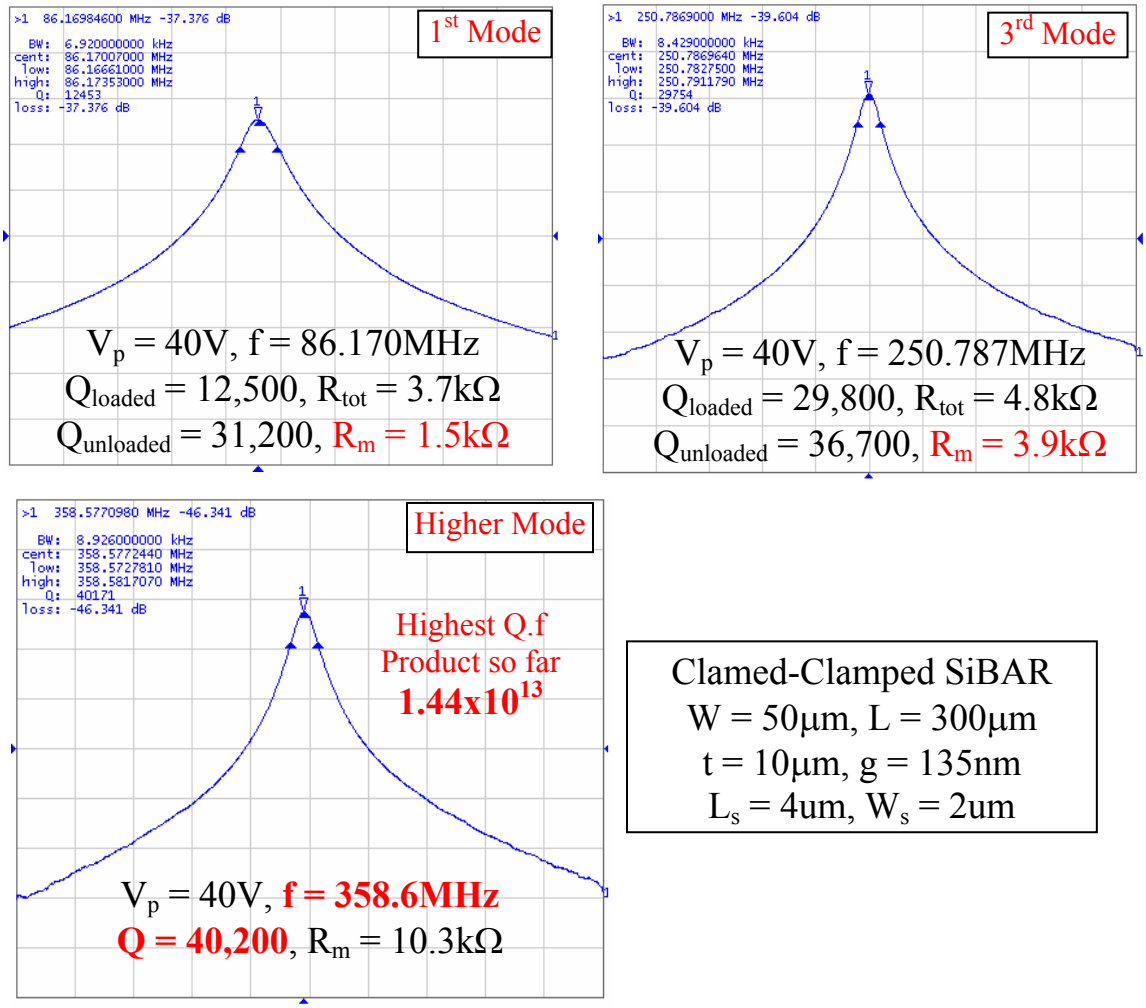

Figure 5.27. Measured frequency response for the first and higher resonance modes of a 50µm wide, 10µm thick SiBAR, showing how the frequency deviates from the expected value for higher harmonics as the effective length reaches resonator thickness.

5.3.2. Higher Resonance Modes of Thick SiBARs

Figure 5.28 shows some of the frequency responses in the UHF range measured for the third thickness modes of SiBARs with different dimensions. The measured quality factors are 3,100 and 3,700 at resonant frequencies of 502MHz and 983MHz corresponding to 30μm and 15μm wide resonators respectively. The affective width for the third extensional mode of these devices are 10μm and 5μm respectively which is equal or smaller than the thickness of the resonators. Therefore, based on the discussions in the previous sections, severely distorted mode shapes and extremely large motional impedances for such devices are not surprising.

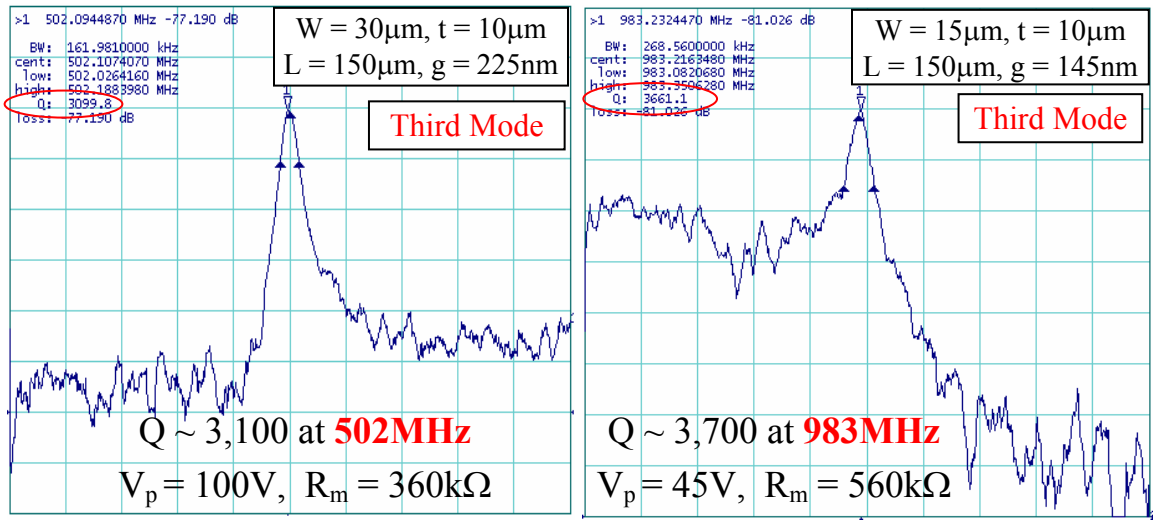

Figure 5.28. Frequency response of 10μm thick SiBARs operating in their higher resonance modes showing very large equivalent impedances due to mode shape distortion.

Prediction of the resonance frequency for such higher resonance modes and finding the appropriate dimensions to maximize their coupling ratio requires extensive and complicated micromechanical analysis. Finite element analysis to find such wavy mode

shapes requires a large number of elements and results in a very large number of modes which makes running the simulation and recognition of the right mode quite complicated and out of the scope of this work. However, some of such higher resonance modes, happen to have surprisingly low motional resistances and can be identified experimentally. Figures 5.29 and 5.30 shows a number of measured resonance peaks in the 1GHz frequency range for higher modes of lower frequency SiBARs with comparatively low motional resistances.

Figure 5.29 shows the measured frequency response of a 40μm wide, 20μm thick SiBAR operating in its fundamental extensional mode at 102MHz as well as a number of higher frequency modes. Resonance modes with frequencies as high as 1.13GHz have been measured for this resonator with comparatively low impedances. The 1.13GHz mode has an impedance of 35kΩ which is close to an order of magnitude lower than other reported capacitive resonators in the GHz range [20-22]. Frequency-wise this resonance peak should correspond to the 11^{th} width extensional mode of the structure, however, referring to such resonance modes as higher width extensional mode does not seem to be appropriate. Although using the higher modes is a good approach to implement high performance GHz silicon resonators, existence of lower frequency resonance modes (specially the fundamental mode with much lower impedance) in the overall frequency response of such devices can be a serious problem (e.g. oscillator locking to the wrong mode). Figure 5.30 shows the high frequency resonance mode measured for a 20μm wide, 20μm thick SiBAR. As shown in Fig. 5.23, for such resonator dimensions, the coupling ratio for the fundamental mode is very low resulting in a high impedance. This helps reduce the possibility of locking to the wrong mode,

when targeting a 1.55GHz frequency reference. Therefore by proper choice of BAR dimensions, the desired high frequency mode can be improved while the undesired lower frequency modes are suppressed.

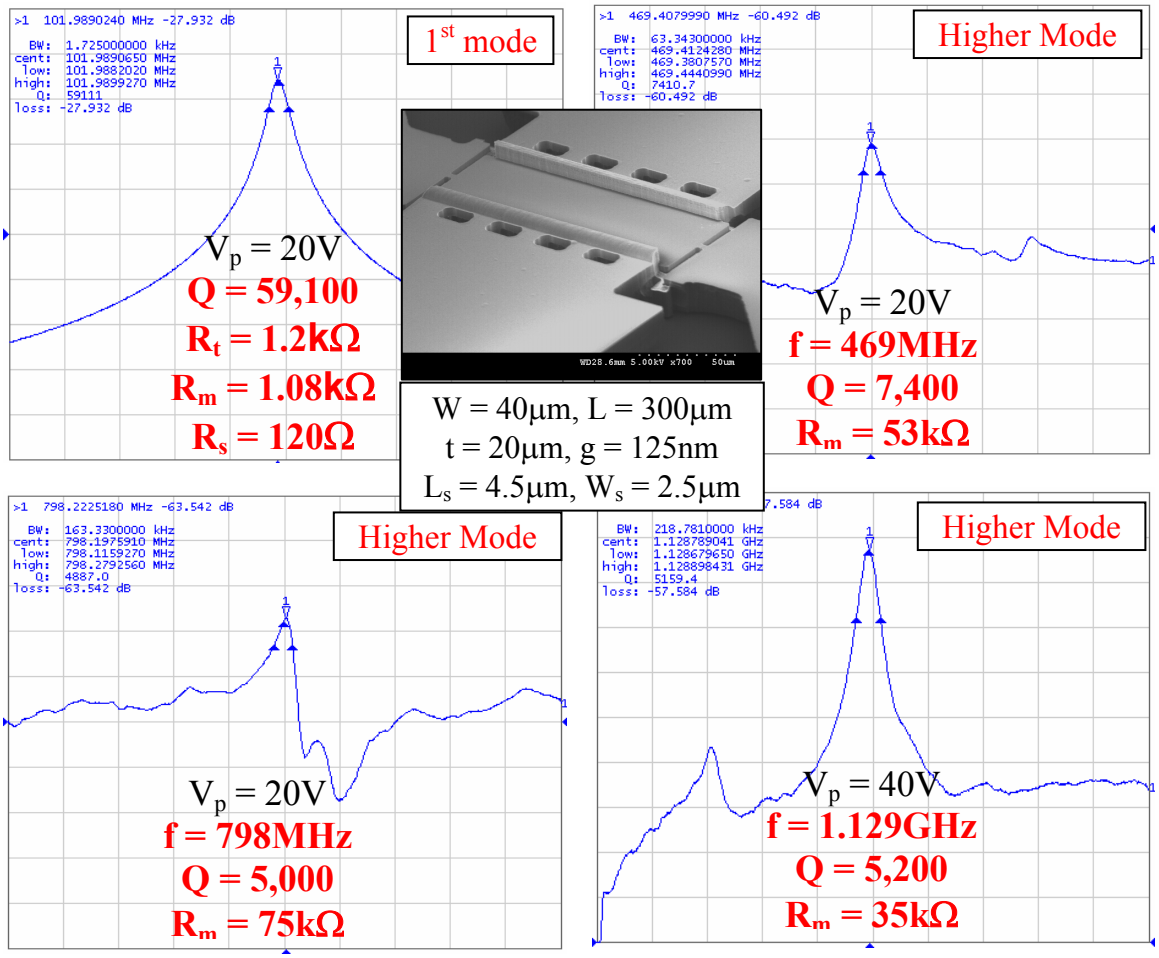

Figure 5.29. Measured fundamental and higher resonance modes measured for a 40µm wide , 20µm thick, 300µm long SiBAR fabricated through the improved HARPSS-On-SOI process.

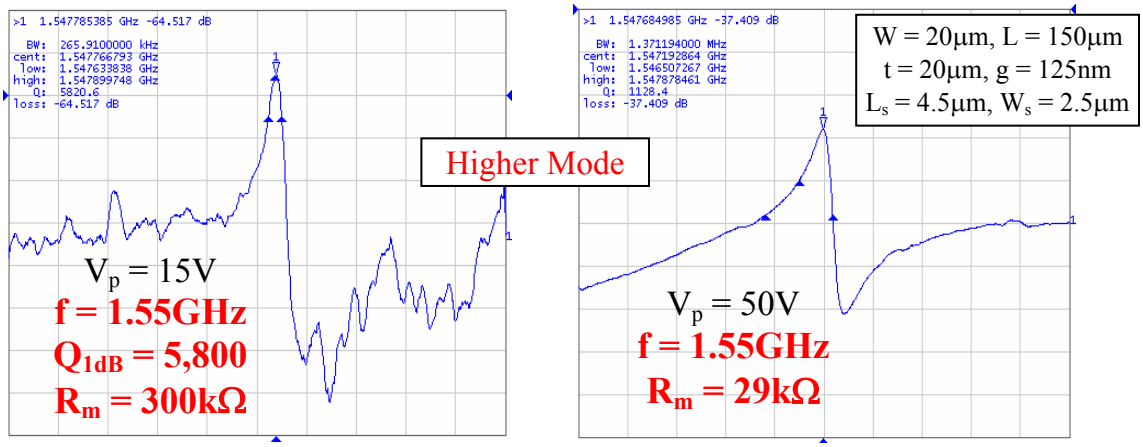

Figure 5.30. Higher resonance mode measured for a 20µm wide, 20µm thick, 150µm long SiBAR with 125nm capacitive gaps. The fundamental mode for this resonator is suppressed significantly due to mode shape distortion.

5.4. Temperature Characteristics and Temperature Compensation of High Frequency SCS Resonators

HARPSS capacitive SiBARs implemented in this work have shown great potential as frequency references in the HF, VHF, and low UHF range. The major remaining bottleneck that limits performance of capacitive SiBARs for some of the applications compared to the traditional quartz crystals is their higher temperature coefficient of frequency. Figure 5.31 shows the SEM view as well as the measured resonance peaks for a 50μm wide, 540μm long, and 20μm thick SiBAR. The resonator operates in its first width extensional mode at 86MHz with a Q of 89,000 in vacuum and 30,500 in air. Temperature dependency of this resonator was measured over a temperature range of -40 to 120°C in atmosphere using a regular temperature controlled oven. Figure 5.32 shows the measured temperature drift of frequency for this resonator. The temperature drift has a linear trend with a temperature coefficient of frequency (TCF) of -27.8ppm/°C. Such temperature drift slope is very close to the values previously reported for SCS disk resonators [26] and piezoelectric FBARs [51]. As shown in [26], the temperature drift of silicon resonators is mainly due to the large temperature coefficient of Young's modulus of silicon.

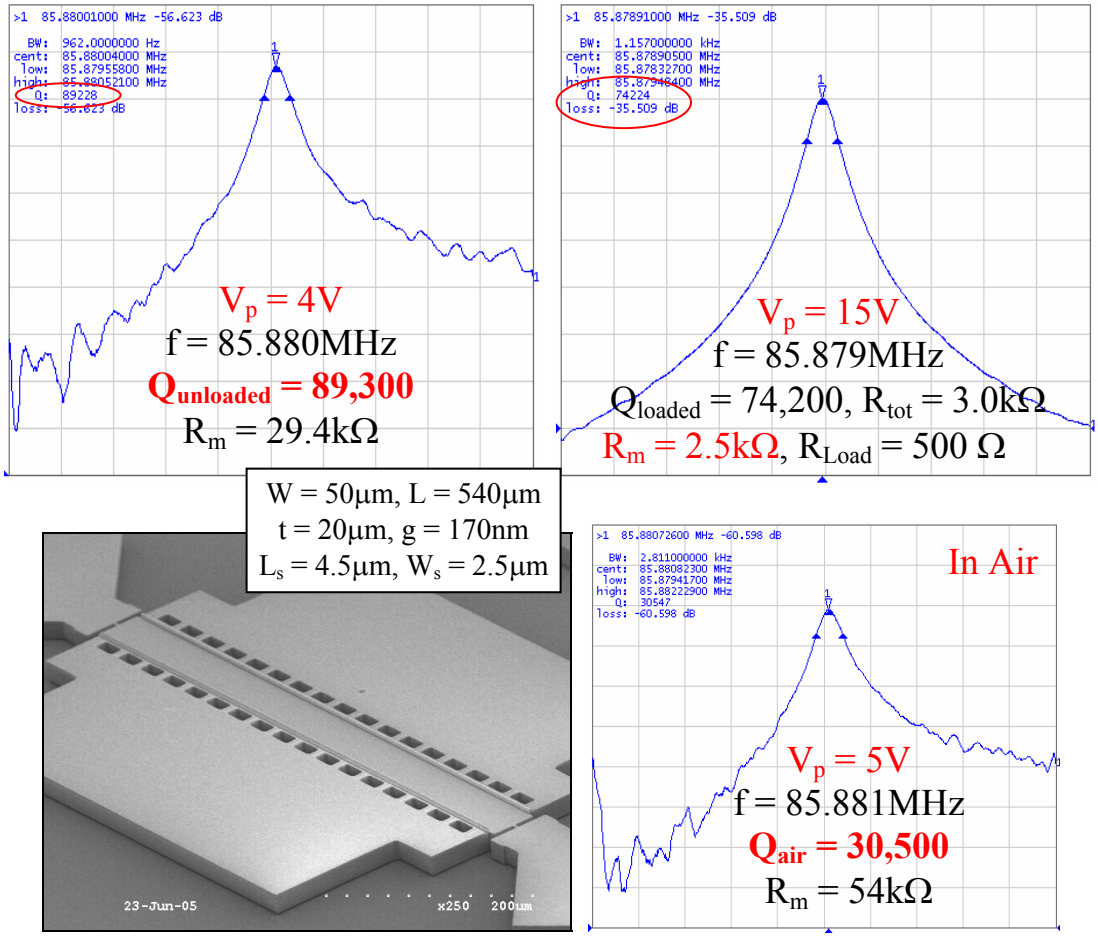

Figure 5.31. Frequency response of a 540µm long, 50µm wide, 20µm thick SiBAR showing low impedance values by applying reasonably low polarization voltages.

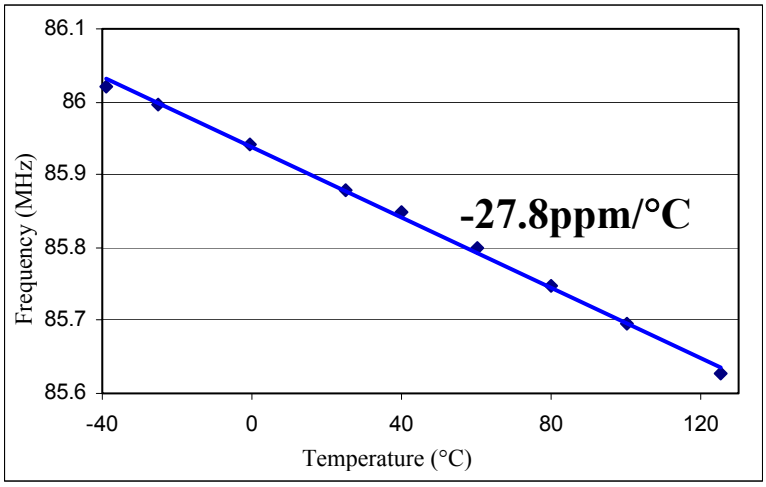

Figure 5.32. Temperature dependence of frequency of the 86MHz SiBAR of Figure 5.31 showing a TCF of -27.8ppm/°C.

Different frequency tuning techniques for temperature compensation of capacitive silicon resonators are available. Electrostatic tuning of parallel plate capacitive resonators by changing the resonator DC bias (polarization) voltage is the favorite choice for lower frequency resonators due to its low power consumption and simplicity. Temperature compensated oscillators using I-BAR resonators with temperature stability better than regular quartz crystals and close to TCXOs have been demonstrated under this project [40,41]. In this approach a temperature dependant DC bias is generated by a low power CMOS circuit and is applied to the resonator to cancel out its temperature induced drift by changing the bias voltage with temperature. For higher frequency resonators (e.g. SiBARs), however, the resonator stiffness is extremely large and the maximum electrostatic tuning range that can be achieved is not large enough to compensate the resonator over a wide temperature range.

Figure 5.33 shows the measured electrostatic tuning characteristic for a 108MHz SiBAR with 135nm capacitive gaps. A frequency tuning of 70kHz is demonstrated for this resonator by changing the polarization voltage from 10V to 70V. Tuning slope for a capacitive SiBAR assuming a non-distorted mode shape is given by Equation 5.4:

$$\frac{\partial f}{\partial V_p} = -\frac{2V_p f \varepsilon A_e}{Kg^3} \tag{5.4}$$

where f is the resonance frequency of the resonator, A_e is the electrode area (area of one electrode only) and K is the effective stiffness as used in Equation 1.

Tuning range of around 300kHz is required to compensate a 108MHz resonator over a 100°C temperature range. As an example, according to Equation 5.2, such tuning range can be achieved by reduction of the capacitive gap sizes to 70nm and changing the

polarization voltage over a range of 5V to 40V, which seems possible although very challenging. However, as the frequency goes to higher values, the required electrical stiffness for temperature compensation increases proportionally making electrostatic compensation more challenging. In addition, changing the polarization voltage of the resonator changes its equivalent electrical impedance sharply which is not desirable from the circuit design point of view. Solution to this problem would be to split the electrodes around the resonator to two electrically isolated sections, one for electrostatic transduction (sense and drive), and one for frequency tuning. In this case, smaller electrode area for each mechanism will result in higher resonator impedance and lower electrostatic tuning (4X higher impedance and 2X lower tuning in case of equally divided electrodes). As a result, even further pushing of the gap sizes to smaller values will be required to get the same performance.

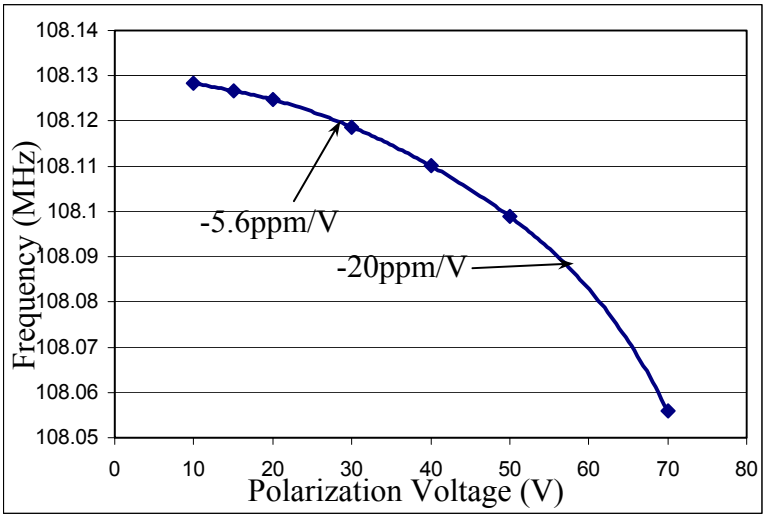

Figure 5.33. Measured electrostatic tuning characteristic of a 108MHz SiBAR showing a tuning range of over 70kHz.

The more effective but power consuming approach that can be quite effective for any resonator independent of its resonance frequency is controlling the resonator temperature and therefore tuning its resonance frequency by passing current through its structure. The actual temperature of the resonator structure can then be controlled by the amount of current applied to it. Since the SiBARs are supported by two support beams on the two sides, two polarization voltage bonding pads are available on the two ends of the resonator making it a perfect structure for current tuning. By applying slightly different DC voltages to the two pads on the two ends of the resonator, DC current will pass through the SiBAR structure and elevate its temperature.

Figure 5.34 shows the frequency tuning characteristics of the SiBAR of Figure 5.31 by passing current through it. More than 1MHz (1.2%) of frequency tuning has been achieved by passing up to 24mA of DC current through the body of the resonator. According to the measured temperature induced frequency drift (Fig.5.32), this corresponds to an elevated temperature of up to 450°C for the resonator (assuming that the resonator maintains its linear temperature characteristics over the whole temperature range). It is worth noting that the resonator was operating flawlessly with no degradation of the quality factor at such high temperature.

This tuning technique can be deployed for temperature compensation of high frequency SiBARs. A temperature dependant current source can be used to keep the temperature of the resonator elevated (e.g. at 125°C) independent of the temperature of the surrounding environment and avoid the temperature drift. In this case, the unpackaged resonator on a $1.2\times1.2cm^2$ silicon substrate with no thermal isolation from the test setup, 85mW of power was required at room temperature to keep the temperature

of the resonator elevated at 125°C. This can be reduced to a few mW or even below mW for a single resonator inside a thermally isolated package. This approach is similar to the concept of oven controlled crystal oscillators (OCXO) which are the most stable quartz crystal frequency references available. Thermal temperature control for the silicon resonators however can be done by consuming a much smaller amount of power due to their smaller size. In addition, due to the linearity of the temperature characteristics of the silicon resonators the control circuitry is expected to be much simpler.

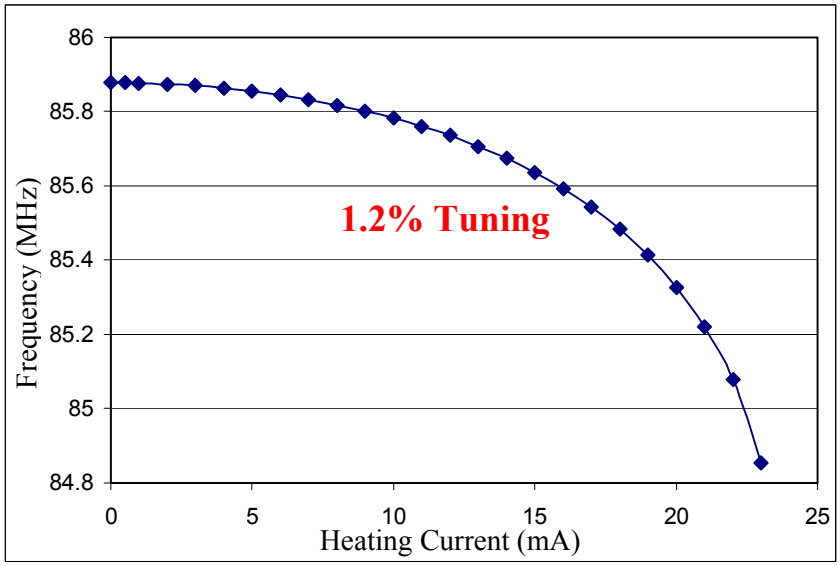

Figure 5.34. Heat induced tuning characteristic of the 86MHz SiBAR of Fig. 5.31 by passing current through the body of the resonator.

Furthermore, as shown in Figure 5.35, the resistance between the polarization voltage pads on the two sides of the resonator changes as a function of temperature. Therefore, one can take advantage of temperature dependency of the resistance of the silicon resonator and use it as a simultaneous in-situ temperature sensor. By corporation of such

resonator in a feedback loop and using it as a the heater, temperature sensor, and frequency reference simultaneously, very high stability levels can be achieved.

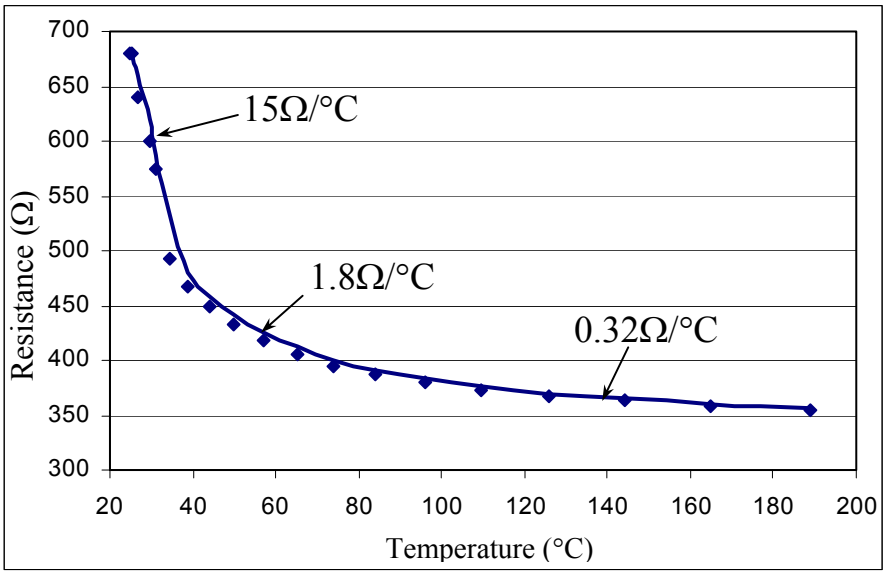

Figure 5.35. Measured resistance between the polarization pads on the two ends of the SiBAR of Figure 5.31 as a function of temperature. Temperature values are extracted from the frequency values in Figure 5.32 based on linear temperature drift of –27.8ppm/°C.

CHAPTER VI

HIGH FREQUENCY COUPLED RESONATORS AND FILTERS

One of the major applications of mechanical resonators in general is implementation of narrow band-width electronic filters. Mechanical filters are used in systems that demand narrow bandwidth, low loss and good stability [1]. Because of the high Q and excellent temperature and aging characteristics these requirements can be achieved with mechanical filters.

A single resonator by itself is a bandpass filter, however, a single resonators although having a high quality factor in the order of a few tens of thousands, is a first order bandpass filter providing limited frequency selectivity (shape factor) which is not enough for most of the applications. To achieve higher filter selectivity (closer response to an ideal filter) higher order bandpass filters consisting of a number of coupled resonators are required [1,34]. It was also discussed and demonstrated in [34] that several electrical or mechanical techniques can be employed to couple similar resonators to each other resulting in multiple coupled resonance modes with close frequencies. Having several coupled modes (several poles in the transfer function) with close natural frequencies provides sharper transition from passband to the stopband, making the filter characteristic closer to an ideal filter. High quality factor of mechanical resonators allows realization of mechanical filters with narrow bandwidth as small as 0.1% and smaller without introducing excessive loss or passband rounding.

Traditionally piezoelectric resonators have been widely used for implementation of higher order filters with sharp roll-off for a variety of wireless applications. Several

types of mechanical filters using different types of resonators, including metal alloy, PZT-ceramic [48], zinc oxide [49] resonators and SAW filters [9,10] have been developed and commercially available.

Recent advances in development of the micromechanical resonators, has led to new opportunities for miniaturization of the mechanical filters. Mechanical and electrical coupling techniques have been applied to different types of micromechanical resonators for demonstration of higher order coupled resonators and filters [42,51-63]. The following sections will discuss and demonstrate several coupling approaches used to implement high frequency multiple order resonant systems using the SiBAR structures. Possibility of developing high performance filters using such devices and some of the limitations will be discussed.

6.1. Mechanical Coupling of High Frequency SiBARs

Mechanical coupling of individual micromechanical resonators is the most common approach for implementation of higher order micromechanical filters. In this approach, the resonators are physically connected to each other by comparatively compliant mechanical elements resulting in multiple resonance modes for the whole system. The frequency difference between the resonance modes is determined by the ratio of the stiffness of individual resonators to the stiffness of the coupling elements. More compliant coupling elements result in smaller separation of the resonance modes. One of the challenges for mechanically coupled filters is comparatively strong coupling provided by the mechanical coupling elements resulting in wide bandwidth and low filter Q. This is mainly due to comparatively large stiffness of the mechanical coupling elements unless they have very small sizes. This can impose a limit on the minimum achievable bandwidth (maximum filter Q) for such filters. There has been somehow successful efforts to reduce the mechanical coupling strength and achieve higher filter Qs using low-velocity coupling [60] or through-support mechanical coupling [61].

For the SiBAR structures presented in this work, due to extremely large size of the resonators and consequently large resonator overall stiffness, mechanical coupling can be a more promising approach towards high-Q filters.

Several types of mechanical coupling were qualitatively under consideration for qualitative investigation of mechanical coupling of VHF SiBARs. Among which are coupling with a perpendicular or parallel coupling beam connecting the two BARs to each other as well as through support coupling. The width and length of the coupling

beam as well as its location determines the bandwidth for such coupled resonant systems. Figure 6.1 demonstrates schematic top view of such coupled resonator systems. The perpendicular coupling beam in Fig. 6.1a is expected to operate in its length extensional mode while the parallel coupling beam in Fig. 6.1.b is expected to operate in a flexural mode resulting in much smaller coupling strength and therefore narrower bandwidth. The structure in Fig. 6.1c is an example of a through-support coupled resonator system. For a support length of quarter wave-length (coupling element length of half wave-length) at the resonance frequency the weakest coupling and highest filter Q can be achieved.

It is also worth noting that extremely high filter Q (> 1000) is not necessary for most of the applications specially in the lower VHF range. In addition stronger coupling (lower filter Q) can help compensate for slight frequency mismatch (due to fabrication tolerance) between the coupled resonators, while for weakly coupled arrays, the frequency mismatch and mismatch compensation can be a very challenging issue.

Figure 6.2 shows the measured frequency response of two different second order coupled 106MHz SiBARs with parallel coupling beams. Separation of the resonance peaks are in the 500kHz range which when terminated as a filter, will result in filter Q of ~100. Strong mechanical coupling between such resonators can compensate fabrication induced frequency mismatch between the two resonators which is typically in the order of 1000ppm.

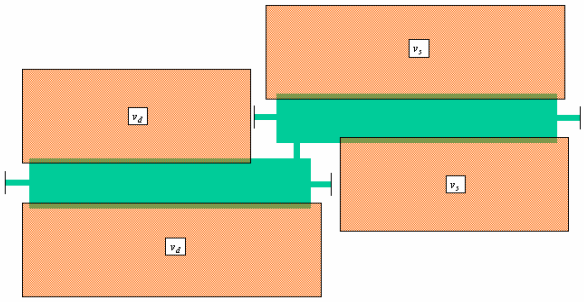

(a) With perpendicular coupling beam

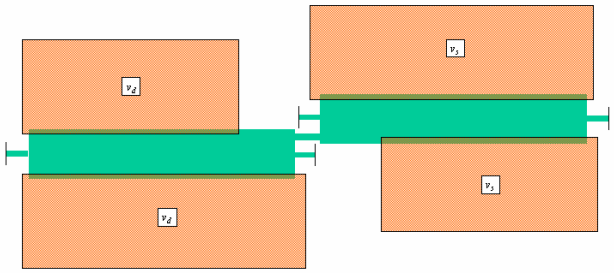

(b) With parallel coupling beam

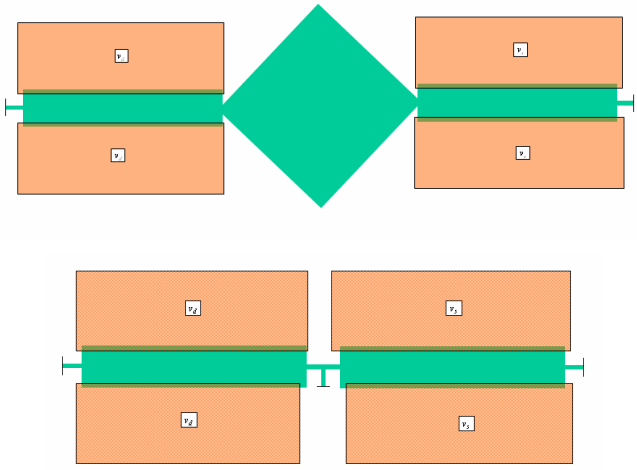

(c) Through support coupled

Figure 6.1. Schematic top view of several types of mechanically coupled SiBARs considered for qualitative evaluation of mechanical coupling approach.

The minimum measured impedance for such coupled resonant arrays in their passband is in the order of a few tens of kilo-Ohm. Therefore, the terminating resistances

required to damp the filter response and reduce the passband ripple to acceptable values is in the order of hundreds of kilo-Ohm. To have effective resistive damping the parallel capacitances existing at the filter terminals should have a much larger impedance compared to resistive terminations. It this case it means capacitance values in the order of 10fF which is much smaller than the pad capacitance and electrode capacitance physically existing at the input and output ports of the device

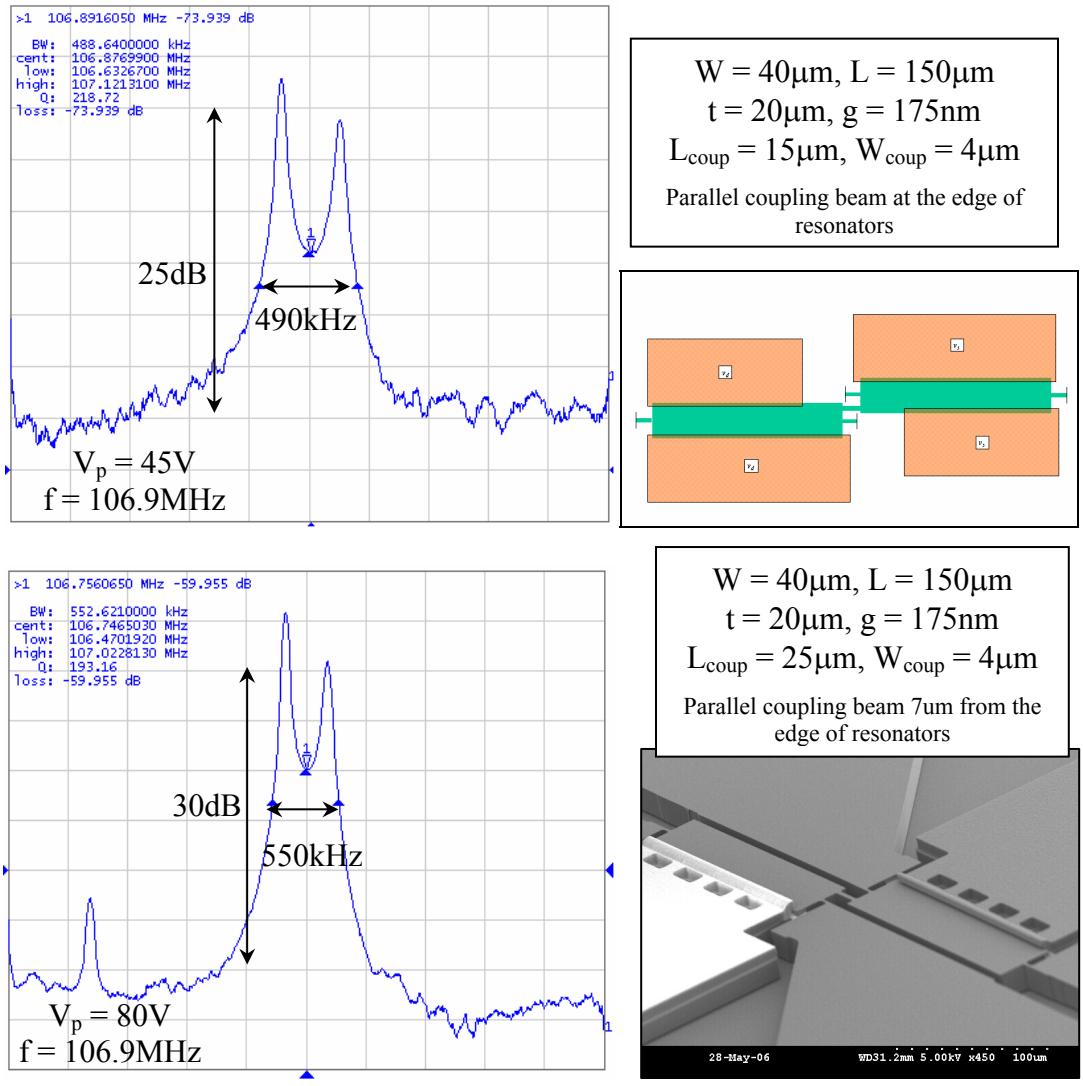

Figure 6.2. Frequency response measured for two different second order mechanically coupled SiBARs with parallel coupling beams.

For demonstration of filter characteristics using coupled resonator arrays much lower resonator impedances or some kind of capacitance cancellation mechanism are required. This is the main challenge for implementation of high frequency filters using the capacitive resonators. Piezoelectric transduction is in general a better candidate for filter implementation because for piezoelectric resonators much larger electromechanical coupling (lower impedances) can be achieved without the need for excessive reduction of the actuator dielectric thickness and introducing large termination capacitances.

Figure 6.3 is an example of a measured resonance response for a coupled SiBAR pair with a perpendicular coupling beam. Surprisingly 4 resonance peaks in close vicinity are observed in the frequency response. Thorough justification of such resonant response requires extensive FEA analysis which is out of scope of this thesis. However, a simple explanation for the observed resonant response is that addition of the perpendicular coupling beam has induced an extra resonance mode with a very close resonant frequency in both the coupled SiBARs in addition to their regular extensional mode. Existence of the coupling element between the too resonators causes coupling and independent second order responses for both modes resulting in the demonstrated frequency response.

Figure 6.4 is the measured frequency response for a through support coupled pair of SiBARs. As expected separation of the two resonance modes is much smaller than the other coupled SiBARs which results from much smaller coupling strength provided by the through support coupling approach. However, as seen in the frequency response of Fig. 6.4, the smaller coupling strength can not compensate the frequency mismatch of the two resonators and the resulting frequency response consists of two independent

resonance peaks with excessive loss. Electrostatic frequency tuning of the SiBARs is not enough to match the frequency of the two resonators and obtain a properly coupled response.

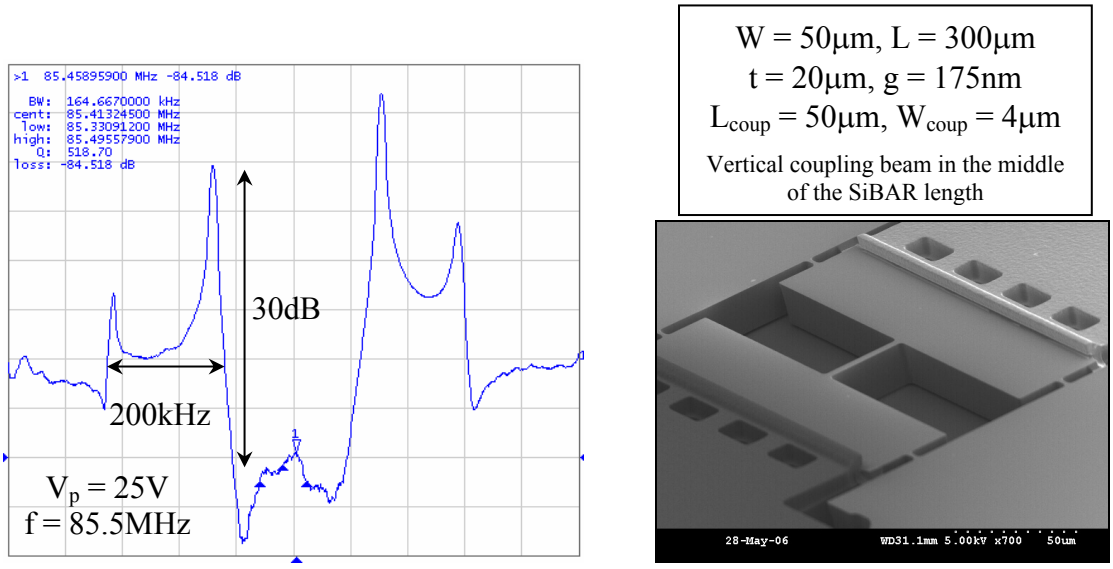

Figure 6.3. Frequency response measured for two mechanically coupled SiBARs with a perpendicular coupling beams.

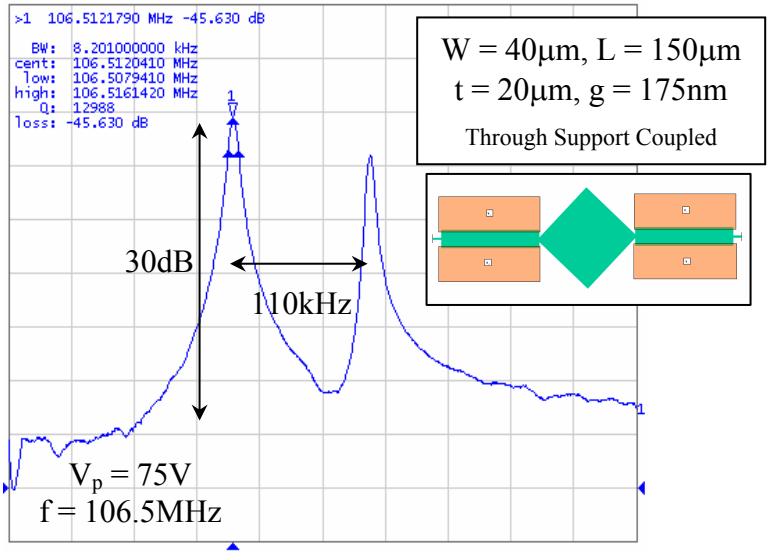

Figure 6.4. Measured frequency response for a second order through support coupled array of SiBARs.

6.2. Electrical Coupling of High Frequency SiBARs

Electrical based resonator coupling techniques were developed under this project and demonstrated in [34,56-59]. The motivations for employment of electrical based coupling techniques instead of mechanical approach are: 1. Achieving much smaller coupling strength and consequently higher filter quality factors is much more straight forward for electrical based approaches, 2. Much better tunability and design flexibility is provided by electrical based approaches. On the other hand tolerances in size and position of the coupling element for mechanically coupled filters will be transfered directly to the filter characteristics and no tuning capability is available for the coupling strength of mechanically coupled resonant systems. This is however at the cost of added bias voltages and complexity to the control circuitry.

Two different electrical based coupling approaches have been previously developed and coupled resonant systems using low frequency beam resonators have been demonstrated for each. In capacitive coupling approach [34,56,58], integrated parallel capacitors to ground added at the interconnect node of the two resonators, generate the extra resonance modes. In the pure electrostatic approach [34,57,59], closely spaced resonators are coupled through the electrostatic forces between them. The nonlinearity of the force applied by the parallel plate actuator formed in between the resonators in this approach is equivalent to the force caused by a negative mechanical stiffness acting between the two structures.

Application of the electrostatic coupling to high frequency SiBARs is not as easy as the lower frequency beam resonators. Due to much larger stiffness of the SiBAR

structures, for electrostatic coupling of such resonators, very large electrostatic stiffness is required to generate strong enough coupling and a distinguishable second resonance mode for the system. This requires nanoscale coupling gaps in the order of the transduction gaps between the resonating SCS bodies of the resonators which is not achievable using the current versions of the HARPSS-On-SOI process.

Fabrication of capacitively coupled SiBARs on the other hand is very straight forward and only requires an added silicon island connecting the output port of the first SiBAR to the input port of the second one. The value of the coupling capacitor in this case will be the electrode to resonator capacitances at the coupling node plus the capacitance between the silicon island and the handle layer of the SOI substrate. Due to comparatively large motional resistance of the high frequency capacitive resonators, achieving small enough coupling capacitor for strong enough coupling and distinguishable resonance peaks can be challenging. One can use ultra-high resistivity handle layer, to avoid the island-handle capacitance. However, for long and thick SiBAR structures with nanoscale capacitive gaps, the electrode resonator capacitances are typically in the hundreds of femto-Farads. Therefore, the minimum achievable coupling capacitor for such filters (resulting in the largest bandwidth) is limited to twice the electrode-resonator capacitance. Moreover, very weak coupling provided by the electrical based approaches, makes frequency matching of the coupled resonators very challenging.

Figure 6.5 shows the measured frequency response of a capacitively coupled pair of 106MHz SiBARs. In this case, the electrode-resonator capacitance for each resonator is 150fF and the silicon island has a capacitance of ~400fF to the SOI handle, resulting in a total coupling capacitance of ~700fF for the device. The impedance for such capacitor at

106MHz is ~2.1kΩ. Therefore, to achieve distinguishably separated resonance peaks for the resonant system, each resonator should have a motional impedance of smaller than 1kΩ which is not easily achievable. Polarization voltages up to 50V were applied to the resonators. As explained in [34] to bias the coupling capacitor at a close to zero DC bias, polarization voltages with different polarities were applied to the two resonators. As can be seen in the frequency response the two resonance peaks are slightly separated clearly demonstrating a second order resonant system. The non-uniformity in the passband can be a result of frequency mismatch between the two resonators or excessive loss in the coupling capacitor.

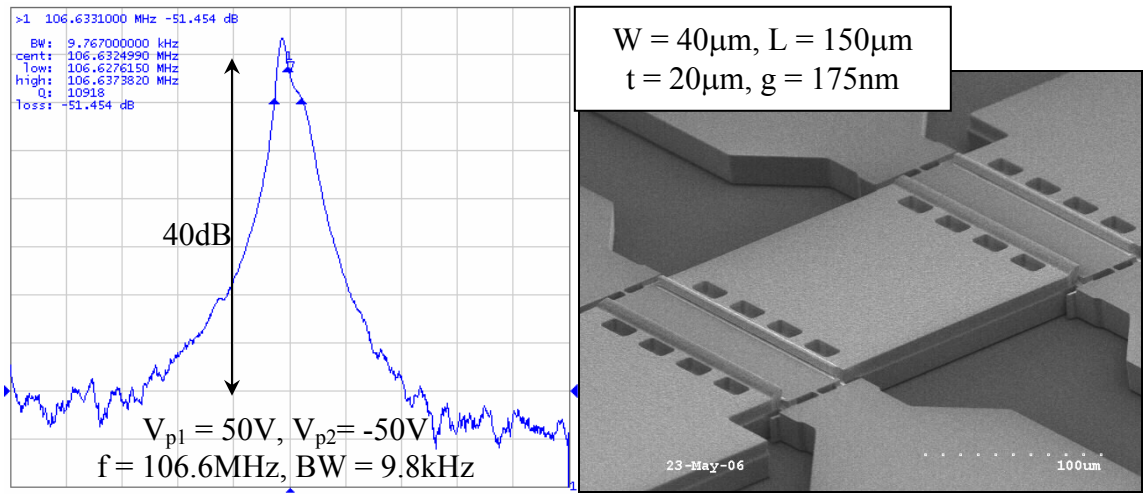

Figure 6.5. Frequency response measured for a capacitively coupled 106MHz SiBAR filter (40um wide, 150um long SiBARs).

In conclusion, according to the measurements and rough calculations presented in this chapter demonstrated for both mechanically and electrically coupled capacitive resonators, implementation of higher order filters at frequencies above 100MHz using capacitive resonators is quite challenging. The major bottlenecks stem from

comparatively weak electromechanical coupling strength of electrostatic transduction mechanism used in such devices. This in turn results in comparatively large motional impedances or extremely large transducer capacitors. As a result termination of such coupled resonators with proper termination resistors to achieve flat passband and low insertion loss is impossible for most filter characteristics. This issue can be overcome by further reduction of the capacitive gaps to 50nm range and below while being able to apply comparatively large polarization voltages to the resonators. This in turn can cause excessive resonator nonlinearity and limit the power handling and dynamic range of the filters. Despite all the advances in silicon capacitive resonator technology, piezoelectric transduction still seems to be a better choice for implementation of high frequency filters. Capacitive filters are superior for lower frequency ultra-narrow bandwidth applications.

CHAPTER VII

WAFER LEVEL HERMETIC SEALING AND CMOS INTEGRATION OF HARPSS CAPACITIVE RESONATORS

A variety of SCS resonators have been developed under this work that have great potential as frequency reference for highly stable, low noise oscillators. High-Q beam resonators, I-BARs and SiBARs can be fabricated simultaneously on a single substrate covering a wide range of frequencies. Beams are a great candidate for low and medium frequency (LF and MF) range (30kHz-3MHz) [4], tunable I-BARs [40-41] can cover the high frequency (HF) range (3-30MHz), and SiBARs [29,47] have demonstrated great performance in the VHF (30-300MHz) range. In addition, although not completely satisfactory yet, possibility of operation of SiBARs in the UHF range (300MHz-3GHz) with high quality factors was demonstrated.

The next step towards implementation of a real product based the silicon resonators that can be used in real world applications, is reliable packaging of such devices. In addition to all the advantages mentioned and demonstrated for the HARPSS-On-SOI fabrication process, this process also provides the great capability for a very convenient encapsulation technique for the fabricated resonators. As demonstrated in the previous sections, the polysilicon electrodes of the SCS HARPSS resonators can bridge over the SCS resonators without physically touching them. This capability has been used to fabricate bridging top interconnects between the electrodes [26-28,47]. It is demonstrated in this chapter that the overlapping electrodes can be extended all the way on top of the resonators providing a polysilicon cap for it. Small openings need to be

made in the polysilicon cap to have electrical isolation between electrodes as well as serve as release openings during the HF release. This can be done by proper resonator layout, without adding any additional process steps to the HARPSS-On-SOI process. Figure 7.1 shows SEM photograph of a SiBAR with extended electrodes on top of it for encapsulation.

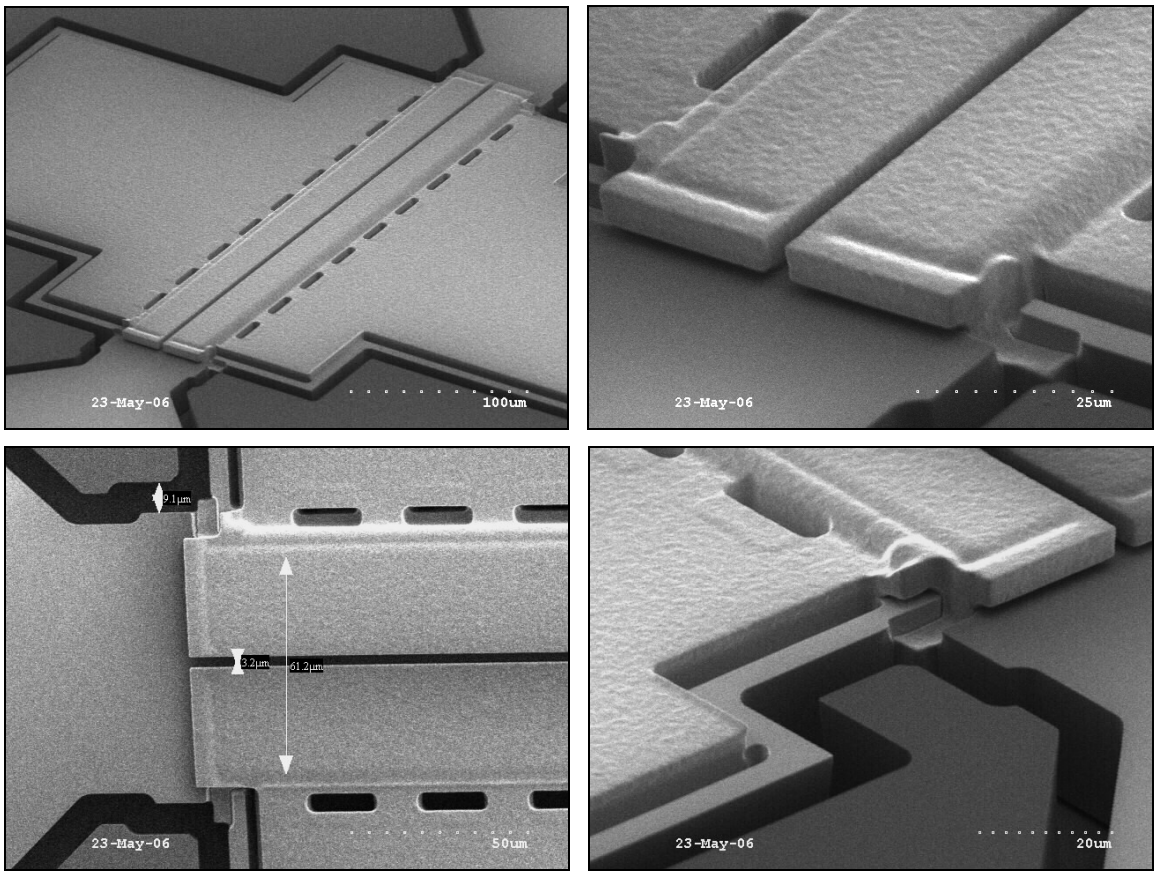

Figure 7.1. SEM views of a SiBAR with extended top electrodes for packaging (20µm thick resonator with 125nm gaps fabricated through the advanced HARPSS-On-SOI process).

As shown in Fig. 7.1, a narrow trench (~2µm wide) separates the electrodes and facilitates HF release of the buried resonator. In addition as opposed to the previously demonstrated resonators, the SOI device layer surrounding the resonators is not removed

to maintain a flat surface for the following packaging related lithography steps. The resonator pads are separated from the rest of the substrate by narrow isolation trenches.

The detailed process steps required for complete sealing of the polysilicon cap as well as performance characterization of the sealed poly cap are described in the following sections.

7.1. PECVD Encapsulation of SiBARs

Figure 7.2 shows the cross-sectional view of HARPSS resonators with overlapping polysilicon electrodes and the proposed hermetic encapsulation technique. The openings in the polysilicon cap first need to be closed by non-conformal deposition of a sealing layer. PECVD oxide was chosen as the non-conformal layer to seal the openings. A thick layer of PECVD oxide (~5-10μm thick) can close-up the openings without penetrating inside the cap and deposition on the resonator (Fig. 7.2b). In addition PECVD oxide is expected to have very low stress. Since PECVD layers typically have a large pin-hole density and are porous compared to the LPCVD films, the main concern about the PECVD sealing layer is its hermeticity and capability to maintain a low pressure inside the cavity. The proposed approach to maintain a high level of hermeticity for the seal is to etch back the PECVD layer (Fig. 7.2c) and deposit a thin layer (~1μm) of LPCVD oxide on top of the cap. In this case one has to assure that the remaining PECVD layer inside the gap after etch back is still covering the opening completely. If small openings are left open in the PECVD seal, the conformal LPCVD layer deposited afterwards will be deposited all over the resonator inside the cap. To assure that the PECVD layer is covering the opening, it needs to be deposited and etched back a few times before LPCVD deposition.

In the end, the capping oxide layers need to be partially removed on top of the pads to allow electrical connection to the underlying resonator (Fig. 7.2d).

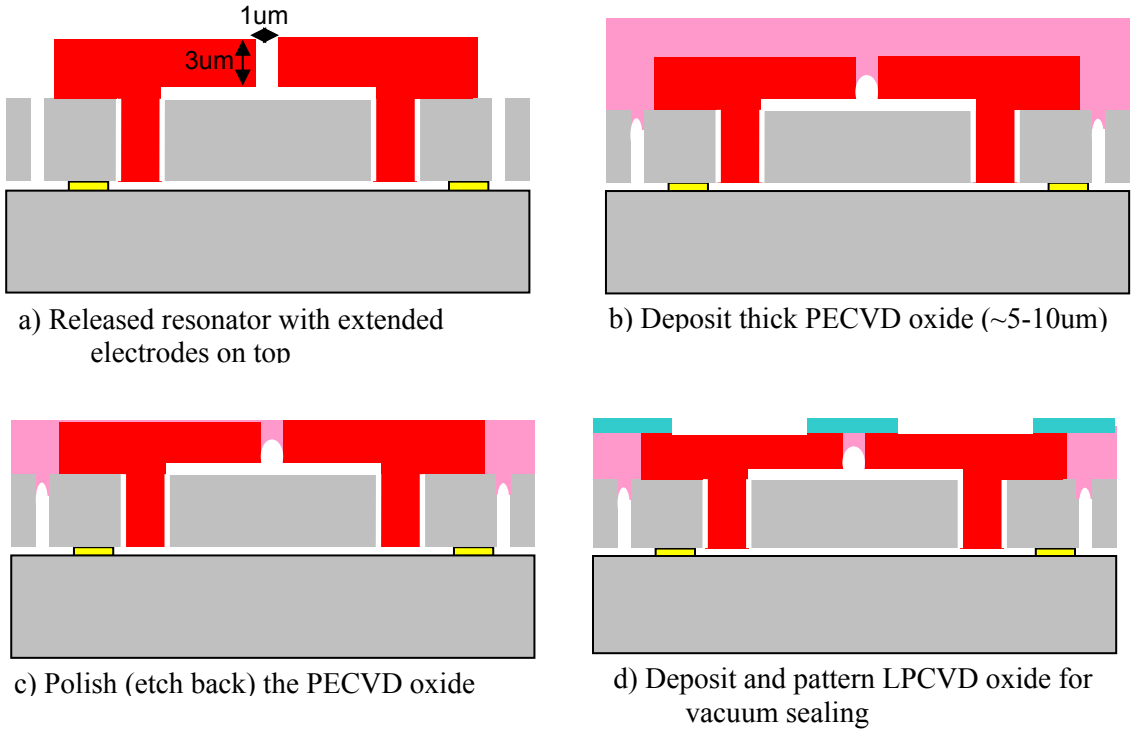

Figure 7.2. Schematic diagram of the wafer level vacuum encapsulation approach proposed for SiBARs.

Figure 7.3 shows the SEM view of the same SiBARs as shown in Fig. 7.1 after deposition of a 2µm layer of PECVD oxide. It is clearly observed that due to its non-conformal deposition, the oxide layer is starting to tighten the trench on the top.

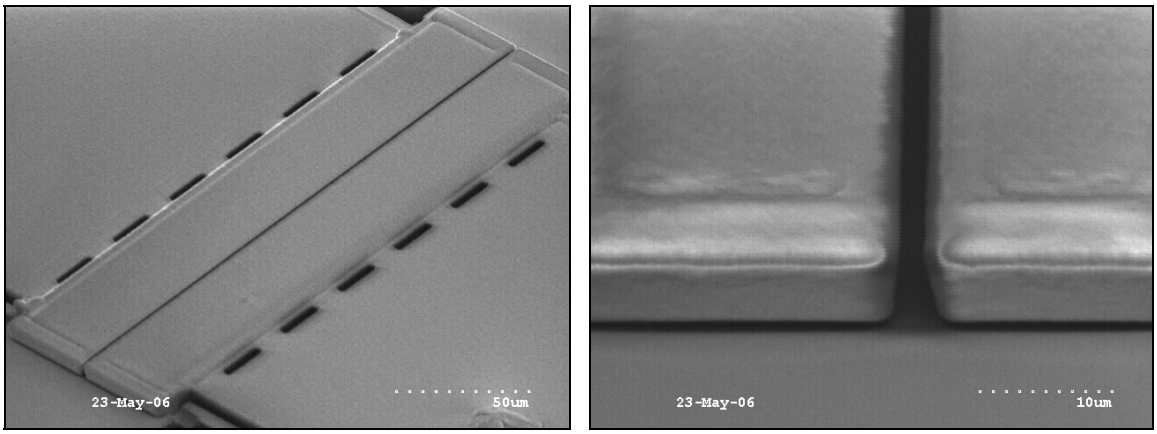

Figure 7.3. Released resonators after deposition of 2um of PECVD oxide.

Figure 7.4 shows the same resonators after deposition of another 6μm of PECVD oxide (total of 8μm). The polysilicon electrode openings are completely sealed, however the trenches isolating the devices from the substrate (which are wider) are not completely covered yet.

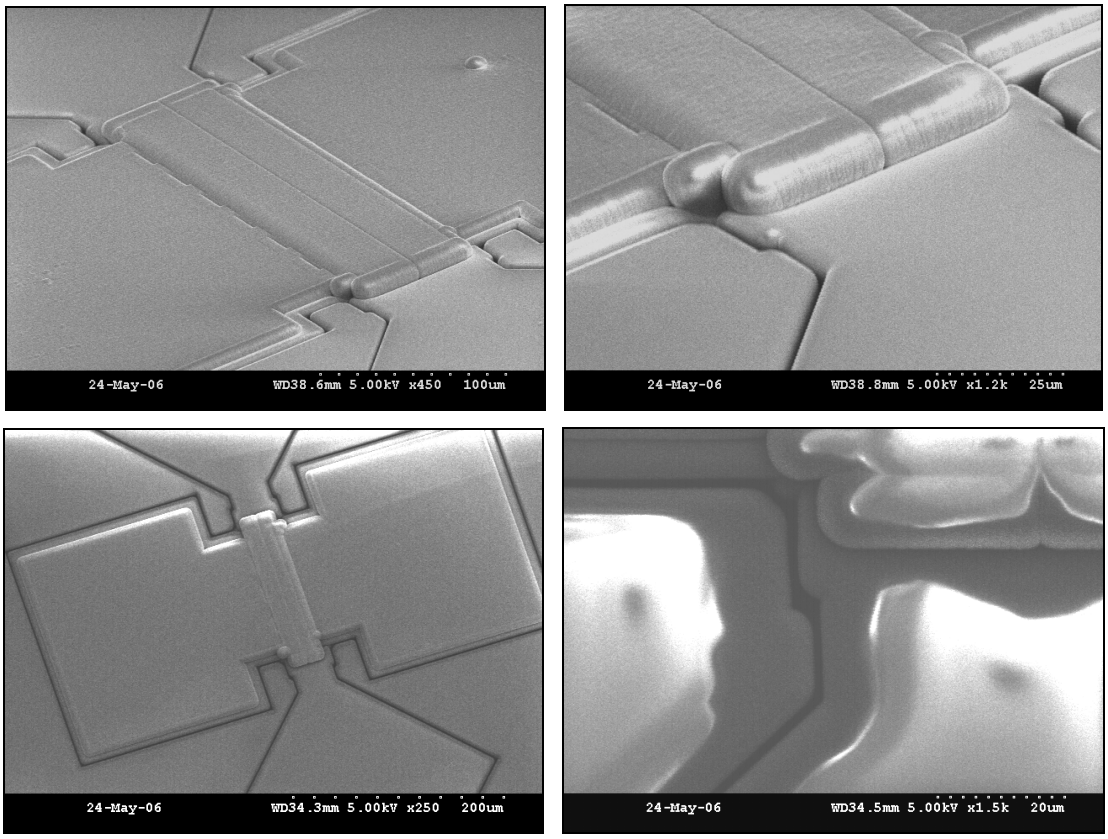

Figure 7.4. Resonators of Fig. 7.3 after deposition of an additional 6um of PECVD oxide (total of 8um oxide). Polysilicon opening is completely closed but the wider isolation trenches around the pads not completely sealed.

Figure 7.5 shows the SEM view of the same resonators after 6μm oxide etch back. As expected, although there is another 2μm of oxide remaining on top of the resonators, the top of the oxide seal on top of the trenches is opened up. Figure 7.6 shows the SEM

view of the same resonators after another 5µm oxide deposition and etch back. After oxide etch back the top of the polysilicon trenches is open again, but the opening size is smaller that of Fig. 7.5. By repeating this deposition and etch back a few times, the seal will remain closed after oxide etch back making the samples ready for the LPCVD oxide deposition.

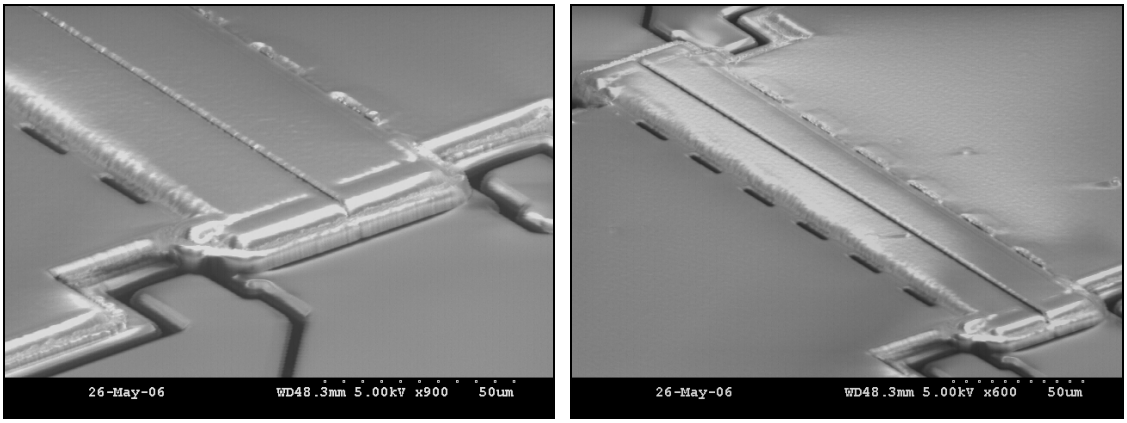

Figure 7.5. PECVD covered resonators after 6µm oxide etch back. (2µm oxide remaining on top).

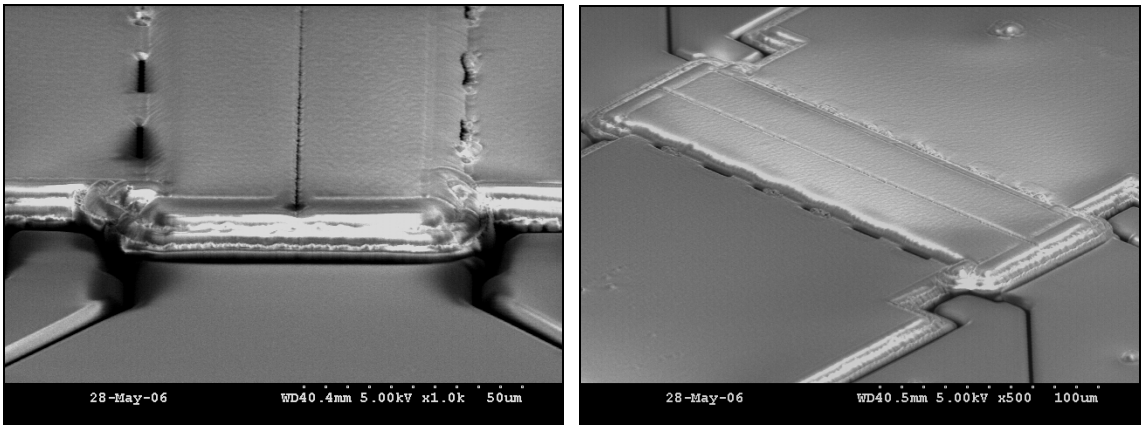

Figure 7.6. PECVD covered resonators after another 5µm deposition and etch back (2µm oxide remaining on top).

For the first sample of resonators it was decided to continue with only the PECVD oxide and characterize its hermeticity. Therefore, another 8µm thick PECVD oxide layer was deposited on the sample resulting in completely sealed resonators of Fig. 7.7. At this point a total of 10µm of oxide exists on top of the devices.

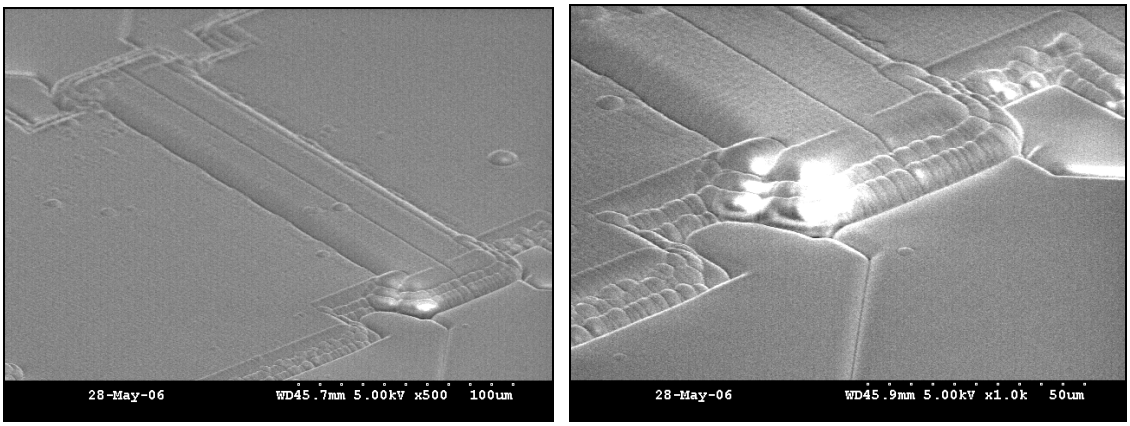

Figure 7.7. PECVD covered resonators after another 8µm deposition to completely seal the openings. A total of 10µm PECVD oxide is covering the resonators on the top.

To open electrical contacts for pads, an additional lithography step was done to etch the oxide on the middle part of the pads while keeping it on the resonator and the isolation trenches. An 8µm thick negative resist (NR4-8000 from Futurrex) was used to pattern the sealing PECVD oxide. Figure 7.8 shows the SEM view of the same resonators after over 10µm oxide plasma etch back silicon surface of the pads exposed. A thin layer of photoresist is still remaining on the resonators.

The encapsulated resonators are now ready for testing and characterization. The following section will report on the measurement results of the sealed resonators and hermeticity and durability of the seal.

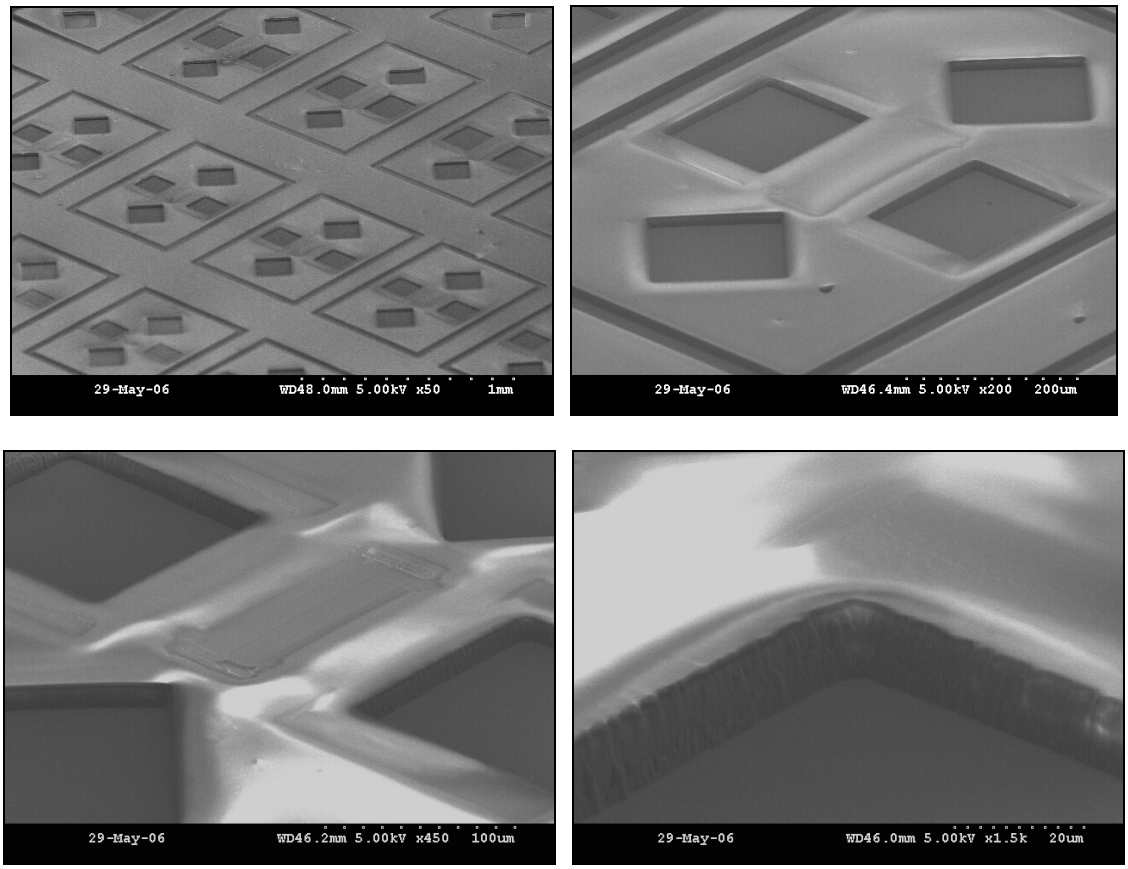

Figure 7.8. Encapsulated resonators after the final lithography and oxide etch to open up electrical connections on the pads.

7.2. Hermeticity and Reliability Testing

One of the most important tests that need to be performed on any package is comparison of the device characteristics before and after encapsulation. Therefore, prior to PECVD oxide deposition and encapsulation of the resonators, some of the released devices were tested in the lab using a regular probe station in air. Figure 7.9 shows the measured resonance peaks for a 40μm wide, 300μm long resonator before encapsulation as well as the measured resonance peak for the exact same device after encapsulation. Not only the quality factor of the resonator has not dropped after several deposition and etch-back steps, but also it shows a slight increase from 25,000 to 31,000. The increase in Q can be due to some level of vacuum maintained inside the cavity by the covering PECVD layer. The final sealing is done inside the PECVD chamber with pressure of a few hundreds of mTorr. If air can not penetrate the thick PECVD oxide layer after exposure of the sample to atmosphere, the same level of vacuum will be maintained inside the package. The resonance frequency of the resonator has slightly decreased from 103.853MHz to 103.809 after encapsulation (424ppm). Decrease in frequency of the resonator is a result of added mass due to slight penetration and deposition of the PECVD oxide on top of the resonator inside the polysilicon cap.

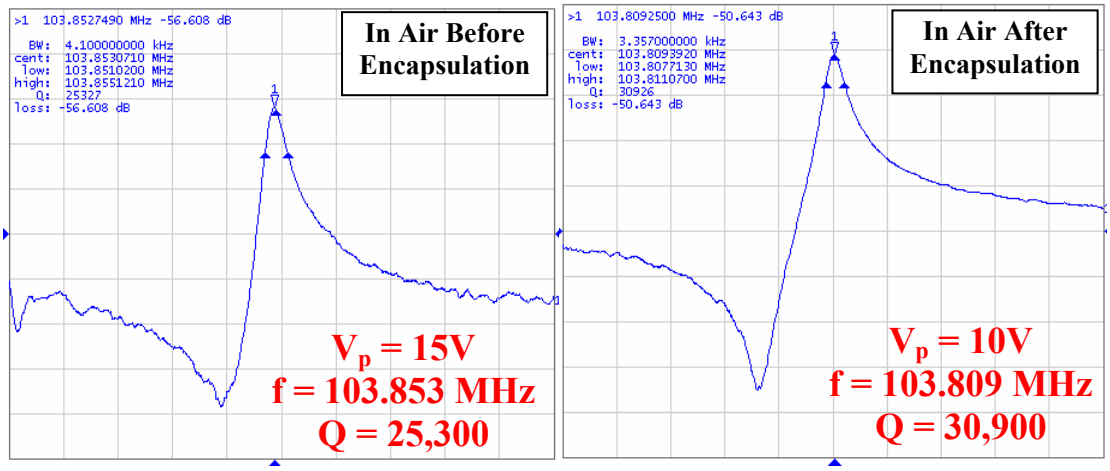

Figure 7.9. Measured resonance peaks for a 40µm wide, 300µm long resonator before and after PECVD oxide encapsulation.

To examine the hermeticity and vacuum maintenance capability of the resonator seals, a 134MHz encapsulated SiBAR was tested in air and then placed inside a vacuum chamber with micro-Torr vacuum level. The resonator was left in the chamber with the pump "on" for over two days. As can be seen in Fig. 7.10, the quality factor does not show a noticeable increase in vacuum. Slight increase in the Q from 17,500 to 18,500 should be due to measurement uncertainties as well as slight changes in Q after resonating for 60 hours. As another proof that the pressure of the surrounding environment does not have any effect on the pressure inside the cavity and consequently resonator Q, the encapsulated resonator was left in air for over another 2 days. The measured Q of 18,700, after such long time of exposure to air, is even slightly higher than the one measured in vacuum (which is due to measurement uncertainty or long term slight changes of resonator characteristics).

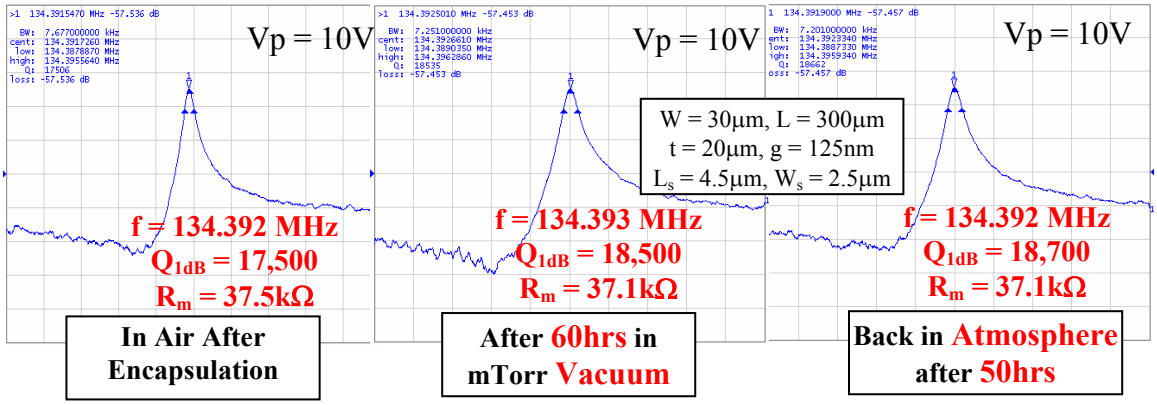

Figure 7.10. Measurement results for an encapsulated resonator. Showing no difference in the measured quality factor when transferring the device from vacuum to atmosphere and vice versa.

To further examine the package reliability and its resistance against penetration of liquids, humidity and contaminations, the same encapsulated resonator was left under water for two days. This was done by dispensing the PCB with the resonator sample attached to it inside a used and unwashed cup of coffee filled with city water. The PCB was taken out after over two days, slightly dried to get rid of the water drops on the PCB, and the resonator was tested again. Figure 7.11 shows that the resulting measured resonance peak demonstrates no noticeable degradation in the quality factor or change in the center frequency of the resonator.

It is worth mentioning that the water test was performed over 2 weeks later than the previous test and the measured resonance frequency right before placing the sample under water was 134.384MHz which shows slight reduction (67ppm) compared to the previous measurement. The difference between the after and right before water test is only 7kHz (52ppm) and can be due to slight changes in room temperature.

Figure 7.12 shows a measured temperature dependant frequency drift of -28.4ppm/°C for the same encapsulated resonator which is similar to an un-packaged resonator showing that the sealing layer does not induce significant stress on the buried resonating body.

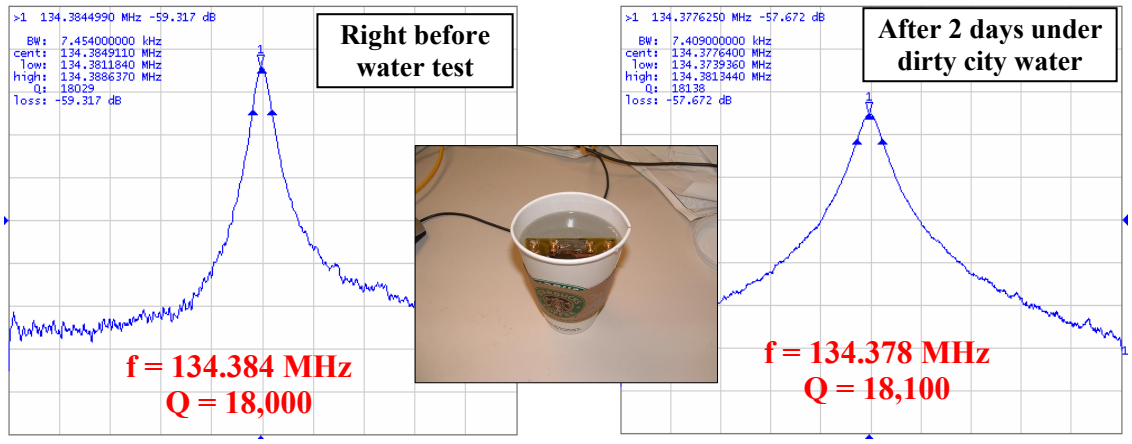

Figure 7.11. Measured resonance peaks for the encapsulated 134MHz resonator before and after dispensing and leaving the sample in dirty city water for over two days.

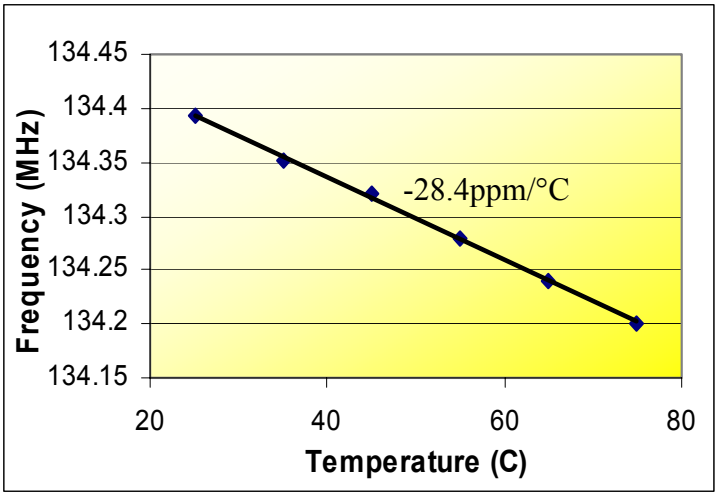

Figure 7.12. Measured temperature drift of frequency for the 134MHz sealed SiBAR.

7.3. Resonator-CMOS Integration: Pre-CMOS MEMS Sealing

One of the major advantages and motivations for fully silicon capacitive resonators compared to their piezoelectric counterparts is their complete material compatibility with silicon IC processes. For HARPSS-based fabrication processes however, the high temperature deposition and oxidation steps as well as the long HF release impose severe limitations and process incompatibilities for monolithic CMOS integration of such devices.

In the first attempt to integrate HARPSS resonators in a CMOS process, the high temperature steps were performed first for the MEMS devices. Such steps include, deposition of the isolation nitride layer, sacrificial oxide thermal growth, poly deposition and doping. The poly was then kept on top of the unreleased MEMS structures to provide a flat surface for the following CMOS lithography steps. Polysilicon also protects the MEMS structures from the oxidation and doping steps of the CMOS process. In this approach an additional lithography and etch step is added to the CMOS flow to form interconnects between the MEMS and CMOS devices by connecting the CMOS second poly to the MEMS poly. The resonators are eventually undercut (isotropic silicon etch plasma) and released in HF after completion of the CMOS devices.

Figure 7.13 shows an optical microscope top view of the SCS beam resonators fabricated next to CMOS circuitry before undercut and release of the resonators. The CMOS process was performed by the MiRC CMOS group in the MiRC cleanroom. The CMOS circuits (simple source follower amplifiers) were tested prior to MEMS release and proved to be operational and not affected by the MEMS structures next to them.

However, HF release of the MEMS devices while protecting CMOS remained an unsolved problem. Different compositions of thick PECVD nitride layers as well as sandwiches of alternative oxide and nitride layers with as high as five thick layers (2-3μm thick each) on top of each other were tried as the protective layer for CMOS devices. However even the thickest and most resistant layers did not survive for more than 5 minutes in 49% HF, while 10-20 minutes of release time is required for HARPSS resonator release.

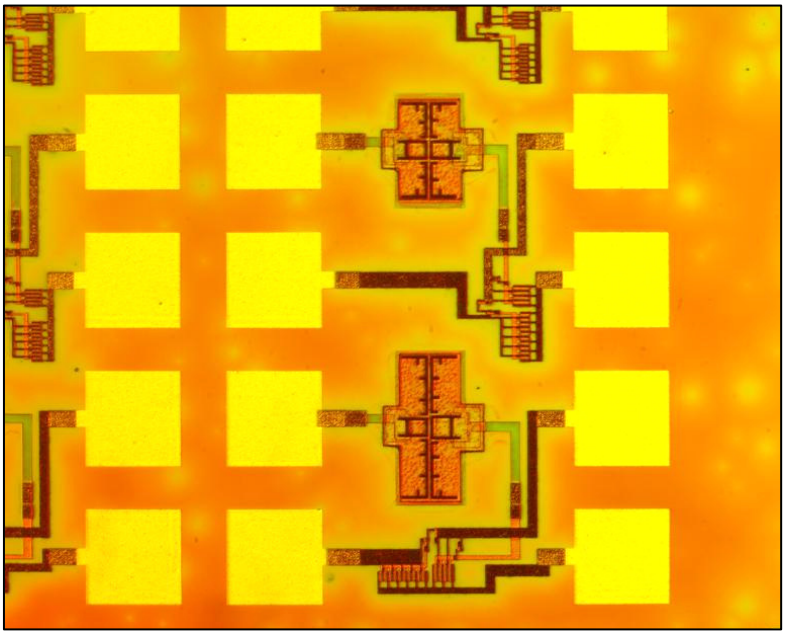

Figure 7.13. Microscope top view of the unreleased beam resonators integrated with CMOS source followers.

A much more convenient and practical approach for CMOS-MEMS integration of HARPSS devices is to perform all the MEMS steps prior to CMOS processing. The poly-oxide encapsulation technique discussed in the previous sections is a very strong enabling technology for this integration scheme. In this approach, the resonators are

fabricated, released and encapsulated first. The regular CMOS process can then be performed on the silicon substrate on top of the resonators. If the MEMS sealing is hermetic enough, CMOS process steps will not have a destructive effect on the resonator performance. Figure 7.14 shows the proposed process steps for pre-CMOS MEMS fabrication followed by CMOS fabrication. To provide a flat surface for following CMOS lithography steps, the MEMS area is to be etched back a few microns prior or after resonator fabrication (Fig. 7.14a). Similar encapsulation steps using polysilicon covering electrodes, non-conformal PECVD oxide layers and hermetic LPCVD oxide film are then performed on the resonators and the substrate is polished back(Fig. 7.14e). CMOS process with no changes can then be performed on the surrounding silicon substrate and on top of the resonators. Making interconnects between MEMS and CMOS devices will be as simple as making a substrate contact in the CMOS process. For this purpose parts of the resonator silicon pads need to be outside the etched-back MEMS area to be accessible by the CMOS substrate contacts (Fig. 7.14f). The integrated MEMS devices implemented in this approach are already encapsulated and the regular packaging used for CMOS ICs can be used for final packaging of such integrated systems.

According to the test results obtained from the encapsulated resonators in the previous section showing excellent hermeticity without even using an LPCVD sealing layer, the proposed approach for monolithic integration of MEMS resonators (as well as other sensors and actuators) is expected to be very reliable, convenient and low-cost.

Due to unavailability of a reliable in house CMOS process and the amount of time and effort required for CMOS processing, practical implementation of the proposed approach is out of the scope of this thesis.

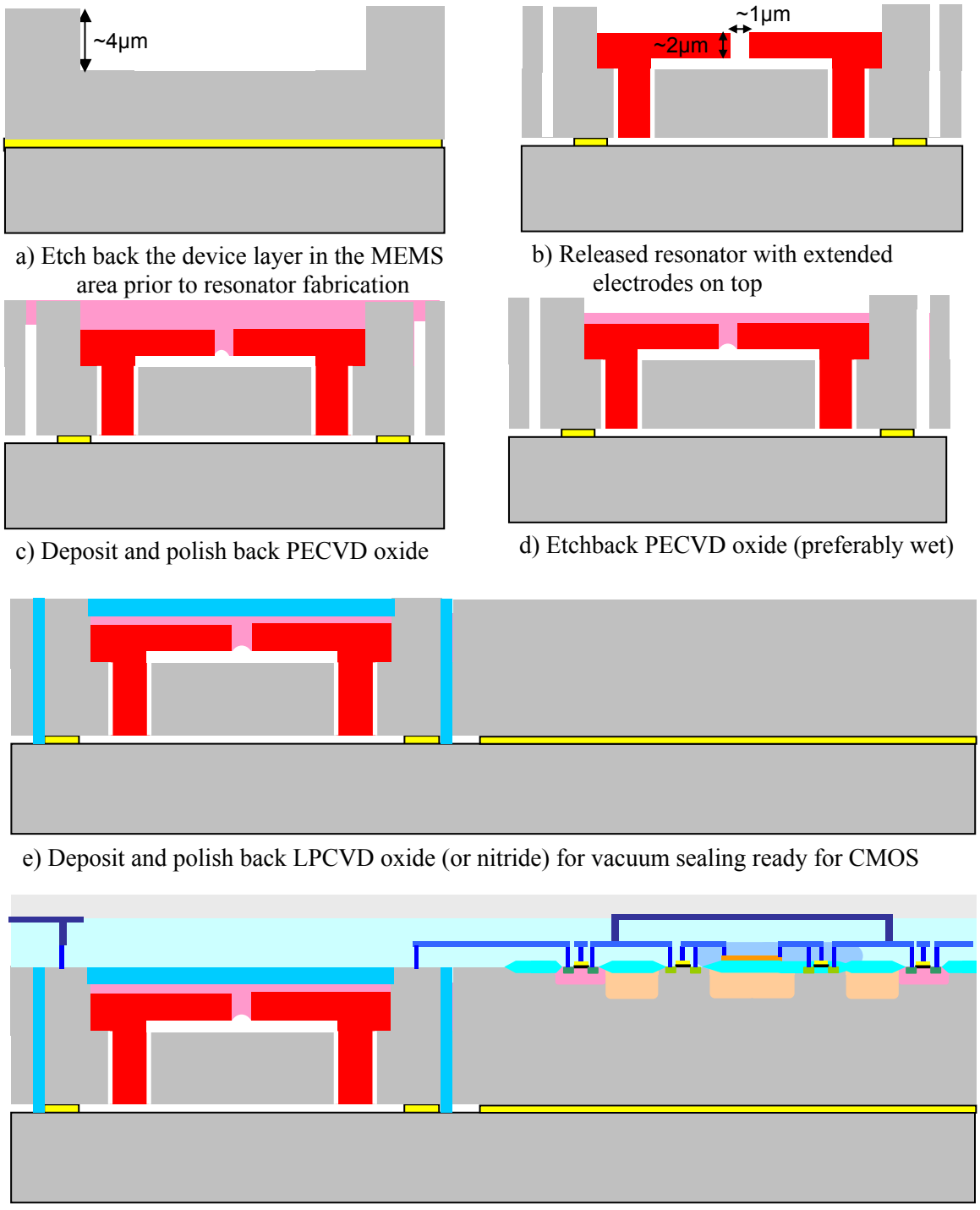

a) Etch back the device layer in the MEMS area prior to resonator fabrication

b) Released resonator with extended electrodes on top

c) Deposit and polish back PECVD oxide

d) Etchback PECVD oxide (preferably wet)

e) Deposit and polish back LPCVD oxide (or nitride) for vacuum sealing ready for CMOS

f) Regular CMOS processing, MEMS interconnects as substrate contacts

Figure 7.14. Cross sectional Schematic diagram for post-MEMS fabrication of integrated CMOS circuitry on top of the polysilicon-oxide encapsulated resonators.

CHAPTER VIII

CONCLUSIONS AND FUTURE WORK

8.1. Contributions

The following is a list of contributions that have been achieved in this work.

- Low frequency single crystal silicon (SCS) resonators including both clamped-clamped and clamped-free beam resonators were fabricated on regular silicon substrates using a modified version of the original HARPSS process. High sensitivity amplifying test circuits were implemented for characterization of the fabricated resonators. Resonators with operating frequency in the 15kHz-1MHz range and quality factors as high as 74,000 for clamped-clamped and 184,000 for clamped-free beams in vacuum were demonstrated using the test circuits. Resonance frequencies as high as 12MHz were demonstrated by the clamped-clamped beam resonators operating in their higher flexural modes.

- Electrical equivalent circuit for two-port capacitive micromechanical resonators operating in their linear region was derived. Electromechanical coupling and electrostatic tuning coefficients were derived for clamped-clamped beam resonators in their first flexural resonance mode as well as for disk resonators operating in their elliptical bulk resonance mode.

- A new version of the HARPSS fabrication process modified for fabrication of bulk mode SCS disk and block resonators with ultra-thin (deep submicron) capacitive gap size on SOI substrates was developed. The fabrication process was

debugged and optimized in several steps before successful fabrication of operational high frequency resonators. Operating frequency, motional resistance, electrostatic tuning, temperature drift and quality factor both in vacuum and atmospheric pressure was measured for the fabricated disk resonators. Among the measured resonators, a 3μm thick single side supported disk resonator with diameter of 30μm demonstrated a quality factor of 40,000 in vacuum at resonance frequency of 148MHz.

- A new processing technique based on dry etching of high aspect ratio deep-submicron capacitive gaps, for implementation of high frequency fully SCS capacitive resonators on SOI substrates was developed. Successful fabrication and operation of high frequency resonators using this technique was demonstrated.

- An improved version of the HARPSS on SOI process consisting of only three mask layers and consequently a much higher processing yield was developed. Several types of thick SCS disk and block resonators with thickness as high 30μm and deep submicron capacitive gaps were fabricated using this approach. Improved performance and lower electrical equivalent resistance for thick resonators was demonstrated.

- New resonator structures referred to as silicon bulk acoustic resonators (SiBAR) were developed based on the FBAR structures providing large transduction area while having high operating frequencies. Impedances as low as a few kiloOhms, quality factors as high as 20,000-60,000 in the VHF frequency range up to 300MHz were demonstrated for the SiBARs operating in their first width

extensional mode. Operating frequencies as high as 983MHz were measured for the higher modes of the SiBARs.

- The second generation SiBARs with optimized dimensions demonstrated motional resistances as low as 200Ω and quality factors as high as ~100,000 in the ~100MHz frequency range. Higher resonance modes of such resonators demonstrated frequencies as high as 1.5GHz with impedance in the tens of kOhm range, which is an order of magnitude smaller than other reported values for capacitive resonators.

- Several versions of ultra-long high frequency bulk mode resonant structures were fabricated using the HARPSS on SOI process. VHF resonators with comparatively low impedances were demonstrated using the SiBAR based structures with a very large effective length. Effect of different supporting schemes on the quality factor and spurious modes of the resonators was investigated.

- Electrically and mechanically coupled resonators with frequencies in the ~100MHz range were demonstrated. Different mechanical coupling schemes were investigated for demonstration of higher order resonant systems as well as coupled arrays of resonators for motional impedance reduction.

- An advanced version of the HARPSS-On-SOI process was developed and characterized. The poly etching step which was the problematic part of the previous version of the HARPSS-On-SOI process was completely eliminated. In addition, the existing limits on the gap aspect ratio and minimum achievable gap

size in the 3-mask HARPSS-On-SOI process were eliminated. Moreover, additional dielectric thin film and lithography step added to the capabilities of this process significantly. Operational resonators with capacitive gaps as small as 65nm and gap aspect ratio as high as 460 were demonstrated using the advanced HARPSS-On-SOI process. Such resonators can demonstrate sub-kiloOhm impedances with polarization voltages less than 10V.

- A wafer level vacuum packaging technology taking advantage of the overlapping resonator electrodes was developed. Encapsulation using non-conformal PECVD oxide layers was proven to be capable of maintaining vacuum and reliably protect the resonator against liquids and contaminations.

Below is a list of patents, patent applications, and invention disclosures that have so far occurred under this research:

- Patents, Patent Applications and Invention Disclosures

1. F. Ayazi, and S. Pourkamali, "Capacitive resonators and methods of fabrication," US patent No. 7,023,065, April 2006.

2. F. Ayazi, and S. Pourkamali, "Electrically-coupled micro-electro-mechanical filter systems and methods," US patent application No. 20040058591, March 2004.

3. F. Ayazi, R. Abdolvand and S. Pourkamali, "Methods of forming oxide masks with submicron openings therein and microstructures formed thereby," US patent No. 7,056,757, June 2006.

4. F. Ayazi, S. Pourkamali and G. K. Ho, "Capacitive Vertical Silicon Bulk Acoustic Resonator (SiBAR)," US patent application No. 20060044078, March 2006.

5. F. Ayazi, G. K. Ho, and S. Pourkamali, "Highly tunable low-impedance capacitive micromechanical resonators, oscillators, and processes relating thereto," US patent application No. 20060125576, June 2006.

6. F. Ayazi, and S. Pourkamali, "CMOS compatible wafer level vacuum packaging," Invention disclosure filed at Georgia Tech. Office of Technology Licensing, GTRC ID No. 3802, March 2006.

Below is a list of publications that have so far occurred under this research:

- Journal Papers

1. S. Pourkamali, G. K. Ho and F. Ayazi, "Low-impedance VHF and UHF capacitive silicon bulk acoustic resonators," ready for submission to JMEMS.

2. K. Sundaresan, G. K. Ho, S. Pourkamali and F. Ayazi, "Electronically temperature compensated Silicon bulk acoustic resonator reference oscillators," submitted for review, IEEE Journal of Solid-State Circuits.

3. S. Pourkamali and F. Ayazi, "Electrically coupled MEMS bandpass filters-Part I: with coupling element," Journal of Sensors and Actuators A 122, 2005, pp.307-316.

4. S. Pourkamali and F. Ayazi, "Electrically coupled MEMS bandpass filters-Part II: without coupling element," Journal of Sensors and Actuators A 122, 2005, pp.317-325.

5. S. Pourkamali, Z. Hao and F. Ayazi, "VHF single crystal silicon side supported disk resonators-Part II: implementation and characterization," Journal of Micro Electro Mechanical Systems, Vol. 13, Issue 6, December 2004, pp. 1054-1062.

6. Z. Hao, S. Pourkamali and F. Ayazi, “VHF single crystal silicon side supported disk resonators-Part I: Design and Modeling,” Journal of Micro Electro Mechanical Systems, Vol. 13, Issue 6, December 2004, pp. 1043-1053.

7. S. Pourkamali, et al, “High-Q single crystal silicon HARPSS capacitive beam resonators with self-aligned sub-100nm transduction gaps,” Journal of Micro Electro Mechanical Systems, Vol. 12, Issue 4, August 2003, pp. 487-496.

- Conference Papers

1. F. Ayazi, S. Pourkamali, G. K. Ho and R. Abdolvand, “High-aspect-ratio SOI vibrating micromechanical resonators and filters,” invited paper, to appear in proceeding, International Microwave Symposium, 2006 (IMS’06).

2. K. Sundaresan, G. K. Ho, S. Pourkamali and F. Ayazi, “A low phase noise 100MHz silicon BAW reference oscillator,” to appear in proceedings, Custom Integrated Circuit Conference, 2006 (CICC’06).

3. S. Pourkamali and F. Ayazi, “High frequency low impedance silicon BAR structures,” Proceedings, Hilton Head 2006, solid-state sensor, actuator and Microsystems workshop, pp. 284-287.

4. G.K. Ho, K. Sundaresan, S. Pourkamali and F. Ayazi, “Temperature compensated IBAR reference oscillators,” proceeding, MEMS’06, pp. 910-913.

5. S. Pourkamali, G. K. Ho and F. Ayazi, “Vertical Capacitive SiBARs,” proceedings, MEMS’05, pp. 211-214.

6. G.K. Ho, K. Sundaresan, S. Pourkamali and F. Ayazi, "Low impedance, highly tunable, I2-resonators for temperature compensated reference oscillators,” proceedings, MEMS’05, pp. 116-120.

7. K. Sundaresan, G.K. Ho, S. Pourkamali and F. Ayazi, "A 2-chip micro-electro-mechanical reference oscillator," proceedings, ISCAS‘05, pp.5461-5464.

8. S. Pourkamali and F. Ayazi, “High frequency capacitive micromechanical resonators with reduced motional resistance using the HARPSS technology,” proceedings, 5th Silicon RF topical meeting 2004, pp. 147-150.

9. Z. Hao, S. Pourkamali and F. Ayazi, “Longitudinal block resonators for detecting mass variation at single molecule sensitivity,” the Fifth Georgia Tech Conference on Nanoscience and Nanotechnology, November 2004.

10. S. Pourkamali and F. Ayazi, “18μm thick high frequency capacitive HARPSS resonators with reduced motional resistance,” proceedings, Hilton Head 2004, solid-state sensor, actuator and Microsystems workshop, pp. 392-393.

11. S. Pourkamali, and F. Ayazi, “Fully single crystal silicon resonators with deep-submicron dry-etched transducer gaps,” proceedings, MEMS’04, pp. 813-816.

12. S. Pourkamali, R. Abdolvand, G. K. Ho, and F. Ayazi, “Electrostatically coupled micromechanical beam filters,” proceedings, MEMS’04, pp. 584-587.

13. S. Pourkamali, and F. Ayazi, “SOI-based HF and VHF single-crystal silicon resonators with sub-100nm vertical capacitive gaps,” proceedings, Transducers ’03, 2003, pp.837-840.

14. S. Pourkamali, R. Abdolvand, and F. Ayazi, “A 600kHz electrically coupled MEMS bandpass filter,” proceedings, MEMS‘03, 2003, pp. 702-705.

15. S. Y. No, A. Hashimura, S. Pourkamali, F. Ayazi, “Single crystal silicon HARPSS capacitive resonators with submicron gap spacings,” proceedings, Hilton Head 2002, solid-state sensor, actuator and Microsystems workshop, pp. 281-284.

8.2. Future Directions

The capacitive SCS resonator technology developed under this project has a great potential for implementation of commercialized monolithic highly stable frequency references. High performance resonators with quality factors in the tens of thousand covering a wide range of frequency starting from tens of kHz to hundreds of MHz have been demonstrated. The demonstrated encapsulation technique can be used to reliably manufacture and maintain such frequency references for real world applications. Moreover, CMOS integration of such encapsulated resonators seems to be straight forward. A few remaining issues as well as open areas for further research in this area are as follows:

1. Temperature compensation: temperature stability of the silicon based micromechanical frequency references, although much better than that of LC or CMOS based references, is close to one order of magnitude worse than that of the most unstable quartz crystals currently available in the market. Some work associated to this thesis has been done to electrically compensate the temperature induced frequency drift of lower frequency resonators by taking advantage of the electrostatic tuning capability of the capacitive resonators [40,41]. Frequency stability better than non-compensated quartz crystal and close to temperature compensated quartz crystals (TCXO) has been demonstrated using this approach [41] while maintaining much smaller size and lower power consumption. The thermal tuning approach is under consideration as a viable solution for higher frequency resonators. A large amount of research is yet to be done on the thermal

based compensation techniques to investigate its reliability, identify the limits and minimize its power consumption. The other approach for high frequency silicon resonators would be material compensation by canceling the temperature dependant drift in the Young's modulus of the structural material by adding a material with an opposite behavior to the structure.

2. Fabrication tolerance characterization and compensation: frequency tolerance between fabricated resonators with same design and dimensions can be a major issue for a commercialized resonator-based products. When targeting an extremely stable frequency reference, fabrication tolerances as high as a few tens of ppm can be a limiting factor. Under this work there has not been a precise and extensive characterization and measurement of frequency tolerance between similar fabricated resonators. Therefore, this remains as an open area for further research. Resonator designs that can be robust to slight dimensional changes due to fabrication tolerances are of great interest as a topic for further research.

3. Long Term Stability and Reliability: most of the measured data presented in this work has been based on short term measurements in the lab for unpackaged resonators. Even the comparatively long term packaged resonator test data does not exceed a few days. For a commercialized product long term stability and reliability over a period of a few year is a mandatory requirement. Looking into the long term behavior of the packaged resonators including, frequency drift, quality factor drift, shock resistance and reliability is another open area for further research.

4. Identification and Improvement of Process Limits: although potentially it is possible to achieve capacitive gap sizes as small as a few nm using the HARPSS-based fabrication processes, capacitive gaps smaller than 60nm have not been demonstrated reliably yet. The process yield and resonator quality factors start to drop drastically as the capacitive gap sizes shrink to sub-100nm. Identification of the physical limit behind this issue and achieving capacitive gaps in the 30nm and below can open up the opportunity of covering the whole UHF range (300MHz-3GHz) by high performance, low impedance capacitive resonators. In addition, the major problem associated with implementation of capacitive high frequency filters which is their comparatively large impedances could be resolved this way.

REFERENCES

[1] R. A. Johnson, “Mechnical filters in electronics,” A Wiley-interscience publication.

[2] C. T.-C. Nguyen, “Vibrating RF MEMS for next generation wireless applications,” Proceedings, 2004 IEEE Custom Integrated Circuits Conf., pp. 257-264.

[3] W.-T. Hsu, J. Clark, C. T.-C. Nguyen, “Q-Optimized Lateral Free-Free Beam Micromechanical Resonators,” Transducer’01, Germany, pp. 1110-1113.

[4] S. Pourkamali, et al , “High-Q Single Crystal Silicon HARPSS Capacitive Beam Resonators with Self-Aligned Sub-100nm Transduction Gaps,” Journal of Micro Electro Mechanical Systems, August 2003, pp. 487-496.

[5] V. Kaajakari et al, “Square-extentional mode single-crystal silicon micromechanical RF-resonator,” Transducers ’03, pp. 951-954.

[6] M. E. Frerking, “Fifty years of progress in quartz frequency standards,” 1996 IEEE international frequency control symposium, pp. 33-46.

[7] Y. L. Vorokhovsky, B.G. Drakhlis, “High-stability quartz oscillators on internally heated quartz resonators with AT and SC cuts,” Proceedings of the 45th Annual Symposium on Frequency Control, 1991, pp. 447 –451.

[8] S. Fujishima, “The history of ceramic filters,” IEEE Transactions on Ultrasonics, Ferroelectrics and Frequency Control, Volume: 47, Issue: 1, Jan. 2000 pp. 1-7.

[9] P. V. Wright, “A review of SAW resonator filter technology,” IEEE Ultrasonics Symposium, 1992, pp. 29-38.

[10] M. Ueda, et al, “Ultra-miniaturized and high performance PCS SAW duplexer with steep cut-off filters,” MTT-S 2004, Vol. 2, pp.913–916.

[11] R. C. Ruby, et al, “Thin film bulk wave acoustic resonators (FBAR) for wireless applications,” Ultrasonics Symposium, 2001, Vol. 1, pp. 813 – 821.

[12] D. T. Chang, et al, “A new MEMS-based quartz resonator technology,” proceedings, Hilton Head 2004, pp. 41-44.

[13] S. Humad, R. Abdolvand, G. K. Ho and F. Ayazi, "High Frequency Micromechanical Piezo-on-Silicon Block Resonators," in Proc. IEEE International Electron Devices Meeting (IEDM'03), pp. 957-960.

[14] G. Piazza and A. P. Pisano, “Dry-released post-CMOS compatible contour-mode aluminum nitride micromechanical resonators for VHF applications,” proceedings, Hilton Head 2004, pp. 37-40.

[15] W.C. Tang, T.-C. Nguyen, and R.T. Howe, "Laterally driven polysilicon resonant microstructures," Sensors and Actuators, vol.20, pp. 25-32, 1989.

[16] J. R. Clark, W.-T. Hsu, and C. T.-C. Nguyen, "High-Q VHF micromechanical contour-mode disk resonators," IEEE Int. Electron Devices Meeting 2000, pp. 399-402.

[17] M.W. Putty, S.C. Chang, R.T. Howe, A.L. Robinson, K.D. Wise, "One-Port Active Polysilicon Resonant Microstructures," Proceedings, An Investigation of Micro Structures, Sensors, Acutators, Machines, and Robots, IEEE, 1989, pp.60-65.

[18] R.T. Howe, "CMOS micromechanical resonator oscillator," Tech. Dig. IEEE Int. Electron Devices Meeting, Washington D.C., Dec. 5-8, 1993, pp.199-202.

[19] M. A. Abdelmoneum, et al, "Stemless wine-glass-mode disk micromechanical resonators," MEMS'03, pp. 698-701.

[20] S.-S. Li, Y.-W. Lin, Y. Xie, Z. Ren, and Clark T.-C. Nguyen, "Micromechanical hollow-disk ring resonators," MEMS'04, pp. 821-824.

[21] Y. Xie, S.-S. Li, Y.-W. Lin, Z. Ren, and C. T.-C. Nguyen, "UHF micromechanical extensional wine-glass mode ring resonators," 2003 IEEE International Electron Devices Meeting (IEDM'03), pp. 953-956.

[22] J. Wang, Z. Ren, and C. T.-C. Nguyen, "Self-aligned 1.14GHz vibrating radial-mode disk resonators," Transducers'03, pp. 947-950.

[23] M. U. Demirci, M. A. Abdelmoneum, and C. T.-C. Nguyen, "Mechanically corner-coupled square microresonator array for reduced series motional resistance," Transducers'03, pp. 955-958.

[24] S. Pourkamali, and F. Ayazi, "Fully single crystal silicon resonators with deep-submicron dry-etched transducer gaps," MEMS'04, pp. 813-816.

[25] S. Pourkamali, and F. Ayazi, "SOI-based HF and VHF single-crystal silicon resonators with sub-100nm nanometer vertical capacitive gaps," Transducers '03, pp.837-840.

[26] S. Pourkamali, et al, "VHF single crystal silicon capacitive elliptic bulk-mode disk resonators part II: implementation and characterization," Journal of Micro Electro Mechanical Systems, Vol. 13, Issue: 6, Dec 2004, pp. 1054-1062.

[27] S. Pourkamali and F. Ayazi, "High frequency capacitive micromechanical resonators with reduced motional resistance using the HARPSS technology," proceedings, 5th Silicon RF topical meeting 2004, pp. 147-150.

[28] S. Pourkamali and F. Ayazi, "18μm thick high frequency capacitive HARPSS resonators with reduced motional resistance," proceedings, Hilton Head 2004, pp. 392-393.

[29] S. Pourkamali, G. K. Ho and F. Ayazi, “Vertical capacitive SiBARs,” Proceedings, MEMS’05, pp. 211-214.

[30] H. C. Nathanson, W. E. Newell, R.A. Wickstrom and J.R. Davis, “The resonant gate transistor,” IEEE Trans. Electron Devices, vol. ED-14, pp. 117-133, 1967.

[31] K. Petersen, et al., “Resonant Beam Pressure Sensor Fabricated with Silicon Fusion Bonding,” Tranducer’91, pp.664-667.

[32] W. -T. Hsu, J. R. Clark, and C. T. -C. Nguyen, “A resonant temperature sensor based on electrical spring softening,” Transducers’01, pp. 1484-1487.

[33] A.-C. Wong, C.T.-C. Nguyen, “Micromechanical mixer-filters (“mixlers”),” JMEMS, Vol. 13, Issue: 1, Feb. 2004, pp. 100 – 112.

[34] S. Pourkamali, “Electrically coupled MEMS bandpass filters,” Master of science thesis, Department of Electrical and Computer Engineering, Georgia Institute of Technology, April 2004.

[35] F. Ayazi and K. Najafi, "A HARPSS Polysilicon Vibrating Ring Gyroscope," Journal of Micro Electro Mechanical Systems, June 2001, pp. 169-179.

[36] F. Ayazi and K. Najafi, “High Aspect-Ratio Combined Poly and Single-Crystal Silicon (HARPSS) MEMS Technology,” Journal of Micro Electro Mechanical Systems, 9(3), 288, (2000).

[37] K. A. Shaw, Z.L. Zhang, N. C. MacDonald, “SCREAM I: A single mask, single-crystal silicon process for microelectromechanical structures,” Proceedings, MEMS '93, pp. 155-160.

[38] K. A. Shaw, N. C. MacDonald , “Integrating SCREAM micromachined devices with integrated circuits,” Proceedings, MEMS '96, pp. 44-48.

[39] M. Puech, et al., “A Novel Plasma Release Process and a Super High Aspect Ratio using ICP Etching for MEMS,” SEMICON, Japan, Dec. 2003.

[40] G.K. Ho, K. Sundaresan, S. Pourkamali, and F. Ayazi, "Low-motional_impedance highly-tunable I2 resonators for temperature-compensated reference oscillators," Proceedings, MEMS'05, Jan. 2005, pp.116-120.

[41] G.K. Ho, K. Sundaresan, S. Pourkamali and F. Ayazi, "Temperature compensated IBAR reference oscillators," Proceedings, MEMS 2006, Jan. 2006, pp. 910-913.

[42] H, Chandrahalim, D. Weinstein, L. F. Cheow, and S. A. Bhave, “Channel-select micromechanical filters using high-K dielectrically transduced MEMS resonators,” Proceedings, MEMS’06, Jan. 2006, pp. 894-897.

[43] S. A. Bhave, and R. T. Howe, "Silicon nitride-on-silicon bar resonator using internal electrostatic transduction," Proceedings, Transducers2005, pp. 2139 – 2142.

[44] Z. Hao, S. Pourkamali and F. Ayazi, "VHF single crystal silicon side supported disk resonators-Part I: Design and Modeling," Journal of Micro Electro Mechanical Systems, Vol. 13, Issue 6, December 2004, pp. 1043-1053.

[45] Don L. DeVoe, "Piezoelectric Thin Film Micromechanical Beam Resonators," Sensors and Actuators A, Vol. 88, 2001, pp. 263-272.

[46] J. H. Ginsberg, "Mechanical and structural vibrations," John Willey & Sons, Inc., 2001.

[47] S. Pourkamali and F. Ayazi, "High frequency low impedance silicon BAR structures," Proceedings, Hilton Head 2006, solid-state sensor, actuator and Microsystems workshop, pp. 284-287.

[48] B. Jaffe, et al, "Piezoelectric Ceramics", NewYork: Academic Press, 1971.

[49] S. Fujishima, et al, "Tuning fork resonators for electronic wrist watches using ZnO sputtered film", 1st meeting on application of ferroelectric materials in Japan, 1977.

[50] A. S. Paulo, et al, "Atomic force microscopy characterization of electromechanical properties of RF acoustic bulk wave resonators," MEMS 2004, pp. 169-172.

[51] J. D. Larson, et al, "Power handling and temperature coefficient studies in FBAR duplexers for the 1900 MHz PCS band," Ultrasonics Symposium, 2000, Vol. 1, pp.869 – 874.

[52] K. Wang and C. T.-C. Nguyen, "High-order medium frequency micromechanical electronic filters," JMEMS 8(4), 534, (1999).

[53] A.-C. Wong, J. R. Clark, and C. T.-C. Nguyen, "Anneal-activated, tunable, 68MHz micromechanical filters," Sensors and Actuators 99, pp. 1390-1393.

[54] L. Lin, R. T. Howe, and A. P. Pisano, "Microelectromechanical Filters for Signal Processing," JMEMS 7(3), 286, (1998).

[55] D. S. Greywall and P. A. Busch, "Coupled micromechanical drumhead resonators with practical applications as electromechanical bandpass filters," J. Micromech. Microeng. 12 (2002) 925-938.

[56] S. Pourkamali, R. Abdolvand, and F. Ayazi, "A 600kHz electrically coupled MEMS bandpass filter," proceedings, MEMS'03, 2003, pp. 702-705.

[57] S. Pourkamali, R. Abdolvand, G. K. Ho, and F. Ayazi, "Electrostatically coupled micromechanical beam filters," proceedings, MEMS'04, pp. 584-587.

[58] S. Pourkamali and F. Ayazi, “Electrically coupled MEMS bandpass filters-Part I: with coupling element,” Journal of Sensors and Actuators A 122, 2005, pp. 307-316.

[59] S. Pourkamali and F. Ayazi, “Electrically coupled MEMS bandpass filters-Part II: without coupling element,” Journal of Sensors and Actuators A 122, 2005, pp.317-325.

[60] K. Wang, F. D. Bannon, J. R. Clark and C. T. C. Nguyen, “Q-Enhancement of microelectromechanical filters via low velocity spring coupling,” IEEE Ultrasonics symposium, 1997, pp. 323-327.

[61] G.K. Ho, R. Abdolvand, and F. Ayazi, "Through-Support-Coupled Micromechanical Filter Array," Proceedings, MEMS '04, 2004, pp.769-772.

[62] S.-S. Li, Y.-W. Lin, Y. Xie, Z. Ren, and C. T.-C. Nguyen, “Small percent bandwidth design of a 431-MHz notch-coupled micromechanical hollow-disk ring mixer-filter,” *Proceedings*, IEEE Int. Ultrasonics Symposium, Sept. 18-21, 2005, 1295-1298

[63] P. J. Stephanou, G. Piazza, C. D. White, M. B. J. Wijesundara, and A. P. Pisano, "Mechanically coupled contour mode piezoelectric Aluminum Nitride MEMS filters," IEEE MEMS 2006, pp. 906-909, 2006.